THE STRUCTURE, STABILITY AND INTERACTION OF GEOPHYSICAL VORTICES

Hanna Płotka

A Thesis Submitted for the Degree of PhD
at the
University of St Andrews

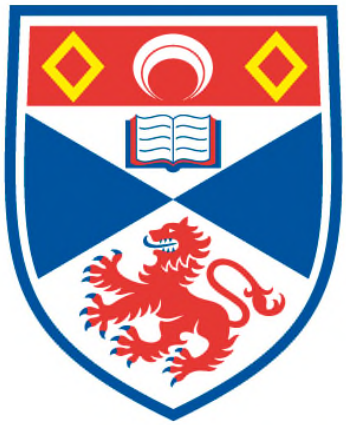

2013

The structure, stability and interaction of geophysical vortices

Hanna Płotka

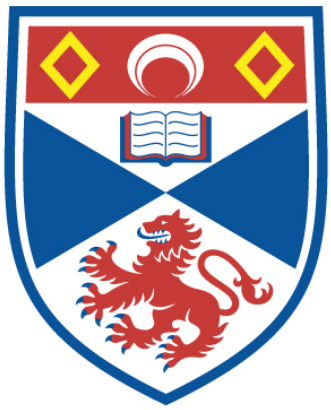

University of St Andrews

A thesis submitted for the degree of Doctor of Philosophy at the

University of St Andrews

22nd April 2013

Abstract

This thesis examines the structure, stability and interaction of geophysical vortices. We do so by restricting our attention to relative vortex equilibria, or states which appear stationary in a co-rotating frame of reference. We approach the problem from three different perspectives, namely by first studying the single-vortex, quasi-geostrophic shallow-water problem, next by generalising it to an (asymmetric) two-vortex problem, and finally by re-visiting the single-vortex problem, making use of the more realistic, although more complicated, shallow-water model.

We find that in all of the systems studied, small vortices (compared to the Rossby deformation length) are more likely to be unstable than large ones. For the single-vortex problem, this means that large vortices can sustain much greater deformations before destabilising than small vortices, and for the two-vortex problem this means that vortices are able to come closer together before destabilising. Additionally, we find that for large vortices, the degree of asymmetry of a vortex pair does not affect its stability, although it does affect the underlying steady state into which an unstable state transitions. Lastly, by carefully defining the "equivalence" between cyclones and anticyclones which appear in the shallow-water system, we find that cyclones are more stable than anticyclones. This is contrary to what is generally reported in the literature.

Acknowledgements

First and foremost, I would like to thank my supervisor, Professor David Dritschel for his advice, support, and for always having time to see me. I can't express how much I've learnt under his guidance.

Thanks are also due to current and past members of the Vortex Dynamics Research Group, for discussions on both scientific and personal topics.

Finally, I would like to thank my friends and family, who, willingly or not, joined me on this PhD-journey. A special mention here should go to the members of "GeekSoc", for adding a certain interdisciplinarity to my research.

I am grateful to the UK Natural Environment Research Council for their financial support.

Declaration

I, Hanna Płotka, hereby certify that this thesis, which is approximately 40,500 words in length, has been written by me, that it is the record of work carried out by me and that it has not been submitted in any previous application for a higher degree.

I was admitted as a research student in August 2009 and as a candidate for the degree of Doctor of Philosophy in August 2009; the higher study for which this is a record was carried out in the University of St Andrews between 2009 and 2013.

Date: ..... **Signature of Candidate:** .....

I hereby certify that the candidate has fulfilled the conditions of the Resolution and Regulations appropriate for the degree of Doctor of Philosophy in the University of St Andrews and that the candidate is qualified to submit this thesis in application for that degree.

Date: ..... **Signature of Supervisor:** .....

In submitting this thesis to the University of St Andrews I understand that I am giving permission for it to be made available for use in accordance with the regulations of the University Library for the time being in force, subject to any copyright vested in the work not being affected thereby. I also understand that the title and the abstract will be published, and that a copy of the work may be made and supplied to any bona fide library or research worker, that my thesis will be electronically accessible for personal or research use unless exempt by award of an embargo as requested below, and that the library has the right to migrate my thesis into new electronic forms as required to ensure continued access to the thesis. I have obtained any third-party copyright permissions that may be required in order to allow such access and migration, or have requested the appropriate embargo below.

The following is an agreed request by candidate and supervisor regarding the electronic publication of this thesis: Embargo on both of printed copy and electronic copy for the same fixed period of 2 years on the grounds that publication would preclude future publication.

Date: .....
Signature of Candidate: .....
Signature of Supervisor: .....

Contents

Abstract **i**

Acknowledgements **ii**

Declaration **iii**

Contents **v**

Commonly used symbols **ix**

1 Introduction **1**

1.1 The concept of balance 3

1.2 Vortex equilibria 8

1.3 Overview of thesis 11

2 Quasi-geostrophic shallow-water simply-connected equilibria **12**

2.1 Introduction 12

2.2 The flow model and vortex-patch equilibria 15

2.2.1 Quasi-geostrophic flow 15

2.2.2 The vortex-patch model 16

2.2.3 Properties of the equilibria 18
2.3 Linear stability 26
2.3.1 Method 26
2.3.2 Results 28
2.4 Nonlinear evolution 32
2.4.1 Method 32
2.4.2 Results 33
2.5 Conclusions 40
2.6 Supplementary movies 41

3 Quasi-geostrophic shallow-water doubly-connected equilibria 42

3.1 Introduction 42
3.2 Flow model and properties of the equilibria 44
3.2.1 Quasi-geostrophic shallow-water flow and the vortex-patch model 44
3.2.2 Properties of the equilibria 47
3.3 Linear stability analysis 55
3.4 Nonlinear evolution 57
3.4.1 Method 59
3.4.2 Results 60
3.5 Transitions between simply- and doubly-connected equilibria . . . 72
3.6 Conclusions 81
3.7 Supplementary movies 83

4 Shallow-water simply-connected quasi-equilibria **84**

4.1 Introduction 84

4.2 Model formulation 86

4.2.1 The shallow-water model and the concept of balance . . . 86

4.2.2 Flow initialisation 88

4.2.3 Flow evolution 91

4.3 Quantifying the degree of steadiness 93

4.4 Stability 102

4.5 Types of evolution 107

4.6 Quantification of imbalance 114

4.7 Conclusions 125

4.8 Supplementary movies 127

5 Summary and Outlook **128**

A Derivation of the linear dispersion relation for small amplitude waves **134**

B Contour-integral form of the energy for quasi-geostrophic vortex patches **136**

C Supplementary movie captions **140**

C.1 Movies of quasi-geostrophic shallow-water simply-connected equilibria 140

C.2 Movies of quasi-geostrophic shallow-water doubly-connected equilibria 141

C.3 Movies of shallow-water simply-connected quasi-equilibria 142

Bibliography **143**

Commonly used symbols

g	acceleration due to gravity
f	Coriolis frequency
c	short-scale gravity-wave speed
p	pressure
q	potential vorticity
Ω	rotation rate
$\boldsymbol{v} = (u, v, w)$	three-dimensional fluid velocity
$\boldsymbol{u} = (u, v)$	two-dimensional fluid velocity
$\boldsymbol{u}' = (u', v')$	two-dimensional fluid velocity in a rotating reference frame
$\zeta = \frac{\partial v}{\partial x} - \frac{\partial u}{\partial y}$	vertical component of vorticity
ψ	streamfunction
δ	divergence of velocity
χ	divergence of acceleration
$\mathcal{R}$	Rossby number
$\mathcal{F}$	Froude number
H	mean fluid depth
h	fluid depth
U	characteristic horizontal velocity scale
L	characteristic horizontal length scale
L_D	Rossby deformation length
$\gamma = L/L_D$	relative size of vortices

λ	ratio of the minor to major axes of a vortex
δ_{min}	minimum distance between two vortices
α	ratio between areas of two vortices (smaller to larger vortex)
E	energy
J	angular impulse
Ω_p	particle rotation rate
P	arc length
κ	curvature
T_p	particle rotation period
T_{ip}	inertial time period
M	mass
B	Bernoulli pressure
ϵ_b	steadiness parameter
PV	potential vorticity
QGPV	quasi-geostrophic potential vorticity
QG	quasi-geostrophic
SW	shallow-water
QGSW	quasi-geostrophic shallow-water
IGW	inertia-gravity wave
CASL	Contour Advective Semi-Lagrangian
OPV	optimal potential vorticity
PVI	dynamic potential vorticity initialisation

Chapter 1

Introduction

Human beings have been observing the skies and oceans since the beginning of time. They have been doing so in awe of their incredible, ever-changing beauty, but also for more practical reasons, for example to predict if a storm is approaching, or to try to map out sea currents for ocean voyages. What is probably masked from the average day-dreamer who gazes at clouds trying to find shapes in them, or who listens to the lulling sounds of waves at the beach, is that because both the Earth's ocean and atmosphere, indeed, also the atmospheres of other planets, are made of fluid (water and air, respectively), and because both are affected by planetary rotation and stratification, once certain approximations have been made, their dynamics are governed by the same equations. As a result, although certain restrictions do exist, both can be studied simultaneously.

Over the centuries, we have gained much understanding about how planetary systems work, but as our knowledge has been increasing, so has our awareness of how much more we have to learn. With the onset of the "digital age" and the increased accessibility to fast and reliable computing power, the study of geophysical motions, including also their numerical study, has been able to move quickly forward, and over recent years much progress has been made. There have

been two main approaches to modelling such motions. The first is to include as many components of the flow as possible, and to see how it evolves. This is especially beneficial for areas like numerical weather prediction or climate modelling, which aim to forecast the evolution of a system from a given initial configuration. However, this approach often masks the roles which individual components, and their interactions, play in such evolutions, and thus a second approach may be adopted. Here, only very simple flows are considered and studied, and once their fundamental features have been understood, complexity is added. In this thesis, we follow this approach and start out with one of the simplest, "balanced" models of geophysical fluid dynamics, the quasi-geostrophic shallow-water model, and once we have understood simple single-vortex equilibrium configurations, we add complexity by first studying the two-vortex problem, and next by revisiting the single-vortex problem, but this time using a richer model which allows "unbalanced" motions.

The first step towards obtaining a simplified flow, which is still complex enough to provide insight into phenomena of interest, is to filter out motions which do not play a significant role in its evolution. Fully three-dimensional geophysical flows are composed of a range of motions at different spatial and temporal scales. They range from small-scale occurrences such as the motion of fluid generated by a fish swimming in the ocean, to the large-scale oceanic circulation; from the displacement of air as you fan yourself on a hot summer day, to a hurricane such as Hurricane Katrina of 2005, which claimed over 1500 lives and caused billions of dollars worth of damage in the United States of America. Since, generally, small-scale phenomena tend not to influence those at large scales (simply imagining that the flutter of the wings of a butterfly could affect the progression of a storm seems ridiculous, despite the popular myth), we can filter them out from the flows we consider, and instead focus on the then less noisy large-scale motions. To do this, we define the dimensionless Rossby num-

ber, $\mathcal{R} = \zeta/f$, which measures how important the relative vorticity ζ of a flow is compared to the planetary rotation embodied by f, the Coriolis frequency. Phenomena with $\mathcal{R} \lesssim 1$ are slow, whereas those with $\mathcal{R} \gtrsim 1$ are fast and may be neglected as they generally do not play an important role in the evolution of the flow. Note that the Rossby number measures the role of the Earth's rotation on fluid motions, and this often relates to their spatial extent. As an example, planetary rotation will not affect the trajectory of a ball thrown across a room, but the trajectory will become curved if the same ball is thrown from Scotland to California. Vallis (2006) points out that the Rossby number can be viewed in terms of measuring time-scales, where "short" phenomena, such as individual clouds or a tornado, are unaffected by the Earth's rotation, and thus have large values of the Rossby number.

Through a scale analysis, Pedlosky (1979) shows that typical values of mid-latitude $\mathcal{R}$ are about 0.1 in the atmosphere and an order of magnitude smaller, 0.01, in the oceans.

1.1 The concept of balance

Having chosen the appropriate range of scales of motion, we next decompose the flow into a form which is easier to understand. As mentioned previously, the complete, turbulent geophysical systems are highly-nonlinear and exceedingly complex. It is therefore beneficial to view them through the concept of "balance", which decomposes a flow into two parts. The first, "balanced", part consists of low-frequency, slow motions which dominate the flow evolution. This component relates to vortical motions, which arise naturally as a result of the planetary rotation, and are commonly-occurring dynamical features of the Earth's oceans and atmosphere, and of the atmospheres of the planets. The second, "unbalanced" part consists of high-frequency, short-lived motions, which relate to the propaga-

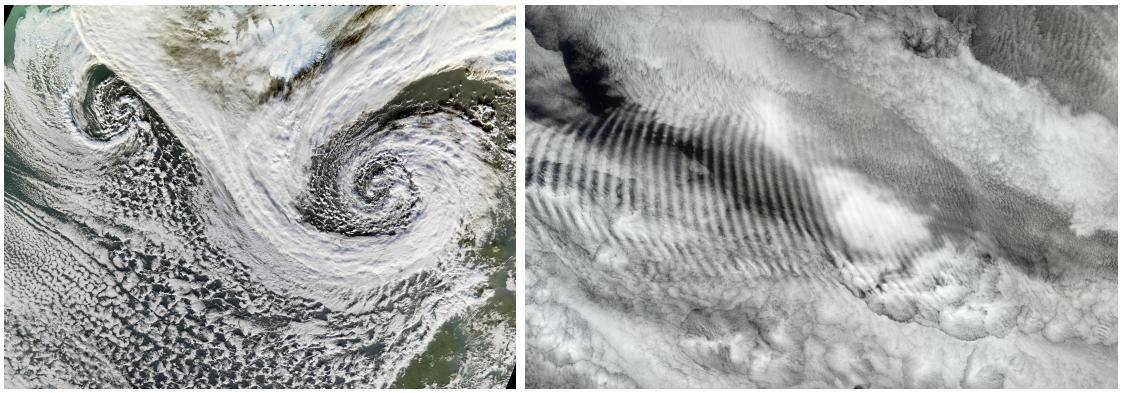

Figure 1.1: Examples of the two different types of motion present in geophysical flows. On the left we see an example of the balanced component: two cyclones formed in tandem over Iceland and Scotland in November 2006 (image source: http://www.nasa.gov/multimedia/imagegallery/image_feature_735.html). On the right we see an example of the unbalanced component: an inertia-gravity wave "ripple" over the Indian Ocean in October 2003 (image source: http://eosweb.larc.nasa.gov/HPDOCS/misr/misr_html/cloud_gravity_waves.html).

tion of inertia-gravity waves (IGWs). Figure 1.1 shows atmospheric examples of both of these types of motion. The left-hand panel of the figure shows "balanced" motion in the form of two cyclones, whereas in the right-hand panel we see an example of IGWs. In the cases shown, the two types of motion are visualised thanks to the presence of clouds, however it should be noted that they may not always be visible to the naked eye.

Vortex motions are ubiquitous in geophysical flows. It has been estimated that in the surface layers of the North Atlantic alone there are over 10,000 vortices (Ebbesmeyer et al., 1986). Examples of terrestrial vortices include structures like the atmospheric "polar vortex", which dominates the extratropical winter stratosphere (Norton, 1994), and oceanic Gulf-stream rings, which detach themselves from the current and, while retaining many of its properties, may have life-times of up to four years (Carton, 2001). The Great Red Spot on Jupiter is perhaps the most famous such structure occurring outside the Earth and has persisted for at least 500 years. Numerical simulations of weakly-forced and damped geophysical flows over the past three decades indicate that vortices

emerge spontaneously from incoherent motions and subsequently dominate the "turbulent" flow evolution (cf. McWilliams, 1984, and many others since), at least under conditions when large-scale planetary vorticity gradients may be neglected. Two-dimensional turbulence, especially at late times, is dominated by widely-separated vortex structures within a sea of filamentary debris (see e.g. Fornberg, 1977; Santangelo et al., 1989; Dritschel et al., 2008, and references therein).

It is beneficial to view vortices as local concentrations of potential vorticity (PV), a scalar, which in the absence of viscous and diabatic effects is materially conserved by fluid particles. The importance of its role as a scalar tracer for rotating, stratified flows was first noted by Carl-Gustaf Rossby in the 1930s, and later, in a more general form, it was defined by Hans Ertel in 1942 to be

$$\Pi = \frac{\boldsymbol{\omega}_a}{\rho} \cdot \nabla\theta,$$

where $\boldsymbol{\omega}_a$ is the absolute vorticity (including the Earth's background rotation), ρ the fluid density, and θ the potential temperature, or the temperature a fluid particle at pressure p would acquire if it was adiabatically brought down to some reference pressure p_0. We have its material conservation, or

$$\frac{D\Pi}{Dt} = \frac{\partial\Pi}{\partial t} + \boldsymbol{v} \cdot \nabla\Pi = 0,$$

where $\boldsymbol{v}$ is the velocity.

In addition to being materially conserved, the special thing about PV is that, given its instantaneous distribution, through what is known as the "invertibility principle" (Hoskins et al., 1985) all other dynamical fields, like the velocity and pressure, may be determined often to an astonishing degree of accuracy. In a flow in which the presence of the unbalanced component is not permitted, doing so

exactly is possible[1], but in more complex flows which are not free of ageostrophic and unbalanced motions, this inversion process is less straightforward and non-unique (see McIntyre and Norton, 2000; Mohebalhojeh and Dritschel, 2000; Mohebalhojeh, 2002; Dritschel and Viúdez, 2003; McKiver and Dritschel, 2008, and others). Ford et al. (2000) have shown that in such flows, the "slow manifold" completely devoid of IGWs does not exist. However, viewing a flow through the concept of "balance" still provides valuable insight into its nature, and so it can be decomposed into a "minimally unbalanced" part, which nevertheless contains some degree of unbalanced wave activity, and an "unbalanced" one, composed of all the residual motions. There are various more-or-less accurate methods for performing this decomposition, though a unique form of these "minimally unbalanced" fields does not exist. It is useful however to regard PV as being entirely free of IGWs, so that IGWs cannot generate PV (they can only add to its advection). It should be noted though that the breaking of IGWs may lead to PV generation (Bühler, 2010).

In this thesis, two different models of geophysical fluid dynamics are used. The first, the quasi-geostrophic shallow-water model (QGSW), also known as the one-and-a-half layer model or the equivalent barotropic model, is a fully (geostrophically) balanced model, in which the unbalanced and ageostrophic components have been completely filtered out. It is perhaps the most popular model to date for the study of fundamental aspects of atmospheric and oceanic flows (Vallis, 2006). The QGSW model is, despite its simplicity, nonlinear *and* parameter rich. Its simplifying feature is that in addition to the non-divergent flow field $\boldsymbol{u} = (u, v)$ being two dimensional, the evolution of the system is governed by the material advection of a single scalar, namely the quasi-geostrophic potential vorticity (QGPV), and it is possible to invert the QGPV exactly to obtain all of

[1]In quasi-geostrophic flows, this "inversion" amounts to inverting a generalised Laplace or Helmholtz operator to obtain a streamfunction, from which the velocity and temperature can be recovered by differentiation; these ideas date back to Charney (1948).

the dynamical fields. The QGSW model is versatile and embodies key elements of geophysical flows: vortices, fronts, jets and turbulence.

The second model used is the shallow-water (SW) model, which describes the motion of an incompressible fluid subject to planetary rotation and gravity effects. It is the simplest model which permits "balanced" vortical motions, ageostrophic effects, and "unbalanced" inertia-gravity waves (IGWs). Here, unlike in geostrophically balanced systems, the symmetry between anticyclonic and cyclonic motions, or motions in opposite directions (in the northern hemisphere, the clockwise and counter-clockwise directions, respectively), is broken. This further allows insight into the well-known asymmetry which exists in both realistic geophysical flows (McWilliams, 1985) and in their numerical simulations (Cushman-Roisin and Tang, 1990; Arai and Yamagata, 1994; Polvani et al., 1994, and others), as well as insight into the role of the unbalanced component in the flow evolution (Mohebalhojeh and Dritschel, 2001). However, in SW it is no longer possible to invert PV exactly to obtain the relevant dynamical fields, although state-of-the-art numerical methods exist for obtaining very accurate approximations of them. Additionally, a SW flow can be initialised in a way to contain minimal amounts of imbalance, so that any IGWs produced may be interpreted as a result of the flow evolution, rather than a numerical artefact (see chapter 4 for details). This allows for a quantitative study of the role of the unbalanced component. A higher-order (than QGSW) balanced model could be used to examine ageostrophic effects, however the choice of the order of balance to use is arbitrary, and so here we turn to the SW model which allows all orders of balance, at the cost of also including the unbalanced component.

1.2 Vortex equilibria

By employing the QGSW and SW models described above, in this thesis we study relative vortex equilibria (or just "equilibria"); these are vortices which do not change in shape in an appropriately chosen frame of reference. This is of interested as it provides insight into the nature of the long-lived vortices which are found not only in the oceans (Olson, 1991; Carton, 2001) and the Earth's and planetary atmospheres (Waugh and Polvani, 2010; Garate-Lopez et al., 2013), but also in simulations of turbulent geophysical flows (McWilliams, 1984; Polvani et al., 1994). These structures remain relatively unchanged by external factors, and often dominate the flow evolution. Additionally, the theory of "adiabatic steadiness" (see Legras et al., 2001, and references) states that widely separated vortices evolve through a series of near-equilibrium states in between strong interactions. These states are determined by the instantaneous local straining flow exerted by the surrounding vortices, and an adiabatic, quasi-steady evolution takes place until an unstable equilibrium state is reached, after which rapid, unsteady motion of the vortices ensues. Hence, understanding the solutions and stability of the equilibrium states allows predictions as to the nature of vortex interactions.

The study of vortex equilibria dates back to Deem and Zabusky (1978a,b), who studied single (simply-connected) rotating vortex equilibria and two-vortex (doubly-connected) translating equilibria. Since then, various other studies have examined the problem, including: Saffman and Szeto (1980), who found steady solutions for symmetric co-rotating states, Pierrehumbert (1980), who did the same for symmetric translating states, Dritschel (1985, 1995) who examined 2 to 8 like-signed vortex equilibria and asymmetric like- and opposite-signed vortices, respectively, Makarov and Kizner (2011) who studied two-vortex equilibria of unequal sizes and vorticities, and Luzzatto-Fegiz and Williamson (2010, 2011) who

used an energy-based argument following Kelvin's variational principle (Thomson, 1875) to find equilibria solutions bifurcating from the Kirchhoff elliptical solution branch.

A limitation of the aforementioned studies is that they deal exclusively with two-dimensional (or "barotropic") systems, while in realistic geophysical flows stratification also plays an important dynamical role. As a midpoint between the two-dimensional and the more complex three-dimensional systems, the QGSW approximation may be used. Through the introduction of a new length scale, the Rossby deformation length L_D, a link can be made between the effects of stratification and planetary rotation in a succinct way. Fluid motions having scales much smaller than L_D behave in the classical two-dimensional manner, whereas motions at scales larger than L_D become confined to fronts or jets of width $\mathrm{O}(L_D)$ and are strongly affected by free-surface or layer-thickness deformations. Note that in shallow-water $L_D = c/f$, where c is the short-scale gravity wave speed, representing the effects of stratification, and f is the Coriolis frequency, representing planetary rotation. In QGSW, in which unbalanced motions have been filtered out, c is infinite, and so here L_D is simply a parameter.

Only a few studies have examined the effects of a finite Rossby deformation length on vortex equilibria. Yet, both experimental (Griffiths and Hopfinger, 1986, 1987) and numerical studies have found qualitative changes in the behaviour of the system. Polvani (1988) and Polvani et al. (1989) studied equilibrium forms of simply-connected and doubly-connected states. Waugh (1992) examined the effects of L_D on symmetric vortex merger, and Yasuda (1995) showed that the QGSW model better represents realistic oceanic vortices. These studies have found that larger vortices are able to sustain greater deformations and get closer together before the onset of instability than smaller ones, and that at large-scales (larger than L_D) there is a roll-up of filaments of vorticity and a suppression of filamentation. Makarov et al. (2012) examined the effects of L_D on the form

and stability of a pair of steadily translating, doubly-symmetric vortex patches, where each patch was located in a different layer of a two-layer rotating fluid. They found that increasing the size of this two-vortex structure relative to L_D destabilises it, although for large enough vortices the conditions necessary for stability become L_D-independent. Other studies, including Waugh and Dritschel (1991) who studied generalised geophysical models of vortex dynamics, further elaborate the differences between the large- and small-L_D regimes.

The study of vortex equilibria in an ageostrophic context is significantly more difficult. A higher-order balanced model, incorporating ageostrophic effects can be used for this, however the choice of the order of balance used is arbitrary. Instead, as a stepping stone to the highly complex, three-dimensional system, the two-dimensional shallow-water (SW) model may be considered, which contains all orders of balance at the cost of also including IGWs. Despite being the simplest unbalanced model, the SW model still presents significant challenges for both analytical and numerical study. As a result, to date, only a few studies have examined SW equilibria. In fact, due to the spontaneous emission of IGWs, shallow-water equilibria are not strictly steady, but radiate such weak IGWs that they may be deemed steady for all practical purposes. Cushman-Roisin et al. (1985) found exact analytical solutions for time-dependent cyclonic elliptical SW vortices, Cushman-Roisin (1987) did the same for anticyclonic ones, and Ripa (1987) developed a stability criterion for SW equilibria. However, this criterion is not applicable to isolated vortices. Stegner and Dritschel (2000) numerically investigated the effects of size, the steepness of the vorticity profile, and strength (Rossby number) on the stability of both cyclonic and anticyclonic isolated circular vortices. In the limit when the Rossby deformation length is large, Ford (1994) found peanut-shaped equilibria analogous to those found in the QGSW context by Polvani et al. (1989). Kizner et al. (2002) numerically constructed barotropic dipole equilibria, while Kizner et al. (2008) found exact, analytic solu-

tions for steadily translating dipolar structures. Notwithstanding, to date there has been no comprehensive examination of SW equilibria and their stability.

1.3 Overview of thesis

This thesis is organised as follows. In chapter 2 we study the equilibrium form, properties, stability and nonlinear evolution of steadily-rotating simply-connected vortex patches in the single-layer f-plane quasi-geostrophic shallow-water (QGSW) model of geophysical fluid dynamics. Here, we also provide an overview of the QGSW model and discuss our results.

By noting that after instability, many of the initially simply-connected states evolve into two co-rotating vortices which seem to have near-equilibrium forms, in chapter 3 we examine doubly-connected (two-vortex) equilibria. Specifically, we study their form, properties, stability and evolution, again in the single-layer f-plane QGSW model. We concentrate on states in which the two vortices are of equal strength, but have an asymmetry in size.

In chapter 4 we revisit the simply-connected vortex-patch problem, however this time using the richer shallow-water model. Having understood the forms of the equilibria in a balanced model in chapter 2, we aim to see how a departure from balance affects their properties, form, and stability, and to examine the role of the ageostrophic component and the significance of inertia-gravity waves.

We finally end with a summary and several suggestions for further work in chapter 5.

Chapter 2

Quasi-geostrophic shallow-water simply-connected equilibria

The following chapter consists of a study, Płotka and Dritschel (2012), published in the journal *Geophysical & Astrophysical Fluid Dynamics* and the work is reproduced here with minor modifications.

2.1 Introduction

As mentioned in chapter 1, vortices are an omnipresent feature of the Earth's oceans and atmosphere, and of the planetary atmospheres. A special case of vortices are dumbbell-shaped ones, as shown in figures 2.1 and 2.2. These occur both in experimental studies (Meunier and Leweke, 2001; Cerretelli and Williamson, 2003b) and in simulations of turbulent flows. Figure 2.1 shows such a vortex which forms from an initially turbulent field in a numerical simulation and persists for many rotation periods. Additionally, dumbbell-shaped structures may also be found in the Earth's atmosphere. For example, during the "sudden stratospheric warming" phenomenon, a dumbbell structure appears and lasts a few days

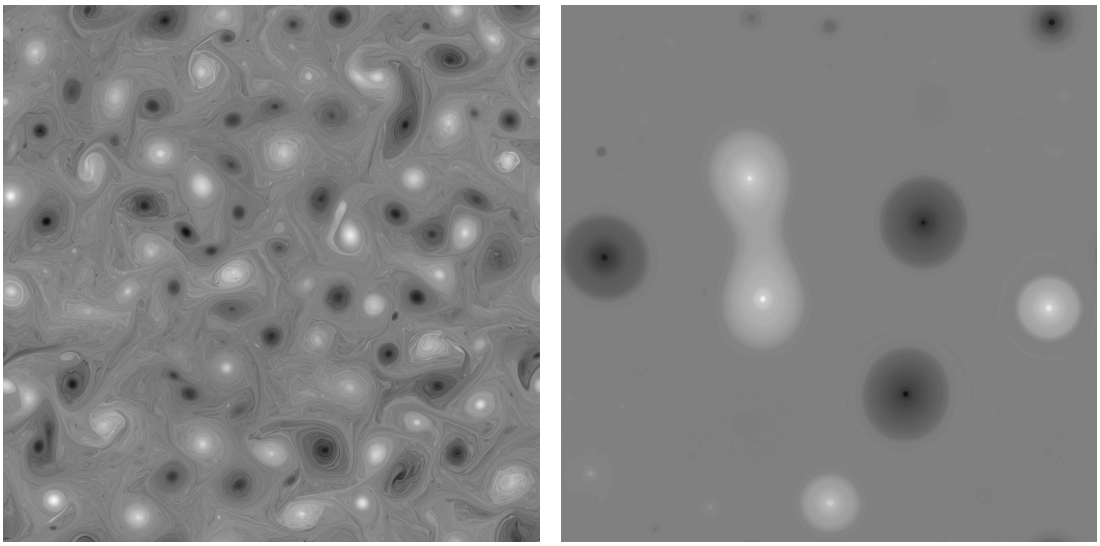

Figure 2.1: An example of the formation of dumbbell-shaped vortices in two-dimensional quasi-geostrophic turbulence (simulated using the CLAM method (Dritschel and Fontane, 2010) at an effective resolution of 4096^2). Here, the domain has dimensions 2π by 2π, and we have the Rossby deformation wavenumber $k_D = 1/L_D = 10$ and $L \approx 0.071$ (calculated from the area of the dumbbell-shaped vortex in the right-hand panel), giving $L/L_D \approx 7$. Starting from a random-phased PV field peaked at wavenumber $k_0 = 20$ (shown on the left at $T = 100$ in units of $T = L_D/u_{\mathrm{rms}}(0)$), we let the field decay freely for 20000 time units. Halfway through the simulation, at roughly $T = 10750$, a dumbbell-shaped state forms, which persists until the end of simulation (for almost 10000 time units). This is shown at time $T = 15000$ on the right.

before breaking up (Rosier et al., 1994). Furthermore, given the variety of different structures found in the ocean, it is also likely that oceanic dumbbell-shaped vortices exist.

Vortices occur over a vast range of spatial and temporal scales, and their interactions can be exceedingly complex (cf. Dritschel and Scott, 2009). To be able to better understand their fundamental properties, idealisations need to be made. Here, following many previous studies, we focus on one of the simplest geophysical fluid dynamical models, namely the quasi-geostrophic shallow water model (Polvani et al., 1989; Waugh and Dritschel, 1991). The key feature of this model is the Rossby deformation length L_D, embodying the effects of rotation

and stratification in a succinct way. The importance of the Rossby deformation radius, in QGSW simply a parameter, is that fluid motions at scales $L \ll L_D$ behave in the classical two-dimensional (2D) manner, with negligible free-surface deformations (as in the 2D Euler equations), while on the other hand, motions at scales $L \gg L_D$ are strongly affected by free-surface deformations, and become confined to fronts or jets of width $\mathrm{O}(L_D)$. In the oceans, typical L_D values range from 25 to 100km, values comparable to the radius of many ocean eddies such as Gulf Stream "rings" or "meddies" (Carton, 2001). In the Earth's atmosphere at mid-latitudes and poleward, typical L_D values are an order of magnitude larger, ranging from 1000 to 1500km (Charney and Flierl, 1981; Juckes and McIntyre, 1987). In Jupiter's atmosphere, indirect modelling estimates suggest L_D is $1/40^{\text{th}}$ of the planet's radius (Cho et al., 2001).

In this chapter, we investigate how the ratio $\gamma = L/L_D$ affects the dynamics of a flow in an especially simple context, namely in the equilibrium shape and stability of an isolated, two-fold symmetric patch of uniform PV. Note that our γ^{-2} is equivalent to the Burger number. The barotropic case $\gamma = 0$ is well understood; in this case, the flow is described by the 2D Euler equations, and the equilibria take the form of ellipses, $x^2/a^2 + y^2/b^2 = 1$ (Kirchhoff, 1876). These (relative) equilibria rotate at a constant rate Ω which depends only on the aspect ratio $\lambda = b/a$ and the uniform PV q_0 (here simply vorticity): $\Omega = q_0\lambda/(1+\lambda)^2$. In 1893 Love showed that these equilibria are linearly unstable if $\lambda < 1/3$, with the first mode of instability having an asymmetric wave-3 form (in elliptic coordinates). This instability has since been confirmed in the fully nonlinear equations (see, e.g. Dritschel, 1986), and extensive studies examining the evolution of unstable elliptical vortices have been done (see, e.g. Polvani and Flierl, 1986; Mitchell and Rossi, 2008, and others).

Much less is known when $\gamma > 0$. Polvani et al. (1989) developed a numerical procedure to compute two-fold symmetric equilibria for a selected set of param-

eters, specifically $\lambda = 0.6$, 0.4, and 0.286, each for 21 γ values equally spaced on a logarithmic scale between 10^{-2} and 10^{2}. They found that the finite-L_D ($\gamma > 0$) equilibria are qualitatively different from ellipses, with these differences becoming more pronounced at smaller aspect ratios λ, where the vortices become dumbbell-shaped. Our purpose here is to extend their work first by a more comprehensive coverage of parameter space, and then by studying the linear and nonlinear stability of the equilibria (it turns out that most instabilities occur for $\lambda < 0.286$). High-resolution nonlinear simulations permit us to examine the fate of instabilities, and provide a deeper understanding of the effects of finite L_D.

This chapter is organised as follows. In §2.2 we first review the physical system, present the numerical method used to find the equilibria, and then discuss the shapes and properties of the equilibria. This is followed by a linear stability analysis in §2.3 and by nonlinear numerical simulations in §2.4. We conclude in §2.5 with a summary of the main findings. Information on supplementary movies is given in §2.6.

2.2 The flow model and vortex-patch equilibria

2.2.1 Quasi-geostrophic flow

The quasi-geostrophic shallow-water (QGSW) model is perhaps the most popular model to date for the study of fundamental aspects of atmospheric and oceanic (geophysical) flows (Vallis, 2006). This is due to the model's great simplicity: two-dimensional, no gravity waves ("balanced"), versatility. Yet, the QGSW model embodies key elements of geophysical flows: potential-vorticity, vortices, fronts, jets and turbulence. Here, we examine this model in its simplest form: no forcing, no damping, no topography, and constant planetary vorticity f. The corresponding QGSW model consists of a single "prognostic" equation

for the material (conservative) advection of quasi-geostrophic potential vorticity "QGPV" q,

$$\frac{\mathrm{D}q}{\mathrm{D}t} = \frac{\partial q}{\partial t} + u\frac{\partial q}{\partial x} + v\frac{\partial q}{\partial y} = 0, \tag{2.1}$$

and a Helmholtz-type "inversion relation" providing the (non-divergent) flow field $\boldsymbol{u} = (u, v)$ from q,

$$(\nabla^2 - L_D^{-2})\psi = q\,, \qquad u = -\frac{\partial \psi}{\partial y}\,, \qquad v = \frac{\partial \psi}{\partial x}, \tag{2.2}$$

where ψ is the streamfunction.

2.2.2 The vortex-patch model

We consider the simplest form of a vortex, namely a patch of uniform (QG)PV, $q = q_0$, in an unbounded domain with $q = 0$ outside the vortex. The vortex is entirely prescribed by its boundary shape, and we seek the shapes which are preserved under the dynamical evolution, i.e. that steadily rotate. (Note, these are often referred to as "relative equilibria", but here we will simply call them "equilibria".) Many possible shapes are likely to exist, depending on the symmetry imposed (or not). Here, we seek two-fold symmetric simply-connected shapes, analogous to the elliptical vortices found in the barotropic limit $\gamma = L/L_D = 0$. An example is given in figure 2.2.

The simplicity of a vortex-patch carries over to the calculation of its induced velocity field. As shown by Deem and Zabusky (1978a,b), the dynamics of a vortex-patch depends only on the shape of its bounding contour, a property coined "contour dynamics". Using Stokes' theorem, one can reduce the double integral involved in inverting the operator $\nabla^2 - L_D^{-2}$ to a single contour integral, resulting in

$$\frac{\mathrm{d}\boldsymbol{x}}{\mathrm{d}t} = \boldsymbol{u}(\boldsymbol{x}) = \frac{q_0}{2\pi}\oint_{\mathcal{C}} \mathrm{K}_0(|\boldsymbol{x} - \boldsymbol{x}'|/L_D)\mathrm{d}\boldsymbol{x}', \tag{2.3}$$

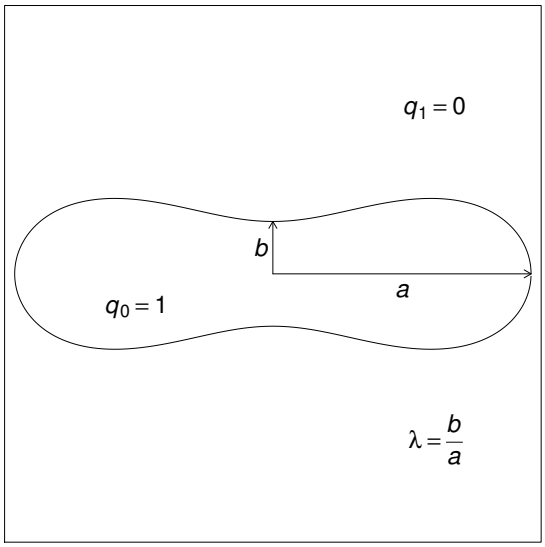

Figure 2.2: Schematic diagram of a vortex-patch equilibrium.

where K_0 is the modified Bessel function of zeroth order, $\mathcal{C}$ is the bounding contour, drawn in a right-handed sense, and $\boldsymbol{x}' \in \mathcal{C}$. When $\boldsymbol{x} \in \mathcal{C}$ also, this equation fully describes the motion of $\mathcal{C}$. It may be generalised to any number of contours $\mathcal{C}$ by simple linear superposition (Dritschel, 1989).

The equilibria are generated following the iterative numerical procedure discussed in Dritschel (1995). Without loss of generality, the PV inside the vortex is set to $q_0 = 1$, and the area of the vortex is set to $A = \pi$ (the latter implies that the characteristic length scale $L = 1$). Then, starting from a circular patch, which is a known equilibrium for any value of $\gamma = L/L_D$, we slightly decrease the aspect ratio λ by $\Delta\lambda = 0.001$, and find a new equilibrium. We do this by iteration, at each step calculating the constant value of the streamfunction ψ on the boundary of the vortex and the correction Ω' to the guess for Ω of the previous iteration. Our convergence criterion is met when the maximum normal variation of the contour shape is less than 10^{-9}. We use cubic-spline interpolation and two-point Gaussian quadrature (see Appendix A of Polvani and Dritschel, 1993, for details) to calculate ψ and Ω'. Once our convergence criterion is met, we then reduce λ further and repeat the procedure until the method no longer converges

(this normally occurs for very small λ between 0.003 and 0.007, depending on γ). This generates a family of equilibria varying with λ for a fixed value of γ. Note that we generate both stable and unstable steady states. To start the procedure, we need a guess for the rotation rate Ω relevant to a near circular vortex ($1 - \lambda \ll 1$). From a linear stability analysis (see Appendix A), it can be shown that for an m-fold symmetric wave $\Omega = \mathrm{I}_1(\gamma)\mathrm{K}_1(\gamma) - \mathrm{I}_m(\gamma)\mathrm{K}_m(\gamma)$, where I_m and K_m are the modified Bessel functions of the m^{th} order. Note that we confine our attention to $m = 2$.

Typically, 400 nodes are used to represent the vortex boundary $\mathcal{C}$. These are connected together by local cubic splines to achieve high accuracy, and are distributed proportionally to the square root of of the local curvature, as discussed in Dritschel (1988). 800 nodes are used when $\gamma > 1$, in part to accurately capture the weak instability occurring for very small λ (when the vortex is strongly distorted), and in part for long-time accuracy in the nonlinear simulations (the evolution slows down markedly as γ increases beyond 1, see below). The difference in the vortex shape between 400 and 800 nodes, however, is much smaller than the line width plotted in figure 2.2.

We generate families of equilibria for $\gamma = 0.02$, 0.25, 0.5 and thereafter in increments of $\Delta\gamma = 0.5$ to $\gamma = 10$ (22 families in total). This range more than sufficiently encompasses the range of values thought to characterise vortices in the oceans, the atmosphere and in other planetary atmospheres. Note that the barotropic case corresponds to $\gamma = 0$.

2.2.3 Properties of the equilibria

A few examples of the equilibrium contour shapes are presented for three different values of γ in figure 2.3, which is complemented by supplementary movie 1. In each frame, we illustrate three different aspect ratios: $\lambda = 0.5$, the aspect

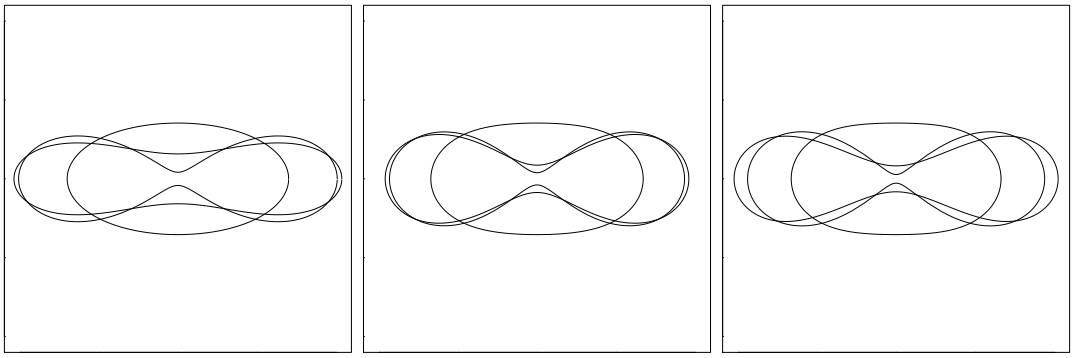

Figure 2.3: Selected equilibrium contour shapes for $\gamma = 0.5$ (left), 3.0 (middle), and 8.0 (right). In each frame, we show the equilibrium contours for $\lambda = 0.5$, for the smallest stable aspect ratio λ_c, and for the smallest aspect ratio attainable λ_f. The plot window is the square $|x|, |y| \leq 2.2$. See also supplementary movie 1.

ratio at marginal stability λ_c (see §2.3), and the smallest aspect ratio for which we achieve convergence λ_f. Here, and for all γ investigated, the shape deforms into a dumbbell shape, nearly pinching off as $\lambda \to 0$. Note that the corner formed as $\lambda \to 0$ is infinitesimally-small-scale, and is controlled by local dynamics. Non-zero γ states therefore have the same behaviour as the barotropic $\gamma = 0$ case, i.e. a right-angle corner is formed; this is studied in detail by Overman II (1986). It is likely that the limiting form for $\lambda = 0$ is a pair of vortices touching at the origin (see Polvani et al. (1989) for comparable examples of doubly-connected equilibria). Note that at large γ, the equilibria become less elongated in x with decreasing λ. This is due to the shortening interaction range, proportional to L_D, as γ increases. As $\gamma \to \infty$, the limiting form for $\lambda \to 0$ is likely to be two circular patches joined by a bridge at a distance $r = \mathrm{O}(L_D)$ from the origin.

There is a gradual transition from quasi-elliptical equilibria with λ close to 1 to dumbbell-shaped equilibria for small λ. This is quantified in figure 2.4 by comparing λ with the elliptical aspect ratio λ_e obtained from the second-order spatial moments of the vortex-patch. For the barotropic Kirchhoff family of equilibria at $\gamma = 0$, each member is an ellipse, hence $\lambda = \lambda_e$. As γ increases, λ_e peels away from this line at progressively larger λ: this indicates

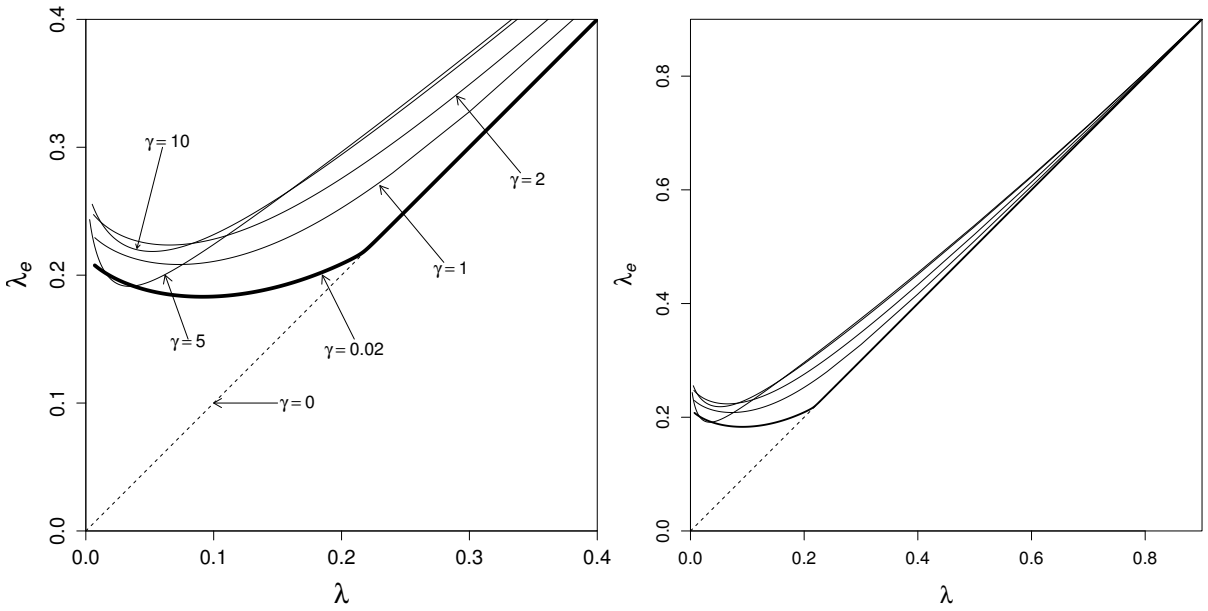

Figure 2.4: Comparison of the aspect ratio λ and the elliptical aspect ratio λ_e, obtained from the second spatial moments, $\iint x^2 \mathrm{d}x\mathrm{d}y$ and $\iint y^2 \mathrm{d}x\mathrm{d}y$ of the vortex-patch. The equilibrium families $\gamma = 1$, 2, 5 and 10 are shown by thin lines, the family $\gamma = 0.02$ by a bold line, and the barotropic Kirchhoff family $\gamma = 0$ by the dashed line. The curve for $\gamma = 10$ displays the most distortion for small λ. On the left we see a zoom of the figure on the right.

that the vortex is becoming dumbbell-shaped. The family for $\gamma = 0.02$, which is close to barotropic, evidently exhibits a bifurcation around $\lambda = 0.21$. For $\lambda > 0.21$, the equilibria are very close to elliptical in shape, but for $\lambda < 0.21$, they become dumbbell shaped, like all the other non-zero γ families. This bifurcation is associated with a known bifurcation occurring in the barotropic family at $\lambda = \lambda_4 = 2^{1/2} + 1 - 2(2^{1/2} + 1)^{1/2} = 0.216845....$ This point coincides with the margin of stability for a wave-4 disturbance, see Love (1893) and Dritschel (1986). Moreover, Kamm (1987); Cerretelli and Williamson (2003a) and Luzzatto-Fegiz and Williamson (2010) have shown that there are two new branches of equilibria splitting off from the elliptical branch at $\lambda = \lambda_4$. One branch is dumbbell-shaped, while the other is eye-shaped (more pointed at the extremities). For non-zero γ, *only* the dumbbell-shaped equilibria are connected by continuous deformations to circular equilibria at $\lambda = 1$. The eye-shaped equilibria presumably still exist, at least for small γ, but they lie on an isolated branch in the parameter space, and so cannot by accessed by the numerical method used in this study. Elliptical equilibria, if they exist for $\lambda < 0.21$ for non-zero γ, also cannot by accessed by continuous deformations from circular shapes. The apparent bifurcation occurring at small γ near $\lambda = \lambda_4$ is clearly visible in the particle rotation rate $\Omega_p = 2\pi/T$, where $T = \oint_{\mathcal{C}} ds/|\boldsymbol{u}|$ and s is arc length (Ω_p is the average rate at which fluid particles circulate around the boundary), shown in figure 2.5 for the four smallest values of γ examined in this chapter. For $\gamma = 0.02$, we see that Ω_p strongly dips toward $\lambda = \lambda_4$, while as γ increases, Ω_p flattens and there is less sign of the bifurcation. Similar sensitivity is seen in the linear stability of the equilibria, discussed below in §2.3.2.

Further properties of the equilibria are shown in figure 2.6 as a function of γ and λ. In 2.6(a) we have the angular impulse $J = q_0 \iint_{\mathcal{D}} (x^2 + y^2) \mathrm{d}x\mathrm{d}y$, where $\mathcal{D}$ is the region inside the vortex-patch, in (b) the total energy $E = -(q_0/2) \iint_{\mathcal{D}} \psi \, \mathrm{d}x\mathrm{d}y$ (see Appendix B), in (c) the rotation rate Ω, and in (d) the particle rotation rate

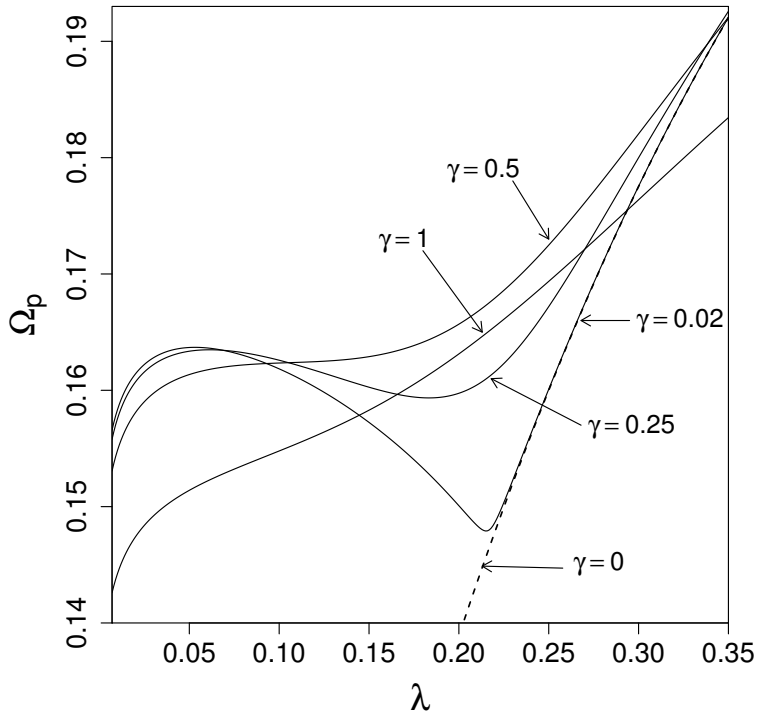

Figure 2.5: The dependence of the particle rotation rate Ω_p on aspect ratio λ for several small values of γ. The dashed line corresponds to the $\gamma = 0$ case, where $\Omega_p = \lambda/(\lambda + 1)^2$ (Dritschel, 1990).

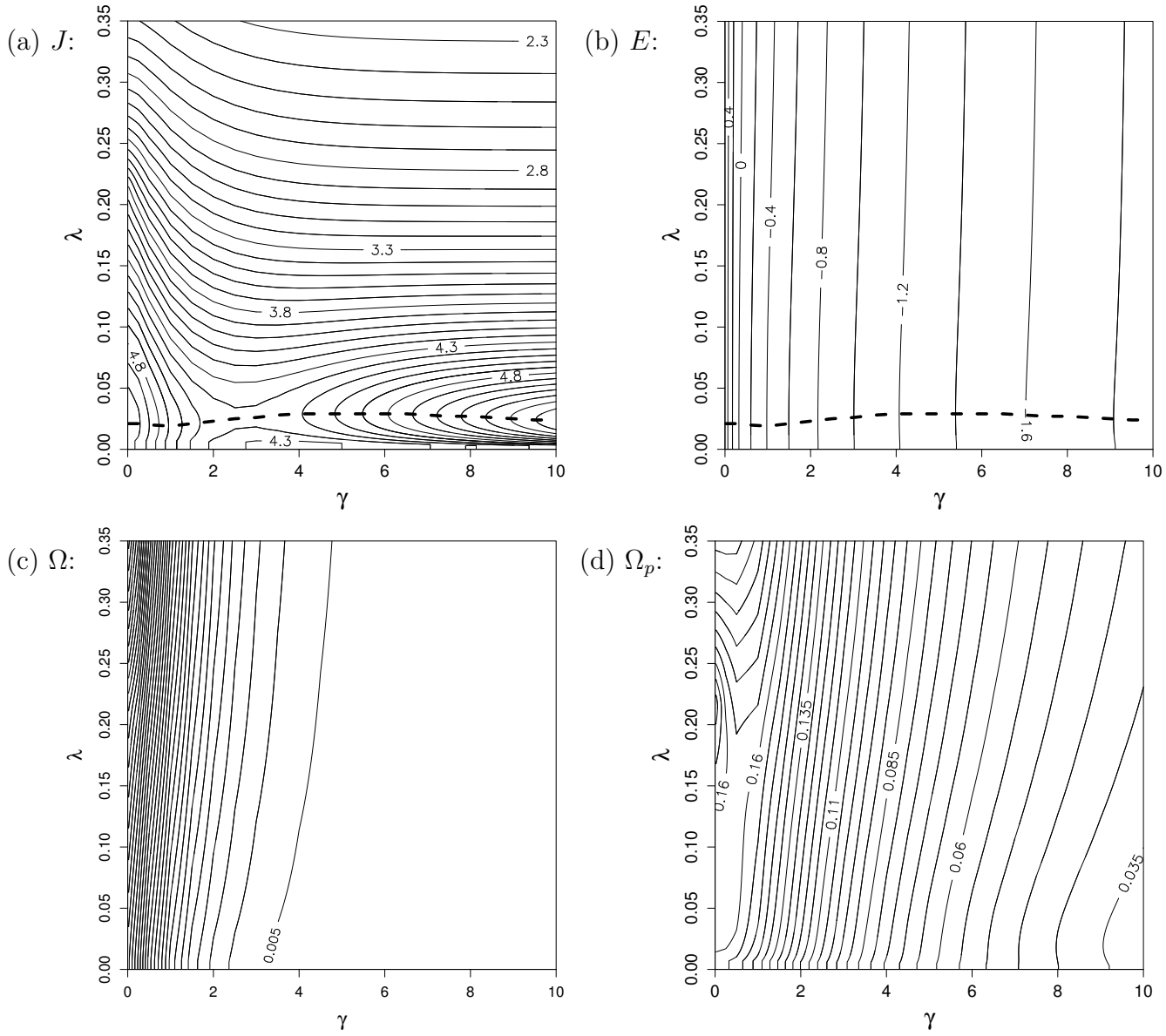

Figure 2.6: Various properties of the equilibria in the $\gamma - \lambda$ parameter plane: (a) angular impulse J (contour interval 0.1), the dashed line shows the maximum of J for each γ; (b) total energy E (contour interval 0.2, $\log_{10}$ scaling), the dashed line shows the minimum of E for each γ; (c) rotation rate Ω (contour interval 0.005); and (d) particle rotation rate Ω_p (contour interval 0.005).

Ω_p. Note that the barotropic Kirchhoff family is *not* represented at $\gamma = 0$; rather we use the numerically generated family for $\gamma = 0.02$, which at small λ is dumbbell-shaped like all other families. Turning first to the angular impulse J and energy E, for every γ considered we find that J exhibits a maximum at the same point λ where E exhibits a minimum (this is marked by the dashed line in 2.6(a) and 2.6(b)). By contrast, J and E are monotonic in λ for the barotropic Kirchhoff family.

If we plot E as a function of J, we generally find two branches of solutions joined at a cusp, as illustrated in figure 2.7 for the $\gamma = 4$ family (all other families are qualitatively similar). Saffman and Szeto (1980) and Saffman (1992) argued that, under these circumstances, the upper branch is linearly stable while the lower branch is unstable (see Dritschel, 1985, for why this argument is incomplete). Saffman and Szeto (1980) studied the $\gamma = 0$ case, but their results are also valid for $\gamma \neq 0$. The joint extremum of J and E at $\lambda = \lambda_c$ thus coincides with the margin of stability. Dritschel (1995) has shown that for a pair of liked-signed, unequal-sized barotropic vortices, the joint extremum of J and E does indeed coincide with the margin of stability. On the other hand, it does not when the vortices are opposite-signed. Notably, at marginal stability $\lambda = \lambda_c$, the linear eigenmode has exactly zero frequency (and growth rate), indicating the existence of multiple branches of equilibria. Here, consistent with this picture, there are two branches, a lower and an upper one stemming from a cusp in the $E(J)$ diagram. The same situation occurs for like-signed barotropic vortices, discussed in Dritschel (1995).

The linear stability analysis for QGSW vortex-patches below confirms this behaviour, albeit for only one of the two modes of instability found. This mode has the same symmetry as the equilibria found here, but it is not the first to become unstable for $\gamma \lesssim 3$. Moreover, this mode does not exist for $\gamma = 0$; then the angular impulse varies monotonically with λ (for further discussion, see

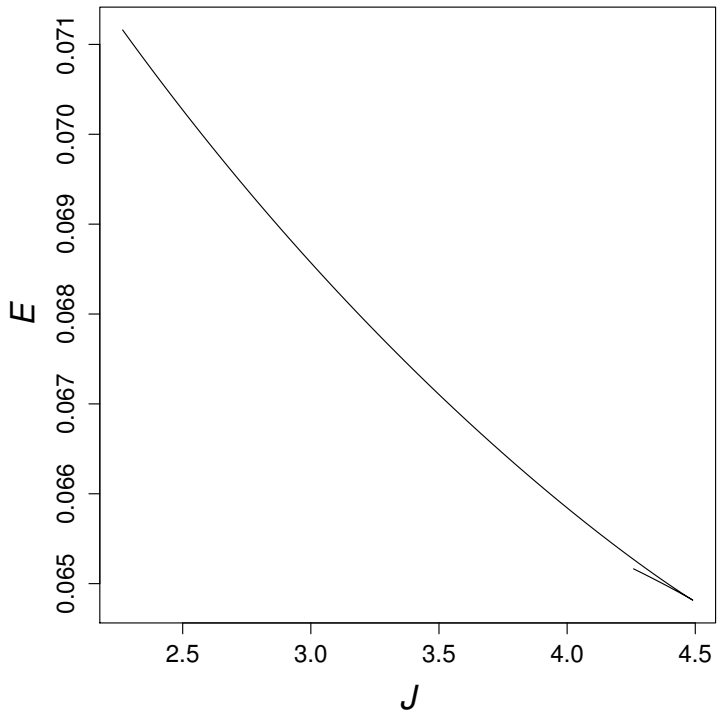

Figure 2.7: The total energy E plotted as a function of angular impulse J for the $\gamma = 4$ family of solutions. The smallest λ values occur on the lower branch at the bottom right of the figure.

Dritschel, 1995, and Luzzatto-Fegiz and Williamson, 2010).

The rotation rate Ω of the vortex and the particle rotation rate Ω_p around its boundary in figures 2.6(c) and (d) both strongly decrease with increasing γ and, to a lesser extent, decrease with decreasing λ. Note that $\Omega_p \gg \Omega$ for large γ. In this part of parameter space, the fluid velocity induced by the vortex is confined to a narrow belt of $O(L_D)$ width, and to leading order the velocity on the contour is $\sim q_0 L_D/2$ (Nycander et al., 1993). This implies $\Omega_p \sim q_0 L_D/2P$, where P is the arc length (a circular patch has $P = 2\pi$), a relationship which holds to within 3% for $\gamma = 10$. On the other hand, the equilibrium rotation rate Ω depends on exponentially-small long-range interactions, and is therefore much smaller in magnitude. If we regard the equilibrium as a solitary wave solution with maximum curvature κ then, following Nycander et al. (1993), the predicted value of Ω is $q_0(\kappa L_D)^3/32$. Figure 2.8 shows $\Omega\gamma^3$ versus γ for $\lambda = 0.5$ (note $q_0 = L = 1$). For this aspect ratio, the equilibria are nearly elliptical, so we can estimate $\kappa \approx \lambda^{-3/2} = 2\sqrt{2}$. This implies $\Omega\gamma^3 \to 1/\sqrt{2} \approx 0.7071$ as $\gamma \to \infty$, which appears to be a plausible estimate.

2.3 Linear stability

We next examine the linear stability to normal-mode disturbances of the vortex-patch equilibria presented in §2.2. We briefly review the method used in §2.3.1, and then discuss our findings in §2.3.2.

2.3.1 Method

We next perform a linear stability analysis of the families of equilibria described above using a method first used by Dritschel and Legras (1991) and fully described in Dritschel (1995). In this method, we displace the equilibrium PV

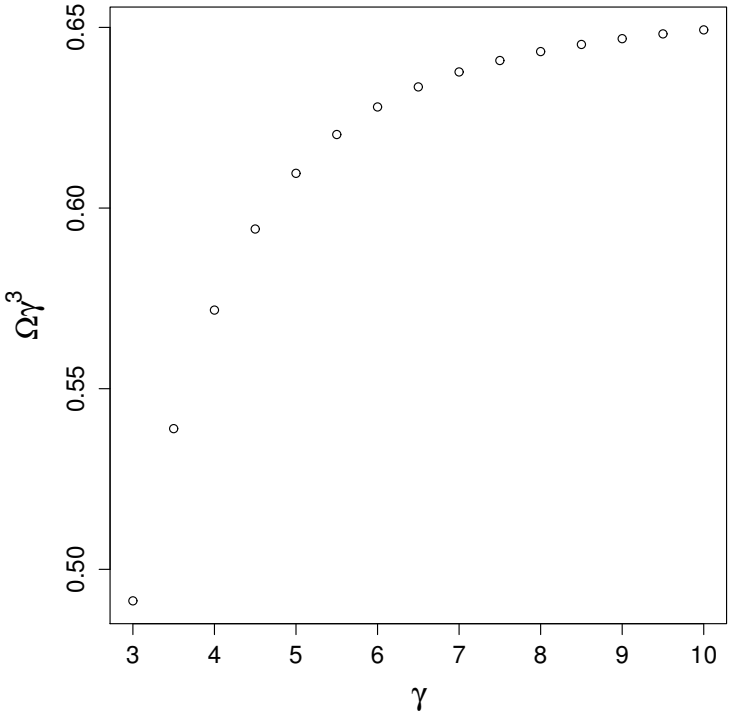

Figure 2.8: The scaled equilibrium rotation rate $\Omega\gamma^3$ versus γ for $\gamma = 3$–10, at $\lambda = 0.5$.

contour by arbitrarily infinitesimal amounts which are normal to the contour, i.e.

$$\boldsymbol{x}(\phi, t) = \boldsymbol{x}_e(\phi) + \eta(\phi, t)\frac{\{\mathrm{d}y_e/\mathrm{d}\phi, -\mathrm{d}x_e/\mathrm{d}\phi\}}{(\mathrm{d}x_e/\mathrm{d}\phi)^2 + (\mathrm{d}y_e/\mathrm{d}\phi)^2},$$

where the quantities with and without the subscript e refer to the equilibrium and disturbed quantities, respectively. The "disturbance function" η is considered small compared to $\boldsymbol{x}_e$ and so we can linearise the equations of motion. Disturbances having the above form preserve area, but not necessarily the angular impulse J, and can arise under the external action of a weak irrotational field, which may for example result from some distance vortices. In the above, ϕ can be any parametrisation of the contour. Here, for simplicity, we choose it to be proportional to the travel time t of a particle moving around the contour, $\phi = \Omega_{p,k}t$, where $\Omega_{p,k}$ is the particle rotation rate on the kth contour. We thus

obtain the evolution of $\eta_k(\phi_k, t)$ of the kth contour:

$$\frac{\partial \eta_k}{\partial t} + \Omega_{ek} \frac{\partial \eta_k}{\partial \phi_k} = \frac{\partial F_k}{\partial \phi_k},$$

where

$$F_k(\phi_k) \equiv -\sum_{j=1}^{n} \frac{\tilde{\omega}_j}{2\pi} \int_0^{2\pi} \eta_j(\phi_j, t) \mathrm{K}_0 \left(\frac{\boldsymbol{x}_{ek}(\phi_k) - \boldsymbol{x}_{ej}(\phi_j)}{L_D} \right) \mathrm{d}\phi_j,$$

and where n is the total number of contours (here $n = 1$) and $\tilde{\omega}_j$ is the inward vorticity jump across the jth contour (here 1).

The disturbances are expanded in a truncated Fourier series involving $\cos m\phi$ and $\sin m\phi$, where we retain only wavenumbers $m \leq M = 50$. We thus solve a $2nM \times 2nM$ matrix eigenvalue problem for the eigenvalue σ at each λ for fixed γ. We have verified that our results change insignificantly when doubling M, and the results presented below are accurate to within the plotted line width.

2.3.2 Results

The results of the linear stability analysis are presented in figure 2.9, which shows the growth rates σ_r of the two most unstable modes found for the full range of γ considered and for $\lambda \leq 0.35$ (stability is found for all $\lambda > 1/3$, the boundary of stability of barotropic Kirchhoff vortices, Love, 1893). The two modes can be broadly identified as a large-L_D mode ($\gamma \lesssim 3$) found on barotropic Kirchhoff vortices, and a distinct small-L_D mode (dominant for $\gamma \gtrsim 3$). The margin of stability λ_c falls at the $\sigma_r = 0$ contour in the figure. We see that the margin of stability of the small-L_D mode coincides with the maximum of the angular impulse J and the minimum of energy E (cf. figure 2.6(a) and (b)). Here, both the growth rate σ_r and the frequency σ_i are zero, a so-called "exchange-type" instability (see §2 for discussion). On the other hand, the margin of stability of

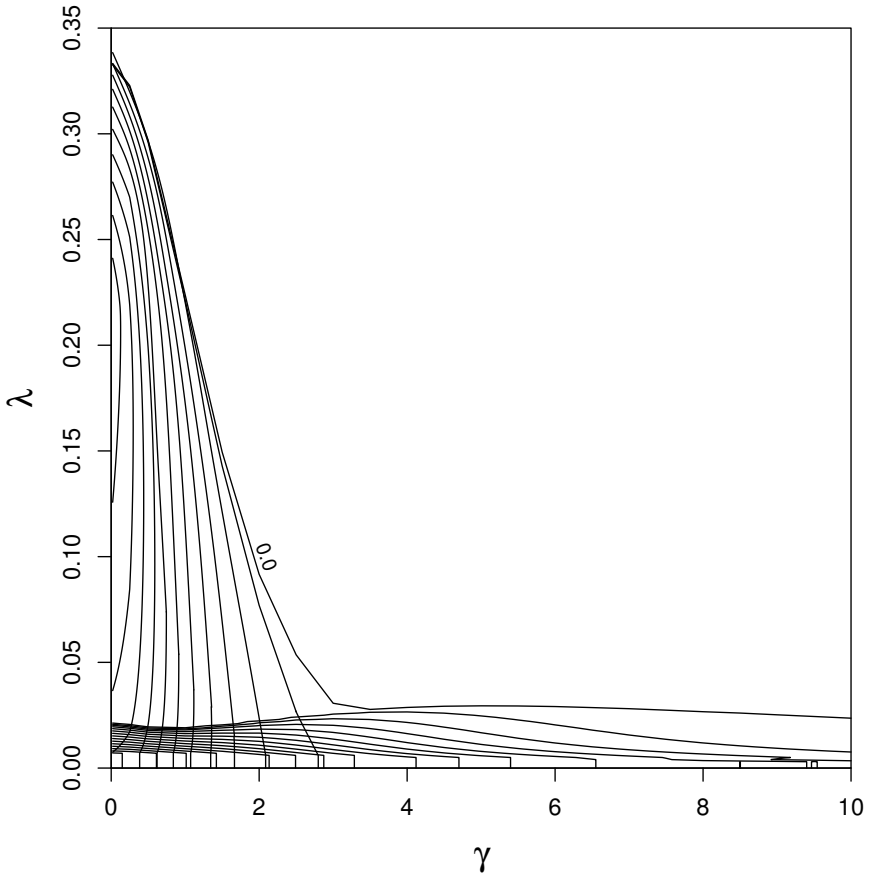

Figure 2.9: Growth rates σ_r of the two most unstable modes in the $\gamma - \lambda$ parameter plane. The contour interval is 0.01.

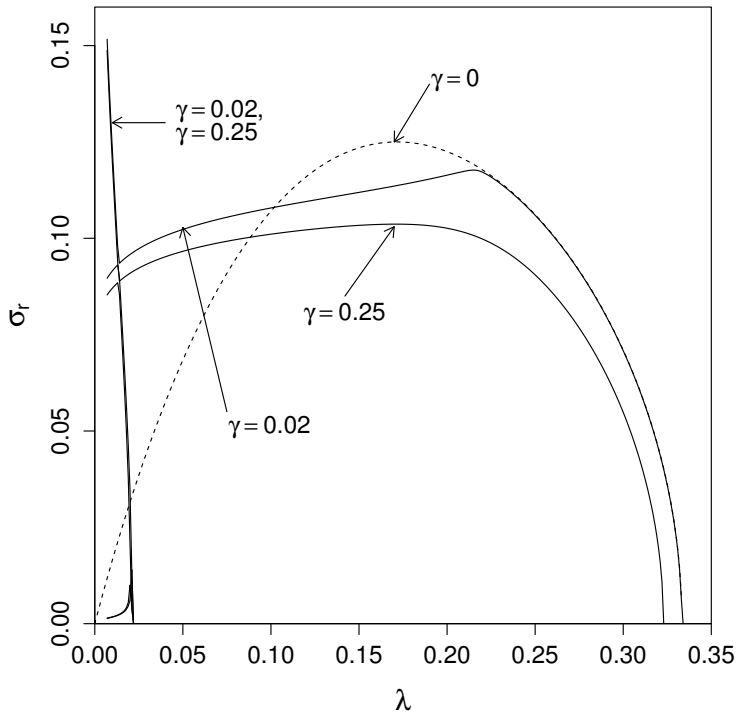

Figure 2.10: The growth rates σ_r of the three most unstable modes for $\gamma = 0.02$ and 0.25. The dashed line corresponds to the analytical prediction of the growth rate for the barotropic case $\gamma = 0$ (Love, 1893; Dritschel, 1986). Note that the third mode is very small and occurs at small λ.

the large-L_D mode does not coincide with either the maximum of the angular impulse J or the minimum of the energy E. This is despite the fact that both σ_r and σ_i are zero at $\lambda = \lambda_c$. Here, it is likely that an additional branch of equilibria without two-fold symmetry splits off from the main solution branch, as found in the analogous barotropic Kirchhoff case (Luzzatto-Fegiz and Williamson, 2010).

Near the barotropic limit $\gamma \ll 1$, we again see evidence of the bifurcation occurring for $\gamma = 0$ at $\lambda = \lambda_4$ in the growth rates of the unstable modes, see figure 2.10. Until roughly $\lambda = 0.22$, the smallest $\gamma = 0.02$ curve hugs the barotropic one, after which it breaks away (the vortex-patch rapidly changes shape through $\lambda = \lambda_4$, cf. figure 2.4). As γ increases, there is a more gradual transition around $\lambda = \lambda_4$.

Figure 2.11 shows the growth rates as a function of λ for three distinct γ values

corresponding to those illustrated in figure 2.3. These γ values are characteristic representatives of large-L_D behaviour ($\gamma = 0.5$ in the figure), small-L_D behaviour ($\gamma = 8$) and the boundary between the two ($\gamma = 3$). For large L_D or small γ (on the left), instability emerges at moderate λ, then plateaus and finally slightly decreases as $\lambda \to 0$. At small λ, a second stronger mode emerges and dominates at very small λ. For intermediate L_D (in the middle), two modes erupt at nearly the same (small) aspect ratio. The first is the large-L_D mode, but this is quickly overwhelmed by the small-L_D mode at smaller λ. For small L_D (on the right), only the small-L_D mode is seen. However, the instability is substantially weaker than in the other two cases. Again, this is due to the weakening of long-range interactions as L_D decreases.

Finally, it is noteworthy that only two modes of instability occur throughout the entire parameter space (with an exceptional third for very small λ and for some γ values)[1]. This stands in sharp contrast to the barotropic Kirchhoff case, where there is an infinite sequence of instability modes (at $\lambda = 1/3$, 0.2168..., etc...) occurring for decreasing λ (Love, 1893; Dritschel, 1986). These modes correspond to wave 3, 4, etc... disturbances, but are evidently not found for $\gamma > 0$, at least for the families of equilibria deformable from circular shapes. The deformation into dumbbell-shaped vortices appears to limit the number of unstable modes (in effect offering greater stability). This appears to explain why we see only the wave-3 instability for small γ near $\lambda = 1/3$, something akin to the wave-4 instability for smaller λ when vortices are dumbbell-shaped, and no other instabilities.

In summary, smaller γ equilibria lose stability at higher λ and have higher growth rates than larger γ equilibria. This means that smaller vortices, for fixed deformation length L_D, destabilise more readily than larger ones.

[1]These modes, which are much weaker than the primary mode of instability, may be associated with additional turning points in the $E(J)$ diagram, as found by Luzzatto-Fegiz and Williamson (2011) in the barotropic context.

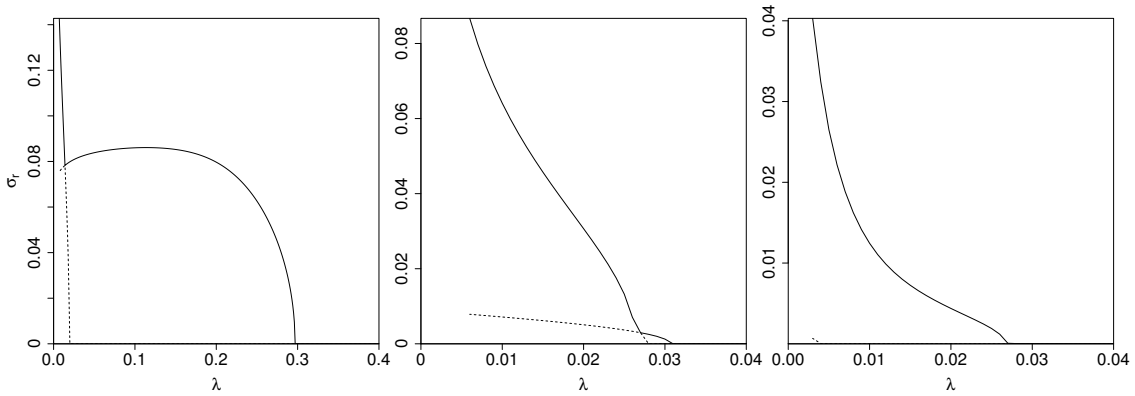

Figure 2.11: The growth rates σ_r of the first (bold line) and second (thin dashed line) most unstable modes, for $\gamma = 0.5$ (left), $\gamma = 3$ (middle) and $\gamma = 8$ (right).

2.4 Nonlinear evolution

We next explore the nonlinear evolution of unstable vortex-patches near the marginal stability boundary found in §2.3. The numerical method is first discussed in §2.4.1, and then various forms of nonlinear evolution are illustrated and mapped in the $\gamma - \lambda$ parameter plane in §2.4.2.

2.4.1 Method

We use the contour surgery algorithm (Dritschel, 1988, 1989) to study the evolution of the boundary of the vortex-patch, including complex processes such as splitting and filamentation. The algorithm solves equation 2.3 numerically by discretising contours into a finite, variable number of nodes, connected together by local cubic splines. The contour integrations are performed semi-analytically for the singular logarithmic part of the K_0 Green function, and by two-point Gaussian quadrature for the non-singular remainder (Dritschel, 1989). Nodes are added, removed and shifted in response to changes in contour curvature. A fourth-order Runge-Kutta time integration method is used with a fixed, standard time step of $\Delta t = 0.025$.

Initially, we start with an equilibrium vortex-patch which is slightly disturbed by randomly displacing the x and y coordinates of each node by 1% of $\Delta\theta = 2\pi/n_0$, where n_0 is the initial number of nodes (400 for $\gamma \leq 1$ and 800 for $\gamma > 1$). This is done so as not to bias the evolution towards either the symmetric or the asymmetric modes. Thereafter, every 8 times steps, the nodes are redistributed using a dimensionless node separation parameter $\mu = 0.2$ and a large-scale length $L_c = P/(\mu n_0)$, where P is the equilibrium arc length. During the evolution (also every 8 time steps), if the distance between two parts of the contour (or between two distinct contours) becomes less than the "cut-off scale" $d_c = \mu^2 L_c/4$, contour surgery is performed (Dritschel, 1988). This either splits a contour into two parts or joins two contours together. The settings for μ, d_c and the frequency of surgery and node redistribution are now standard, and a comprehensive discussion may be found in Fontane and Dritschel (2009), which also generalise to the pure contour dynamics simulations of this study.

We evolve the equilibria typically for 100 particle rotation periods $T_p = 2\pi/\Omega_p$ (based on the equilibrium value of Ω_p, see figure 2.6(d)). A few cases were evolved for longer times (for as long as $500T_p$), and no qualitative differences were found. No vortex splitting occurred later than $91T_p$, with splitting times being highest for $\gamma = 2$ and 3, which were both evolved for at least $200T_p$. Due to computational costs, we examine a subset of equilibria having $\gamma = 0.25, 0.5, 1, 1.5$ and 2 to 10 in increments of unity (13 cases in total). We examine the small γ cases more closely, as there is a steep decrease in λ_c for these values (cf. figure 2.9).

2.4.2 Results

Dritschel (1986) and Tang (1987) found that, for the barotropic case, linear stability of an equilibrium implies nonlinear stability (which, unlike the converse of the statement, is not generally true). For $\gamma > 0$, we find that this statement

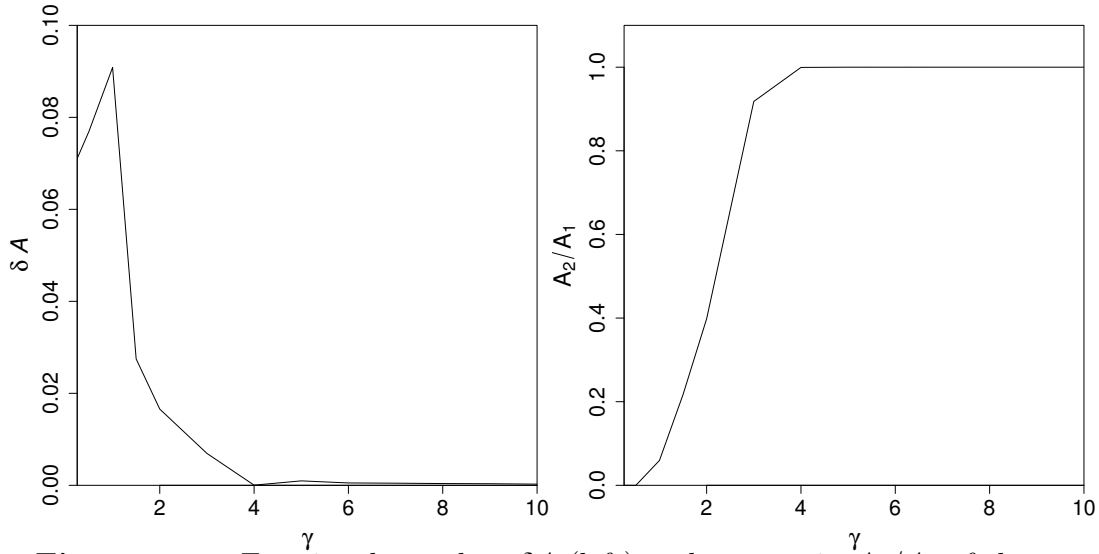

Figure 2.12: Fractional area loss δA (left) and area ratio A_2/A_1 of the second largest to largest patches (right) at the end of the simulation. For each γ, only results for the weakest linear instability near marginal stability ($\lambda \lesssim \lambda_c$) are shown.

remains true, within $\Delta\lambda = 0.001$ in almost all cases. The only exception is the $\gamma = 4$ case, where the stability boundary occurs at an aspect ratio smaller by 0.004 than predicted. This may be due to weak vacillations occurring near the margin of stability in this case, as such vacillations are noticeable for $\gamma = 5$ and 6 (see below).

In almost all cases, these weak linear instabilities near λ_c nevertheless lead to major structural changes in the vortex shape, from filamentation to splitting. Different types of evolution accompany the two main linear modes discussed above, and there are significant variations in these types. In addition to a visual examination, we quantify area changes at late times to better distinguish these types. The first diagnostic is the fractional change in the total area occupied by the largest one or two vortex patches at the end of the simulation,

$$\delta A = 1 - \frac{\sum_{i=1}^{2} A_i}{A_0}, \tag{2.4}$$

where A_1 is the area of the largest vortex-patch and A_2 is the area of the second

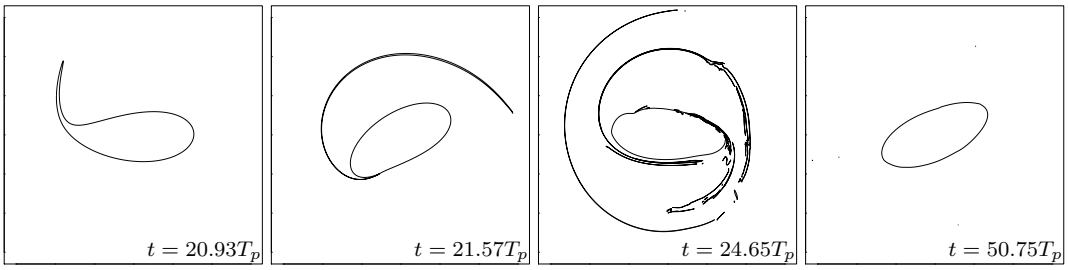

Figure 2.13: Type 2 instability, filamentation. Here we illustrate the case for $\gamma = 0.5$ and $\lambda_c = 0.296$. Note that $|x|, |y| \leq 3.3$, and that we are viewing the state in a reference frame co-rotating with the undisturbed configuration in this and subsequent figures. See also supplementary movie 2.

largest one (if present; otherwise $A_2 = 0$). Here, $A_0 = \pi$ is the area of the original vortex-patch. We thus do not include any filamentary debris or smaller vortex patches left over at late times. The second diagnostic is the ratio of vortex areas, $A_2/A_1 \leq 1$, at the end of the simulation.

Three types of instability can be identified by looking at δA and A_2/A_1 in figure 2.12. The first, which we call "type 2" (see below for the "type 1" instability), occurs for states with $\gamma < 1$. Here, we see a peak in δA, and a gradual increase in A_2/A_1 from 0 as γ increases. Visual examination indicates that the vortex destabilises asymmetrically, shedding a large filament which may subsequently roll up into a series of smaller vortices. This behaviour was found previously in the barotropic case (Dritschel, 1986), apart from the vortex roll up, and is directly associated with the instability of a wave-3 disturbance in this case. An example of this evolution, now for $\gamma = 0.5$ and $\lambda = \lambda_c = 0.296$, is illustrated in figure 2.13. (Note that figures 2.13–2.16 are complemented by supplementary movies 2–5). At late times, a single quasi-elliptical vortex-patch remains, whose final aspect ratio is approximately $\lambda = 0.435$ (based on the second-order spatial moments of the patch). This is well within the stable part of the parameter space.

A second type of instability, which we label "type 3i", is apparent for $1 \leq \gamma < 4$: here the vortex splits asymmetrically with little filamentary debris. An example

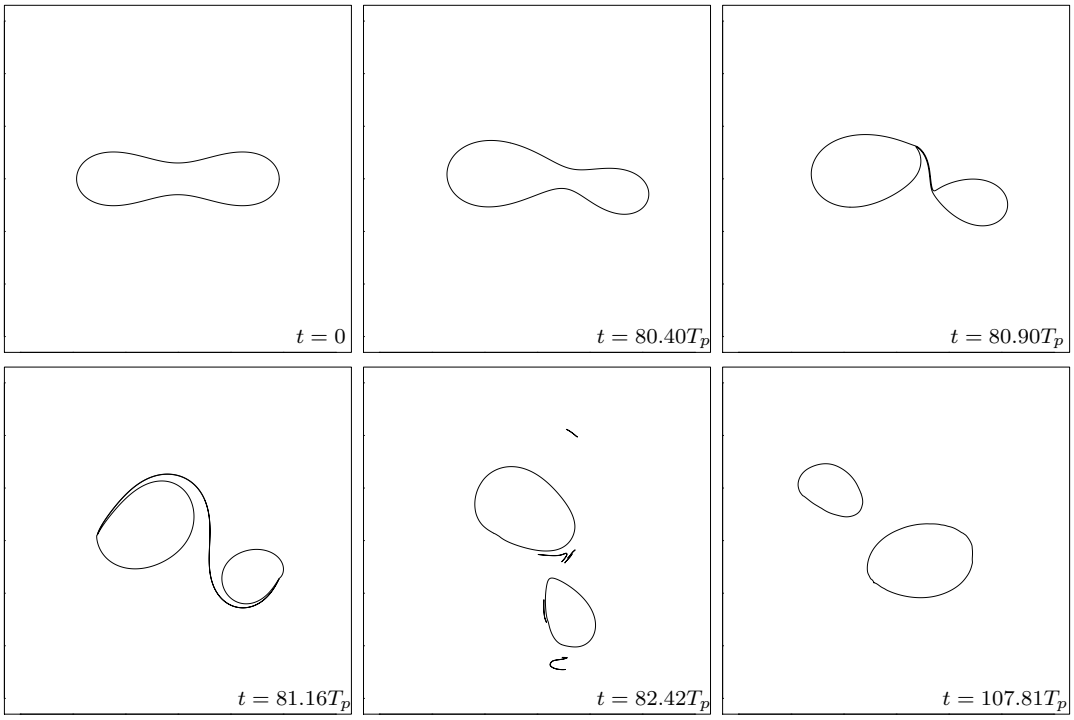

Figure 2.14: Type 3i instability, asymmetric split. Here we illustrate the case for $\gamma = 2$ and $\lambda_c = 0.091$. See also supplementary movie 3.

is illustrated in figure 2.14 for $\gamma = 2$ and $\lambda = \lambda_c = 0.091$. In fact, there is a smooth transition from type 2 to type 3i, accompanied by a significant growth in the area ratio A_2/A_1 and a decay in the area loss δA, as shown in figure 2.12. As γ increases, the initial filament shed from the vortex increases in size, and has a greater tendency to roll up into a single vortex with little debris. This type of instability reflects a competition between the asymmetric small-L_D linear instability mode, and the symmetric large-L_D mode (cf. figure 2.9).

Finally, as γ increases further, the vortex splits almost perfectly into two identical halves, with negligible filaments. This instability, referred to as "type 3ii", is illustrated in figure 2.15 for $\gamma = 10$ and $\lambda = \lambda_c = 0.024$. Such symmetric evolution occurs for $\gamma \geq 4$, and appears directly associated with the symmetric large-L_D linear instability mode. Notice the very slow evolution of the flow, in particular the slow propagation of waves around each vortex boundary (the waves

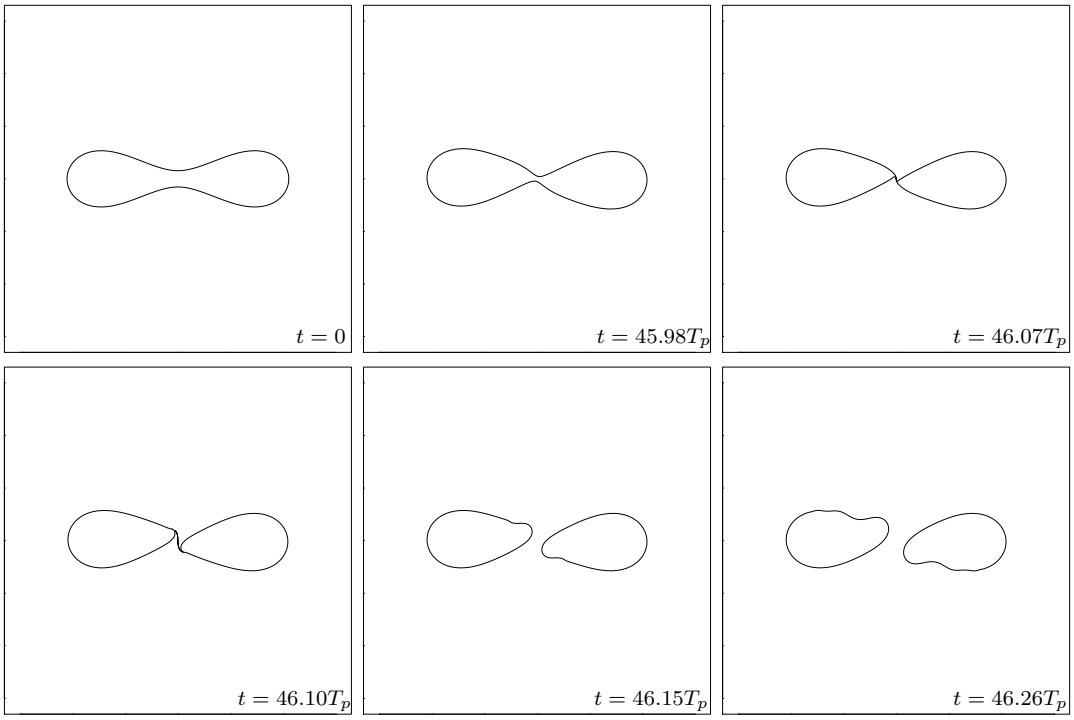

Figure 2.15: Type 3ii instability, symmetric split. Here we illustrate the case for $\gamma = 10$ and $\lambda = 0.024$. See also supplementary movie 4.

in fact obey a modified Korteweg-de Vries equation to leading order in L_D, as explained in Nycander et al., 1993).

After careful scrutiny, we uncovered an additional type of linear instability which is not apparent from figure 2.12. In a small range of aspect ratios near marginal stability for $\gamma = 5$ and 6 only, we observe a vacillating state, an example of weakly nonlinear instability. This instability, here called "type 1" as it is the weakest of all, is illustrated in figure 2.16 for $\gamma = 5$ and $\lambda = 0.024$. We note that λ_c attains a maximum near $\gamma = 5$ for the small-L_D linear instability mode (see figure 2.9), but we are unsure of the significance of this for nonlinear vacillation. Vortices exhibiting type 1 instability begin by tilting, similar to that seen at $t = 45.98T_p$ in figure 2.15), but recover stability by increasing their aspect ratio or widening the bridge between the two halves of the vortex (see $t = 23.76T_p$). By angular momentum conservation, this requires the vortex to

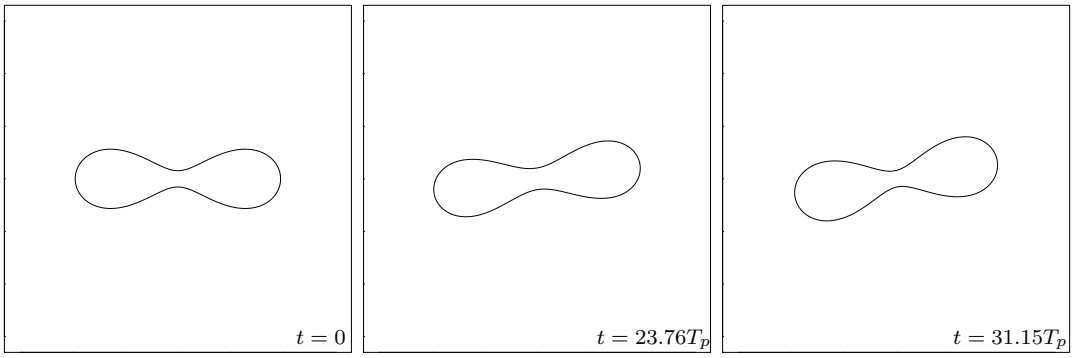

Figure 2.16: Type 1 instability, vacillation. Here we illustrate the case for $\gamma = 5$ and $\lambda = 0.024$. See also supplementary movie 5.

become more extended. Thereafter, the evolution reverses and the initial vortex shape is recovered by $t = 31.15T_p$. The whole process then repeats itself.

A summary of the types of instability occurring near marginal stability is presented in figure 2.17. Note the different scales for λ in the three panels shown. The barotropic case with $\gamma = 0$ is also shown, following Dritschel (1986) who found the type 2 instability for $\lambda \leq 1/3$. The large-L_D mode found in figure 2.9 is characterised by the type 2 and 3i instabilities, in which filaments are shed by the equilibrium as it loses stability. The small-L_D mode, on the other hand, has little or no filamentation and results in a split of the equilibrium into two symmetric vortex-patches. The transition from one mode to the other is smooth; each consecutive case with larger γ having the type 3i instability produces a decreasing amount of filaments and two increasingly symmetric vortex patches. There is a division between the types of instabilities which produce filaments and those which do not. Dritschel (1986) found filamentation for the barotropic case, which agrees with our findings for the large-L_D cases. Polvani et al. (1989) observed a suppression of filamentation for large γ in the case of the merger of two nearby patches of equal PV. For $\gamma = 1$ they observed a "roll-up" of the filaments, similar to the formation of a small vortex-patch observed here at the same value of γ (cf. figure 2.12). For $\gamma = 3$ they noted a complete suppression of filamentation

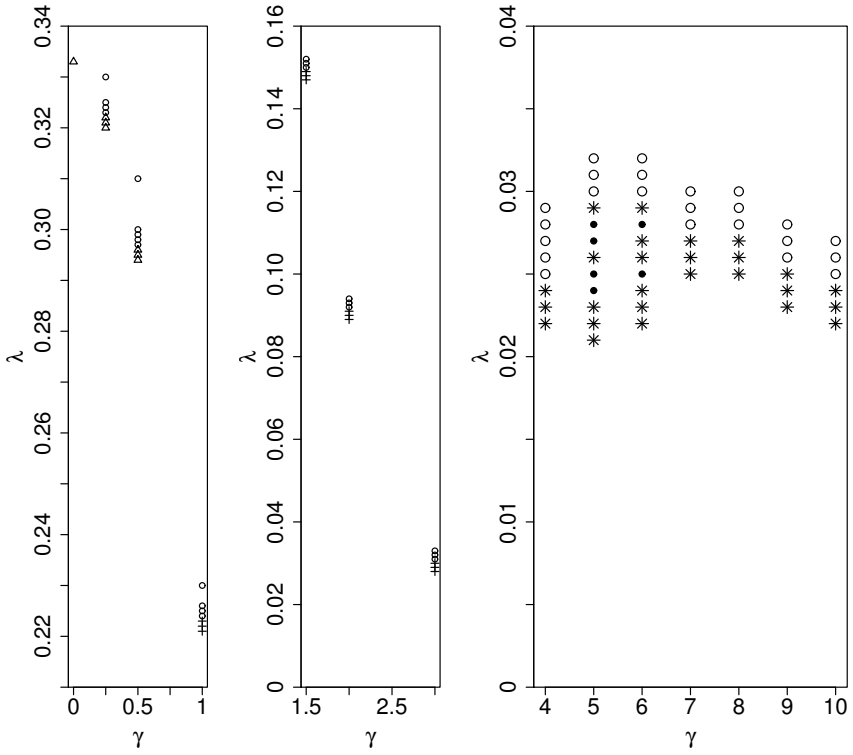

Figure 2.17: Overview of the simulations carried out. The symbols denote the following: ∘ stable; • type 1 instability, vacillation; △ type 2 instability, filamentation (with $A_2/A_1 < 0.1$); + type 3i instability, asymmetric split (with $0.1 \leq A_2/A_1 < 0.99$); ∗ type 3ii instability, symmetric split (with $A_2/A_1 \geq 0.99$).

– this is close to the transition from type 3i to type 3ii instabilities observed here (at $\gamma = 3$, we have $\delta A = 0.007$ and $A_2/A_1 \approx 0.93$, together with some weak filamentation, but this is much weaker than at $\gamma = 2$, for which we have $\delta A = 0.017$ and $A_2/A_1 \approx 0.4$). For yet larger γ, Polvani et al. (1989) observed large-amplitude non-breaking nonlinear waves propagating on the boundary of the vortex, which also closely parallels our observations following a vortex split. Note that there is a continuous transition between vacillating and unstable states at $\gamma = 5$ and 6. We believe this can be attributed to the sensitivity on λ of the large-amplitude waves travelling on the vortex boundary. When the phases of the waves are slightly out of synch, vacillations, rather than breaking, occurs.

2.5 Conclusions

This chapter has examined the form, stability and long-time nonlinear evolution of two-fold symmetric vortex-patch equilibria in a single-layer quasi-geostrophic shallow-water model. The equilibria depend on two parameters: the ratio γ of the mean vortex radius L to the intrinsic Rossby deformation length L_D, and the ratio λ of the minimum to the maximum width of the vortex. The uniform potential vorticity within the vortex may be taken to be unity, as the induced flow is linearly related to potential vorticity.

We have covered a wide range of the $\gamma-\lambda$ parameter space in detail, extending a previous study by Polvani et al. (1989). We have furthermore carried out a linear stability analysis to locate the margin of stability to within $\Delta\lambda = 10^{-3}$ over a wide range of γ values. Finally, we have examined the nonlinear evolution of marginally unstable vortex equilibria, and associated the types of evolution with the principal modes of linear stability.

There are two principal modes, one occurring for small γ which has its origin in the barotropic problem, when $\gamma = 0$, and another occurring mainly at intermediate to large γ, which appears to be unrelated to the barotropic problem. The first "large-L_D" mode is asymmetric (at least near the margin of stability), and results in the ejection of a large filament in the nonlinear evolution. The second "small-L_D" mode is symmetric, and results in a symmetric split of the vortex patch into two, with negligible filamentary debris. The nonlinear problem proves even richer, as there is mode competition, leading to asymmetric vortex splits for moderate γ, specifically $1 \leq \gamma < 4$. Furthermore, we have found a weak nonlinear instability, vacillation, for some aspect ratio values near the margin of stability when $5 \lesssim \gamma \lesssim 6$ (these uncertainties arise because we have performed simulations only for integer values of γ for $\gamma \geq 1$). This weak instability results in variations of the vortex shape only, with the initial shape recurring from time

to time.

Both modes of linear stability exhibit an "exchange-type" instability where both the real and imaginary parts of the eigenfrequency are simultaneously zero at marginal stability. Saffman (1992) argued that such an instability occurs at an extremum of total energy, and Dritschel (1985, 1995) showed that this occurs at joint extrema of both angular impulse and energy (here for fixed γ) as a function of λ. This we have verified for the second small-L_D mode, but not for the first large-L_D mode. Notably, the small-L_D mode has the same symmetry as the equilibrium, while the large-L_D mode does not. (There are symmetric modes of instability in the barotropic problem at smaller λ, the first occurring at $\lambda = 0.2168...$, that exhibit an "exchange-type" instability yet the angular momentum and energy are monotonic functions of λ in this case. For further elaboration, see Dritschel, 1995 and Luzzatto-Fegiz and Williamson, 2010.)

By way of summary, we have found that for a fixed vortex aspect ratio λ and Rossby deformation length L_D, small vortices are likely to be more unstable than large vortices. Put another way, large vortices can sustain much greater deformations before destabilising than small vortices.

2.6 Supplementary movies

Supplementary movies are available on the compact disc attached to this thesis in the folder SC, with movie captions available in Appendix C.1.

Chapter 3

Quasi-geostrophic shallow-water doubly-connected equilibria

The following chapter consists of a study, Płotka and Dritschel (2013), published in the *Journal of Fluid Mechanics* and the work is reproduced here with minor modifications.

3.1 Introduction

The study of two-dimensional vortex dynamics has received considerable attention over the past few decades, largely because of its relevance to geophysical flows. It has been approached from two different perspectives, the first of which has been to directly examine the vortex-dominated processes in realistic geophysical phenomena (e.g. Hoskins et al., 1985; McIntyre, 1993; Carton, 2001). The second has arisen from the study of two-dimensional turbulence which, especially at late times, is dominated by widely-separated vortex structures within a sea of filamentary debris (see e.g. Fornberg, 1977; McWilliams, 1984; Santangelo et al., 1989; Dritschel et al., 2008, and references therein).

Understanding vortex interactions both qualitatively and quantitatively is key in both of these approaches. The majority of studies performed to date have concentrated on vortices of equal size and strength (Zabusky et al., 1979; Saffman and Szeto, 1980; Polvani et al., 1989; Waugh, 1992; Dritschel, 1986, to name a few). However, exact symmetry is rare in realistic flows, and even slight departures from it have been shown to change the nature of the vortex interactions (see §5.1 of Dritschel, 1995). A few studies have examined the asymmetry in size (Melander et al., 1987; Dritschel and Waugh, 1992; Dritschel, 1995; Mitchell and Driscoll, 1996), strength (Yasuda and Flierl, 1995), or both (Trieling et al., 2005; Makarov and Kizner, 2011), and, in short, the variety of different forms of behaviour is remarkably rich.

The goal of the present chapter is to extend the work of Dritschel (1995) and Polvani et al. (1989). The former studied two-dimensional asymmetric doubly-connected equilibria, and examined their linear and nonlinear stability. The latter examined the form of symmetric doubly-connected states at finite L_D and found the critical distance between the two vortices for merger to occur. We go further and examine the effects of finite L_D on the form, properties, linear and nonlinear stability of doubly-connected co-rotating vortex equilibria, aiming also to quantify and describe their nonlinear interactions.

The chapter is organised as follows. In §3.2 we present the theoretical and numerical framework for generating the equilibria, and discuss their form and properties; in §3.3 we perform a full linear stability analysis of the equilibria, and in §3.4 we examine their nonlinear stability and evolution. In §3.5 we examine the transitions between simply- and doubly-connected equilibria, and finally we draw some conclusions in §3.6. Note that information on supplementary movies may be found in §3.7.

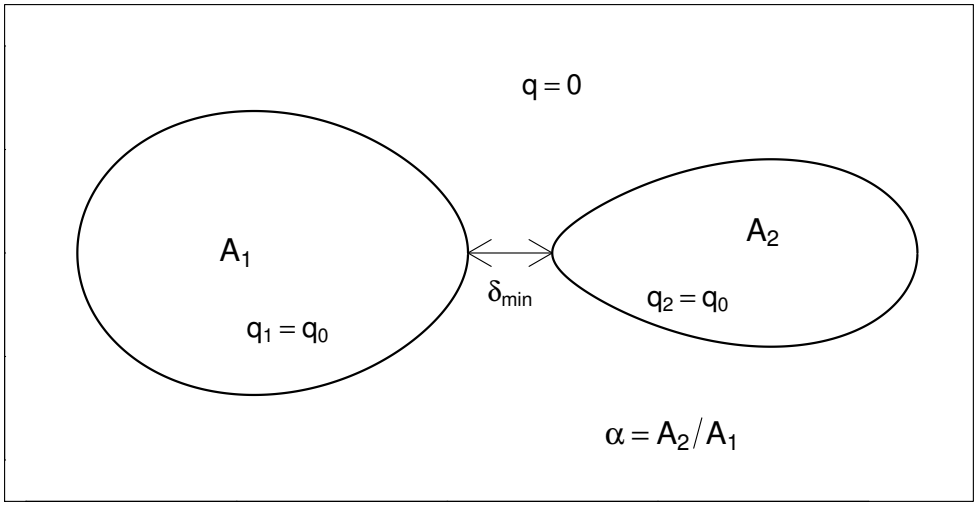

Figure 3.1: Schematic diagram of the doubly-connected equilibria.

3.2 Flow model and properties of the equilibria

3.2.1 Quasi-geostrophic shallow-water flow and the vortex-patch model

The quasi-geostrophic shallow-water model (cf. Pedlosky, 1979) has been widely applied to study fundamental features of atmospheric and oceanic dynamics. We refer the reader to §2.2.1 for full details of it, and here describe its specific application in this chapter.

By considering the single-layer form of the model on the f-plane, we look for equilibrium solutions of two vortex patches of uniform and equal PV $q_1 = q_2 = q_0$ in an unbounded domain having $q = 0$, as shown in figure 3.1. Although very simple in form, vortex patches are a good approximation of realistic high-Reynolds-number flows, as these commonly exhibit vortices with steep PV gradients on their boundaries, having near-uniform values of PV within their core (see e.g. Melander et al., 1987; Legras and Dritschel, 1993; Dritschel, 1993). By employing a formulation now termed "contour dynamics", Deem and Zabusky (1978a,b)

showed that the dynamics of vortex patches, which can be determined from the superposition of their induced velocities, is determined wholly by the shape of their bounding contours. For k regions of constant potential vorticity in irrotational flow, the velocity field is determined from the contour integral

$$\frac{\mathrm{d}\boldsymbol{x}}{\mathrm{d}t} = \boldsymbol{u}(\boldsymbol{x}) = \sum_k \frac{q_k}{2\pi} \oint_{\mathcal{C}_k} \mathrm{K}_0(|\boldsymbol{x} - \boldsymbol{x_k}|/L_D)\mathrm{d}\boldsymbol{x_k}, \tag{3.1}$$

where K_0 is the modified Bessel function of zeroth order, $\mathcal{C}_k$ is the bounding contour of each patch k, drawn in a right-handed sense, q_k is the inward jump of PV across $\mathcal{C}_k$, and $\boldsymbol{x_k} \in \mathcal{C}_k$, as generalised to multiple contours by Dritschel (1989). This is obtained by using Stokes' theorem on the double integral involved in inverting $\nabla^2 - L_D^{-2}$ in equation 2.2. When $\boldsymbol{x} \in \mathcal{C}_j$ also, this equation fully describes the motion of each contour $\mathcal{C}_j$.

We set $k = 2$ in equation 3.1 and seek families of asymmetric doubly-connected equilibria. In this configuration, the families are completely spanned by three dimensionless parameters: (1) their size relative to the Rossby deformation length $\gamma = L/L_D$, (2) the ratio between the areas of the smaller and the larger vortex $0 < \alpha = A_2/A_1 \leq 1$, and (3) the distance δ_{min} between the innermost edges of the vortices.

Using a modification (Dritschel, 1985, 1995) of the iterative scheme first used by Pierrehumbert (1980), we generate asymmetric doubly-connected co-rotating vortex equilibria. Without loss of generality, we set $q_0 = 1$ (giving $q_1 = q_2 = 1$) and $A = A_1 + A_2 = \pi$, where $A_1 \geq A_2$. This prescribes the areas $A_1 = \pi/(1+\alpha)$ and $A_2 = \alpha\pi/(1+\alpha)$ of each of the vortices in terms of the area ratio between them. Throughout this chapter the sub- and superscripts 1 and 2 will be used to distinguish between the larger and smaller vortices, which, without loss of generality, in equilibrium we set to be on the left-hand and right-hand side of the state, respectively (cf. figure 3.1).

For each α, we begin the iterative procedure with a first guess for the equilibrium shapes, namely two circular vortices at a sufficiently large distance δ_{min} apart, proportional to $2/\gamma$. For this guess we approximate the rotation rate of the equilibrium to be that of two point vortices located at the centre of each patch, namely $\Omega = \gamma \mathrm{K}_1(\gamma d)/2d$, where K_1 is the modified Bessel function of the first order and $d = \delta_{min} + r_1 + r_2$ is the distance between the centroids of the vortices. We then progressively decrease the distance δ_{min} by $\Delta\delta_{min} = 0.001$, at each step finding a solution for the boundaries of the vortices and the rotation rate Ω until convergence, here when the maximum normal variation of the contour shapes is less than 10^{-7}. At each step of the iterative procedure, we use cubic-spline interpolation and two-point Gaussian quadrature to calculate the constant value of the streamfunction on the boundary of each of the vortices and the correction Ω' to the rotation rate Ω (full details of how these are calculated may be found in the appendix of Polvani and Dritschel, 1993). We continue this procedure until we reach a final distance δ_f after which we either fail to obtain convergence, or a numerical artefact in the form of a "spike" appears (see Wu et al., 1984, for more details on this). The value of δ_f is dependent on both γ and α: as an example, for $\alpha = 0.2$ for various γ, we find $0.013 \leq \delta_f \leq 0.647$ (with δ_f decreasing as γ increases), while for $\alpha = 1.0$, we find $\delta_f = 0.001$ for all γ.

To obtain the high levels of accuracy in the equilibrium shapes necessary for solving the linear stability problem (see §3.3), we use 200 nodes to represent half of the boundary of each of the vortices, distributed proportionally to the square root of the local curvature. Note that the iterative scheme fixes the global centroid of the equilibria at $(x, y) = (0, 0)$, and enforces symmetry about the x-axis, so that we have to compute only half of the boundary of each vortex.

We seek families of doubly-connected equilibria for a range of α and γ. We generate barotropic-like families with small $\gamma = 0.02, 0.25$, and 0.5, and families which increasingly depart from barotropy, $\gamma = 0$, with $\gamma = 1 - 3.5$ at $\Delta\gamma = 0.5$

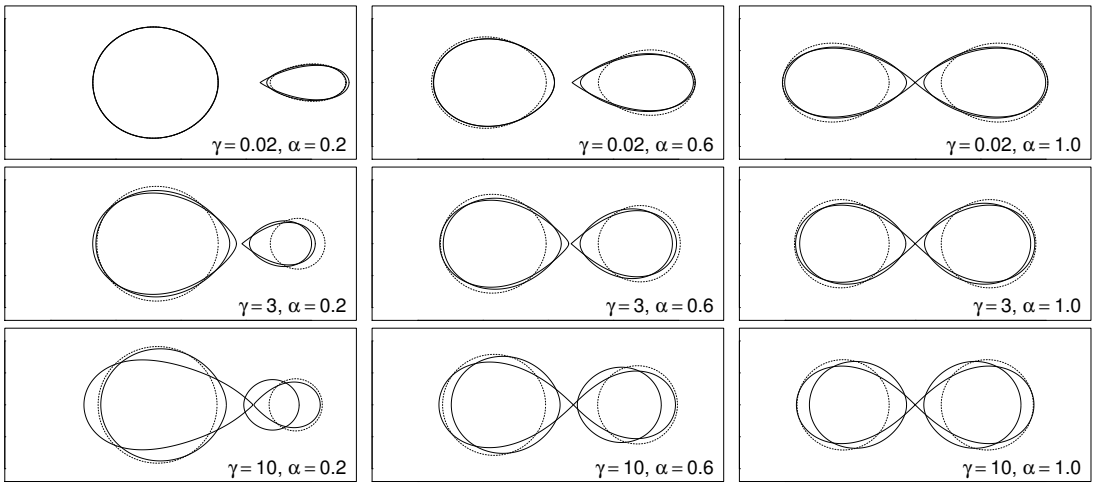

Figure 3.2: Examples of doubly-connected vortex equilibria. For each case we show the distances $\delta_{min} = 0.8$ (dashed line), the critical distance $\delta_{min} = \delta_c$ (bold line), and the smallest distance attained $\delta_{min} = \delta_f$ (thin line). Note, $|x| \leq 2.7$, $|y| \leq 1.2$. In these and subsequent figures we are in a frame of reference rotating with the equilibria. See also supplementary movie 1 for the case $\alpha = 0.2$.

and $\gamma = 4-10$ at $\Delta\gamma = 1$. A denser range of families is necessary at smaller γ, as the equilibria depart from barotropy quickly, but once a critical value of $\gamma \approx 3$ is reached, differences between them are small. The range of γ examined provides a good description of the variety of motions found in geophysical contexts (Charney and Flierl, 1981; Carton, 2001; Scott and Polvani, 2008). For each γ, we examine $\alpha = 0.1 - 1.0$ at $\Delta\alpha = 0.1$. Note that Dritschel (1995) has studied in detail the case $\gamma = 0$, which is omitted in this chapter (we instead examine $\gamma = 0.02$ for comparison), for a range of α, while Polvani et al. (1989) examined families of equilibria for a range of γ at $\alpha = 1.0$, but did not address the problem of their stability.

3.2.2 Properties of the equilibria

Several examples of how equilibrium contour shapes change with γ and α are shown in figure 3.2 (and in supplementary movie 1). For each value of γ (0.02, 3, and 10), we show three different α: a highly-asymmetric state with $\alpha = 0.2$, a

moderately-asymmetric state with $\alpha = 0.6$, and a symmetric state with $\alpha = 1.0$. For each (γ, α), we show three distances: a "large" distance $\delta_{min} = 0.8$, the critical distance $\delta_{min} = \delta_c$ at the boundary of stability (see §3.3), and the smallest distance $\delta_{min} = \delta_f$ attained. We see that as the distance decreases, the vortices become increasingly deformed, until either one or both of them develop a sharp corner. For fixed γ, as α increases, the vortices are able to move closer and closer together before either δ_c or δ_f is reached. Also, the smaller vortex tends to be more deformed than the larger one, with this most pronounced for small α. Deformations of equal-sized vortices are symmetric. As γ increases both δ_c and δ_f decrease, and so despite the weakening of long-range interactions, even for small α the shapes of both of the vortices are affected by each others' presence. Across all α, we see that when $\delta_{min} = 0.8$, the vortices are nearly unaffected by each other for $\gamma = 3$ and 10, in contrast to what is seen from the elongated form of the vortex at $\gamma = 0.02$. For the $\gamma = 10$ equilibria, even at $\delta_{min} = \delta_c$ the shape of each vortex is hardly changed from a circular form. At $\delta_{min} = \delta_f$, despite having moved closer together at a single point, the larger vortex appears to push the smaller one away, while at the same time deforming considerably. Note that it is the local dynamics which control the corner formed in the limiting (small δ_{min}) states, and so the $\gamma = 0$ results of Overman II (1986), who found that a right angle corner is formed, apply to the $\gamma \neq 0$ states.

Further properties of the equilibria are exhibited in figure 3.3 for each of the five area ratios, $\alpha = 0.2$, 0.4, 0.6, 0.8, and 1.0 (rows 1–5 of the figure, respectively) in the $\gamma - \delta_{min}$ parameter plane. In column (1) we show the angular impulse $J = q_0 \iint_{\mathcal{D}} (x^2 + y^2) \mathrm{d}x\mathrm{d}y$, where $\mathcal{D}$ is the region inside the vortex patches, in (2) the total energy $E = -(q_0/2) \iint_{\mathcal{D}} \psi \, \mathrm{d}x\mathrm{d}y$, with ψ the streamfunction, and in (3) the rotation rate Ω. Note that the barotropic families of equilibria are not included, and instead the nearly barotropic case $\gamma = 0.02$ is used.

We first examine J and E. For each γ considered we find that there is a

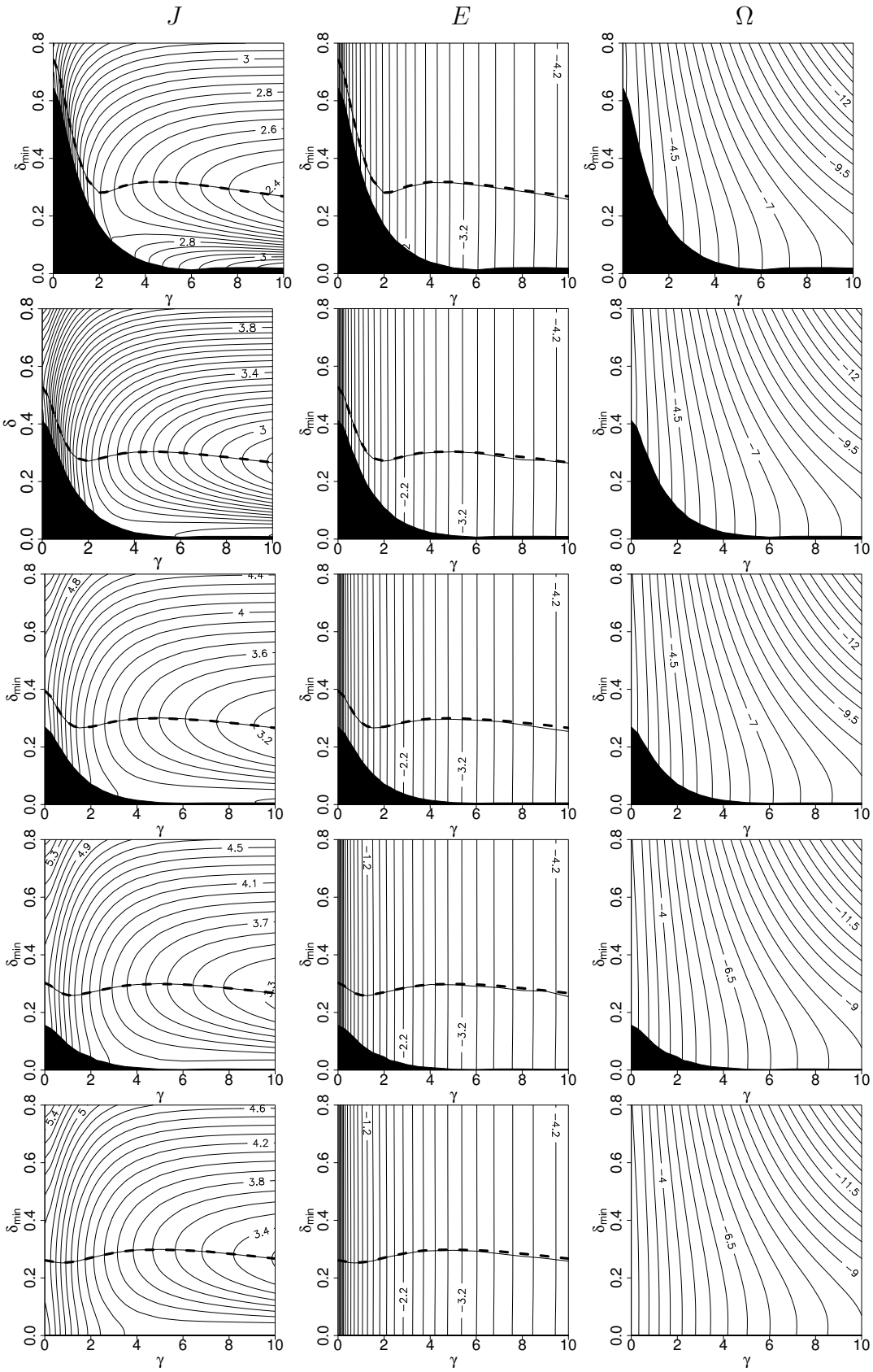

Figure 3.3: Various properties of the equilibria in the $\gamma - \delta_{min}$ parameter plane plane for five different area ratios $\alpha = 0.2, 0.4, 0.6, 0.8$, and 1.0 (rows 1–5, respectively): angular impulse J (column 1, contour interval 0.05 for rows 1–2 and 0.1 for rows 3–5), energy E (column 2, $\log_e$ scaling, contour interval 0.2), and rotation rate Ω (column 3, $\log_e$ scaling, contour interval 0.5). The bold dashed line corresponds to the boundary of linear stability (with instability below, see §3.3; note that this very closely coincides with the boundary of nonlinear stability, see §3.4.2) and the bold line marks the extrema of J or E with respect to δ_{min} for each γ. Here, and in figures 3.8, 3.17 and 3.19 the black area is the region for which no states have been generated.

distance for which J exhibits a minimum, and an almost identical distance at which E exhibits a maximum, marked by the bold lines in the figure. The biggest difference between the two extrema ranges between 0.009–0.012, depending on α. As shown by Luzzatto-Fegiz and Williamson (2012), the location of the extrema of J and E must be the same, and we expect it to coincide with the location of the boundary of stability (see discussion below). In this chapter, the difference in δ_{min} at which the extrema occur is due to the fact that the function of $E(\delta_{min})$ is very flat (cf. column 2 of figure 3.3), implying that it is very sensitive to finding the exact location of the maximum. On the other hand, the location of the minimum of J is better defined, and thus provides a more trustworthy value for the boundary of stability (cf. figure 3.4). Figure 3.4 shows how J changes with α for $\gamma = 0.02$, 0.5, 1, 2, 4 and 10. It can be seen that as γ increases, the location of the minimum of J (indicated by a dashed line in the figure) becomes independent of α, and the minimum itself becomes more obvious. It appears that the numerical method fails to converge at the point when J starts levelling off after its minimum for small δ_{min}. This is not only more pronounced for larger γ, but as γ increases also occurs at smaller distances for small α. The angular impulse increases with α, most strongly for small γ. However, the degree of asymmetry (given by α) does not affect J linearly; in fact, regardless of γ, states with $\alpha = 0.8$ and 1.0 have very similar values of J, while there is a considerable discrepancy between the values of J for $\alpha = 0.2 - 0.6$.

Saffman and Szeto (1980) and Saffman (1992), whose results are valid for both $\gamma = 0$ and $\gamma \neq 0$, argued that when the plot of $E(J)$ has the form of two branches of solutions joined at a cusp (i.e. when there exist simultaneous extrema of J and E), the lower branch is unstable whereas the upper one is linearly stable. Dritschel (1985) showed that this argument is not complete, and Dritschel (1995) demonstrated that the joint extremum of J and E coincides with the boundary of stability only for like-signed pairs of barotropic, i.e. $\gamma = 0$, vortices of equal

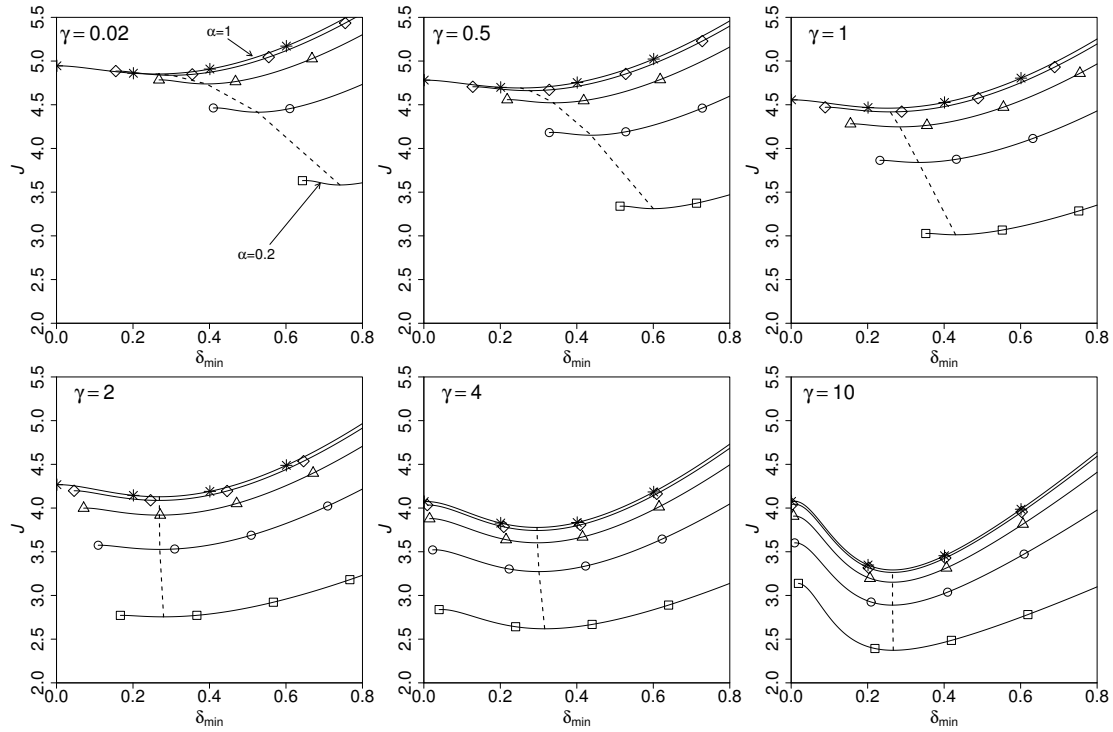

Figure 3.4: The angular impulse J against distance for various γ. The dashed line connects the minima of J, and the symbols on each line represent different area ratios: $\square$ $\alpha = 0.2$; $\circ$ $\alpha = 0.4$; $\triangle$ $\alpha = 0.6$; $\diamond$ $\alpha = 0.8$; $*$ $\alpha = 1.0$.

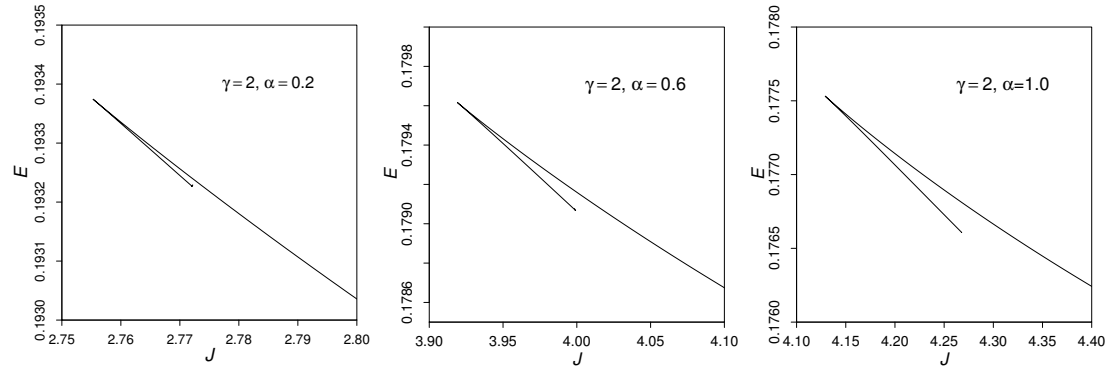

Figure 3.5: The energy E as a function of angular impulse J at $\gamma = 2$ for three different α.

or unequal size. Figure 3.5 shows a plot of E as a function of J for the $\gamma = 2$, $\alpha = 0.2$, 0.6, 1.0 families of equilibria (all other families are qualitatively similar, with the length of the lower branch increasing with γ). We see that the plots have the form described above. The linear stability analysis below confirms the coincidence of the boundary of linear stability with extrema of J and E also when $\gamma \neq 0$ (see §3.3, and the bold dashed line in figure 3.3). The nonlinear stability analysis (see §3.4) also finds the boundary of nonlinear stability to fall at this location.

Figure 3.6 shows how the particle rotation rates $\Omega_{p,i} = 2\pi/T_i$, where $T_i = \oint_{\mathcal{C}_i} ds/|\boldsymbol{u}|$ and s is arc length, change with γ and α for each of the vortices. We examine the same families of equilibria as those shown in figure 3.4, namely the cases with $\gamma = 0.02$, 0.5, 1, 2, 4 and 10. We see that both $\Omega_{p,1}$ and $\Omega_{p,2}$ decrease strongly as γ increases, and to a lesser extent as δ_{min} decreases. The sharp decrease of $\Omega_{p,2}$ for small δ_{min} at small γ suggests that the decrease in Ω_p with δ_{min} results from the presence of a stagnation point near the corner. At smaller γ, $\Omega_{p,1}$ of the larger vortex (solid line in figure 3.6) is bigger than $\Omega_{p,2}$ of the smaller vortex (dashed line in the figure), with this being most pronounced at small distances. As γ increases, so does $\Omega_{p,2}$ relative to $\Omega_{p,1}$, and it goes through a transition where $\Omega_{p,2} > \Omega_{p,1}$ at large distances and $\Omega_{p,2} < \Omega_{p,1}$ at small ones,

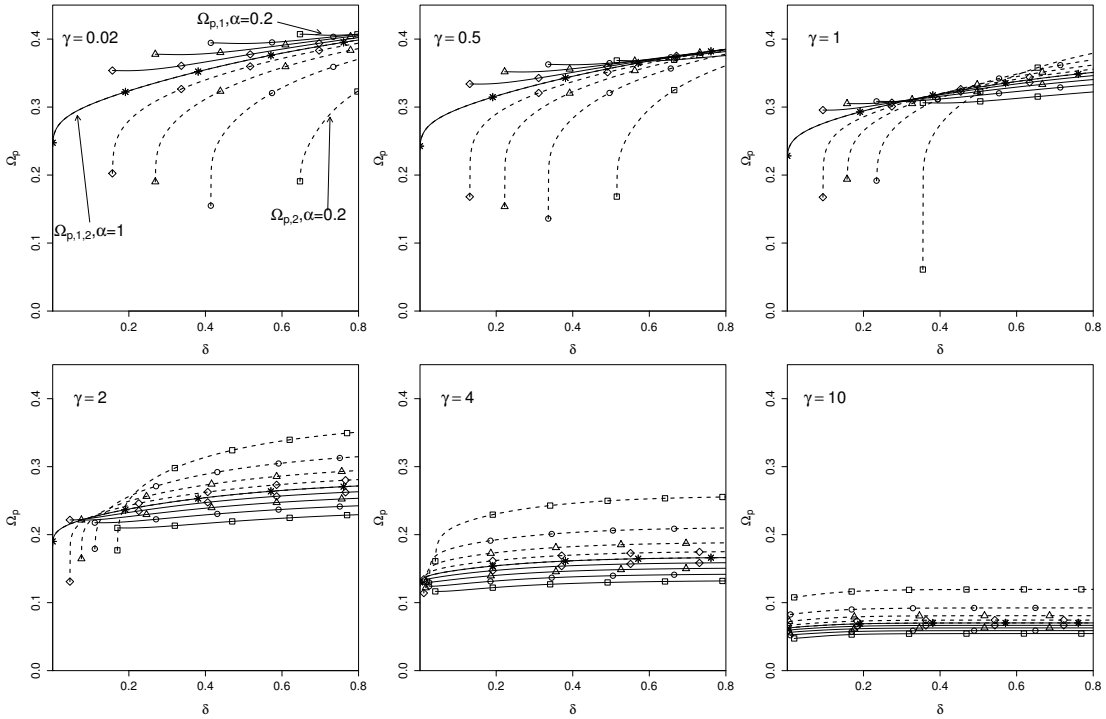

Figure 3.6: The particle frequency Ω_p against distance for various γ. The solid and dashed lines are Ω_p for the larger and smaller vortices, respectively. The symbols on each line represent different area ratios: $\square$ $\alpha = 0.2$; $\circ$ $\alpha = 0.4$; $\triangle$ $\alpha = 0.6$; $\diamond$ $\alpha = 0.8$; $*$ $\alpha = 1.0$.

until at large γ, we find $\Omega_{p,2} > \Omega_{p,1}$ for all distances. For large γ, $\Omega_{p,1}$ and $\Omega_{p,2}$ become distance-independent, as discussed below.

By comparing column 3 of figure 3.3 with figure 3.6, we see that like the particle rotation rates, the rotation rate Ω also decreases strongly with γ, and to a lesser extent with δ_{min}. We further note that for large γ, we have $\Omega_p \gg \Omega$. Here, the fluid velocity induced by each of the vortices is confined to a belt of $O(L_D)$ width, where the leading-order velocity on each contour is $\sim q_0 L_D/2$ (Nycander et al., 1993). This in turn implies that $\Omega_{p,i} \sim q_0 L_D/2P_i$, where P_i is the arc length of vortex i. This relationship holds within 10% for both vortices across all α at $\gamma = 10$. In general, the relationship is more accurate for the larger vortex at small α, and for the smaller vortex at large α. The equilibrium rotation rate Ω, on the other hand, is much smaller in magnitude because it arises from

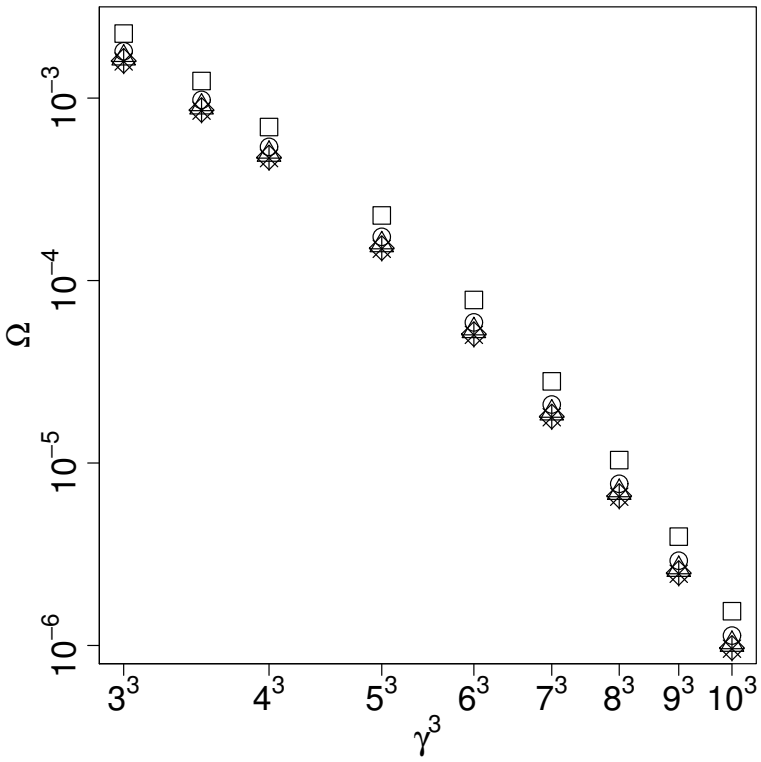

Figure 3.7: The relationship between Ω and γ^3 at $\delta_{min} = 0.700$. The different symbols correspond to: $\square$ $\alpha = 0.2$; $\circ$ $\alpha = 0.4$; $\triangle$ $\alpha = 0.6$; $\diamond$ $\alpha = 0.8$; $*$ $\alpha = 1.0$.

weak long-range interactions associated with the Green function. If following Nycander et al. (1993) we view the deformations of each contour as long waves, then it follows that they must rotate at a frequency proportional to γ^3. For the equilibrium to be steady, therefore, the frame of reference must also rotate at this rate: $\Omega \approx a\gamma^3$. Figure 3.7 verifies that this scaling holds closely for $\delta_{min} = 0.700$, with a varying only slightly from 0.0757 (at large α) to 0.0774 (at small α).

Note that our results for the symmetric case $\alpha = 1.0$ agree with those found by Polvani et al. (1989).

3.3 Linear stability analysis

We next perform a linear stability analysis of the families of equilibria described above by using the method described in §2.3.1. Here, we have two contours and so $n = 2$. We solve the arising $2nM \times 2nM$ matrix eigenvalue problem (with $M = 50$) at each δ_{min} for fixed γ and α. We have verified that doubling the number of retained wavenumbers to $M = 100$ insignificantly affects our results.

The growth rates σ_r of the most unstable mode, being the real part of the solution σ of the eigenvalue problem, are presented in figure 3.8 in the $\gamma - \delta_{min}$ parameter plane for each α. The "waviness" of the contours arises from a competition between a variety of different modes of instability; however, we are still able to distinguish a small-γ and a large-γ regime. At small γ, the contours of σ_r are steep and growth rates rapidly decrease with γ. This is most apparent in the smaller α cases, with the boundary between the steep and flat contours being at $\gamma \approx 2$. As α increases, not only does this boundary fall at smaller γ, but also states with progressively smaller δ_{min} become stable across all γ. Note that as in §3.2.2, we do not show the $\gamma = 0$ case, and instead use equilibria having $\gamma = 0.02$; nevertheless our results converge to the barotropic results (Dritschel, 1995). Note that Dritschel (1985) examined various modes of instability of symmetric barotropic vortices and found that there are many possible mode combinations, and that there is a tendency for vortices to merge. The eigenstructure pushes two vortices together (at some angle), causing them to deform and eventually overlap (merge).

Near the margin of stability, the growth rates turn out to be sensitive to the number of points n_p chosen to discretise half of the boundary of each vortex. Figure 3.9 shows σ_r for $n_p = 200$ (the value used in this chapter), 400, and 800. We see that as γ increases, the results become less sensitive to the number of points. The fact that the extrema of energy E and angular impulse J, marked by

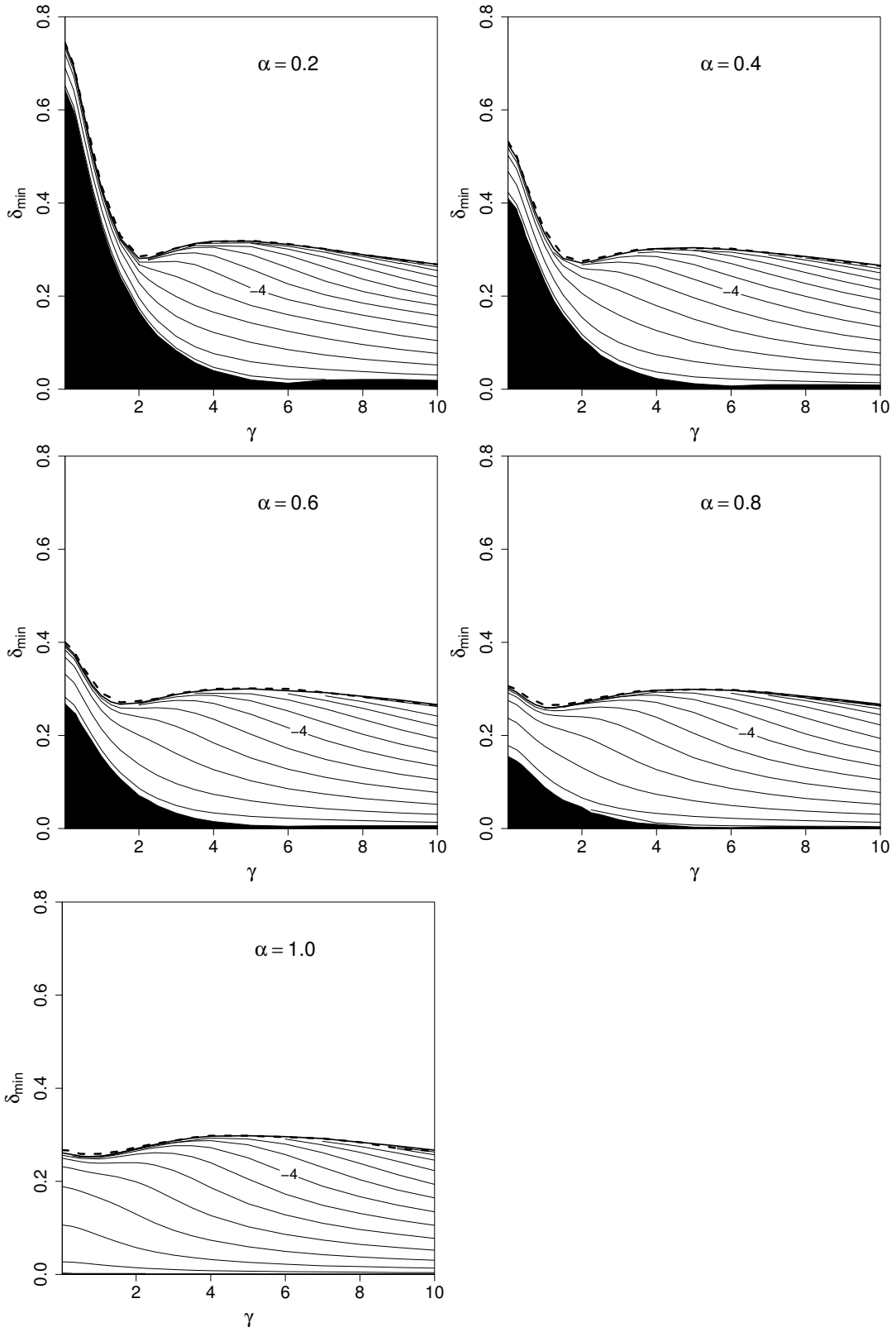

Figure 3.8: Logarithmically ($\log_e$) scaled growth rates σ_r of the most unstable mode in the $\gamma - \delta_{min}$ parameter plane. The contour interval is 0.5. The bold line corresponds to when $\sigma_r = 0$, while the dashed line corresponds to the boundary of nonlinear stability. Note that these two lines practically coincide.

the vertical lines in the figure, do not converge may be attributed to how "flat" the function of $E(\delta_{min})$ is (see discussion in the previous section).

Dritschel (1995) found that for the $\gamma = 0$ case, instability erupts via an "exchange of stability", where the real and imaginary parts of σ are both identically zero at the margin of stability $\delta_{min} = \delta_c$. Moreover this corresponds to simultaneous extrema of J and E. We recover this result for our $\gamma \neq 0$ equilibria, pointing towards the possible existence of additional branches of families of equilibria (which are likely to be unstable, as we have found no evidence for them in our nonlinear simulations). As can be seen from figure 3.9, we do not have $\sigma_r = \sigma_i = 0$ exactly at $\delta_{min} = \delta_c$, but the falling values of the lower branch of σ_i as n_p increases indicates that this result is likely to be recovered for infinite resolution.

To summarise, doubly-connected equilibria having large γ tend to be stable at smaller distances than those having small γ. This is most notable at small α. Additionally, the boundary of stability becomes independent of α for large γ, especially for $\gamma \gtrsim 2$ and $\alpha > 0.2$. Note that Makarov et al. (2012) found that two-vortex heton equilibria (a heton is a vortex structure where the vortices are located in different layers) are less stable at large γ. However, these differences in the effects of γ can be attributed to the fact that the dynamics of a two-layer quasi-geostrophic system are very different when the lower layer is of finite depth (it is infinite in QGSW), as pointed out and discussed by Polvani et al. (1989).

3.4 Nonlinear evolution

We next examine the nonlinear stability of the equilibria, and by finding their margin of nonlinear stability, we aim to relate it to that of the linear problem. We also endeavour to give an overview of the general features which characterise the evolution of marginally unstable states, and how these change with γ and

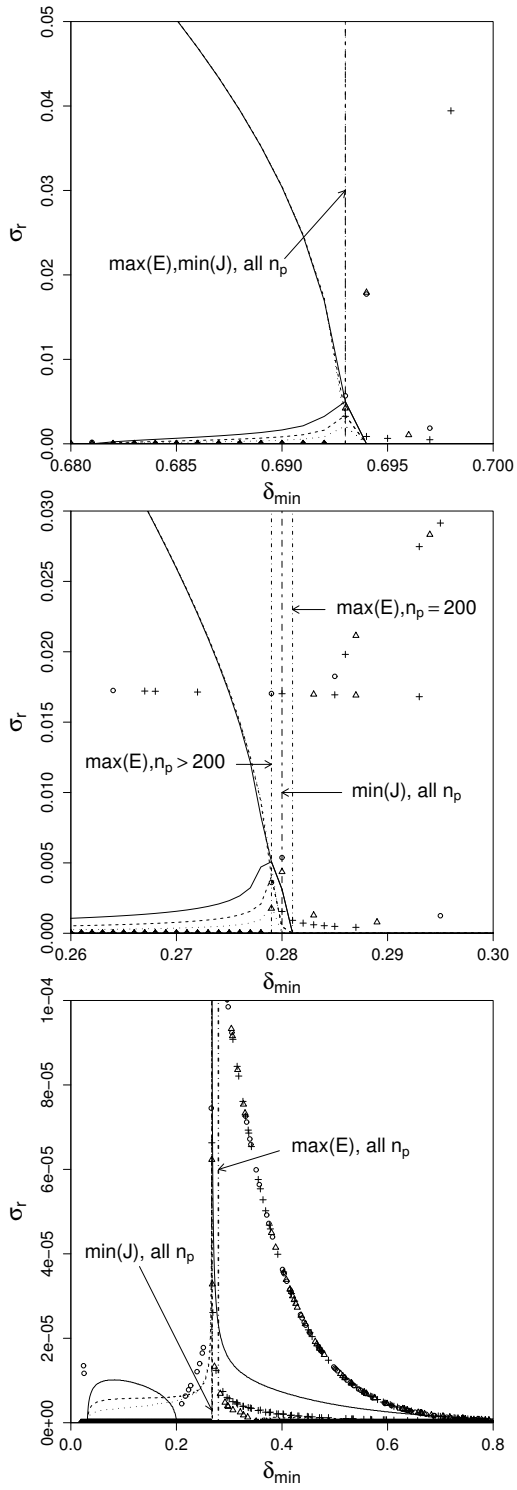

Figure 3.9: The growth rates (lines) and frequencies (points) of the two most unstable modes as a function of distance for $\gamma = 0.25$ (top), $\gamma = 2$ (middle), and $\gamma = 10$ (bottom) at $\alpha = 0.2$. The different lines and symbols indicate different number of points n_p used on half of the vortex boundary. We have: $n_p = 200$ (solid line; circles), $n_p = 400$ (dashed line; triangles), and $n_p = 800$ (dotted line; pluses). The dash-dotted line indicates the maximum of E and the short-long-dashed line the minimum of J for each of the cases, as marked in the figure. Note the different scale for σ_r in each of the figures.

α. We first present the numerical framework for examining the evolution of the states in §3.4.1 and then present our results in §3.4.2.

3.4.1 Method

We examine the nonlinear evolution of equilibria by exploiting the natural "contour dynamics" formalism, as discussed in §3.2.1. As we only need to keep track of the boundaries of the vortex-patch equilibria, we discretise the boundary of each vortex by a self-adapting number of nodes connected by local cubic splines, and numerically solve equation 3.1 using the "contour surgery" algorithm (Dritschel, 1988, 1989). The algorithm, also used in chapter 2, splits the singular modified Bessel function K_0 appearing in equation 3.1 into a logarithmic part, $\log|\boldsymbol{x}-\boldsymbol{x_k}|$, which is integrated explicitly, and a non-singular remainder part, which is numerically integrated by two-point Gaussian quadrature. A fourth-order Runge-Kutta time integration method is used with a fixed, standard time step of $\Delta t = 0.025$.

The number of nodes adjusts in response to dynamic changes in the contour curvature. We initially start with a slightly disturbed doubly-connected equilibrium, where each vortex patch is represented by an initial $n = n_0 = 400$ number of nodes. In order to avoid biasing the evolution towards any particular instability mode, we randomly perturb the x and y coordinates of each node by up to 1% of $\Delta\theta = 2\pi/n_i$, where $n_{i=1,2} = n_0$ is the initial number of nodes used to represent each contour. Throughout the evolution, the nodes are redistributed every 8 time steps, using a dimensionless node separation parameter $\mu = 0.2$ and a large-scale length $L_c = P/(\mu n_0)$, where $P = P_1 + P_2$ is the sum of the arc lengths of the equilibrium contours. Contour surgery, which either splits a contour into two parts or joins two contours together, is performed with the same frequency whenever the distance between two contours or two parts of the same contour decreases

below the "cut-off" scale $d_c = \mu^2 L_c/4$. This allows the representation of many complex phenomena which typify vortex-patch dynamics, such as filamentation and splitting. The numerical details of the procedure, along with a full discussion of the now standard settings of the control parameters μ, d_c and the frequency of the surgery and node redistribution can be found in Fontane and Dritschel (2009), which also generalise to the pure contour dynamics simulations of this study..

We consider five different area ratios $\alpha = 0.2 - 1.0$ at $\Delta\alpha = 0.2$, as well as $\gamma = 0.02$, 0.25, $\gamma = 0.5 - 3.5$ at $\Delta\gamma = 0.5$, and $\gamma = 4 - 10$ at $\Delta\gamma = 1$ (16 γ cases in total). The small-γ states are examined more closely as in this regime there is a steep decrease in the growth rates, as seen in figure 3.8. We evolve the equilibria for at least 200 particle rotation periods $T_p = 2\pi/\min\Omega_{p,1}, \Omega_{p,2}$ of the smaller vortex. One T_p is equivalent to the amount of time it takes for a particle to complete a circuit of the vortex boundary. Based on the time scales which typify the oceans, this was deemed sufficiently long to assess nonlinear stability.

3.4.2 Results

In general, unlike the reverse of the statement, linear stability does not imply nonlinear stability. However, we find that the boundaries of linear and nonlinear stability coincide to within $\Delta\delta_{min} = 0.008$, as shown by the dashed and bold lines in figure 3.8. The accuracy of this coincidence increases with γ. We expect that with increasing resolution, these discrepancies would reduce to zero.

The unstable evolution of vortices having $\delta_{min} < \delta_c$ near the margin of stability reveals a surprisingly rich set of behaviours. We follow Dritschel and Waugh (1992), and classify them based on the change in the area of the two largest PV patches in the domain: $A_1^r = A_1^f/A_1^i$ and $A_2^r = A_2^f/A_2^i$, where the superscripts i and f indicate the initial and final states (the A_j^f are calculated as a time-

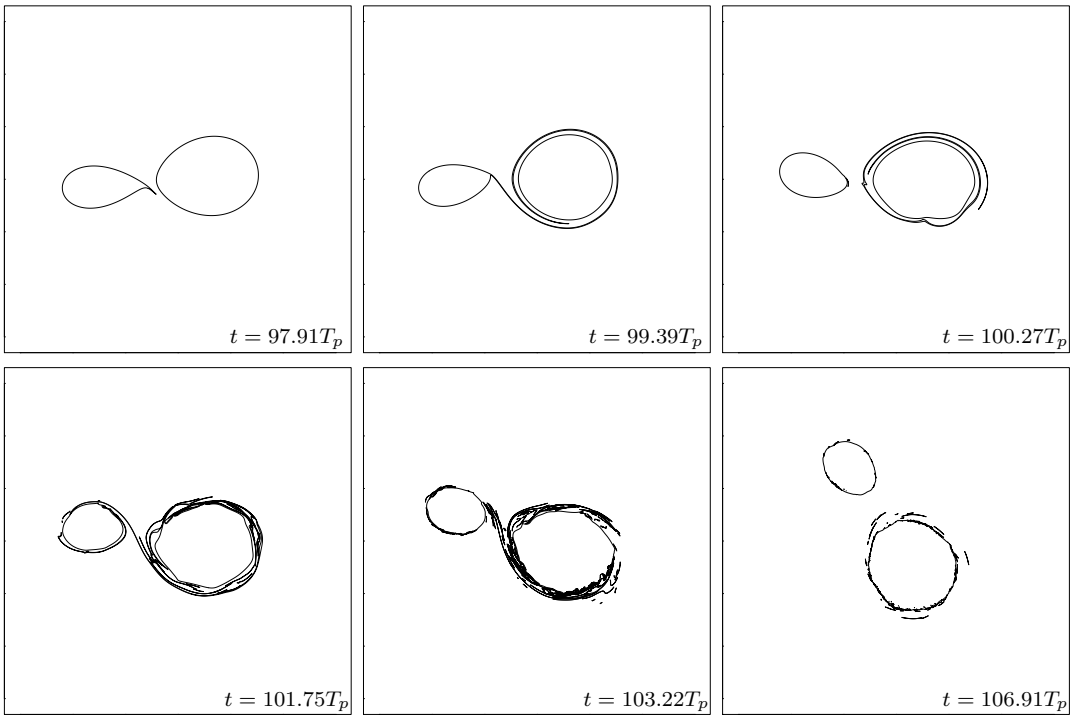

Figure 3.10: An example of the evolution of a state undergoing partial straining out $\mathrm{PSO_b}$. We show the case $\gamma = 1$, $\alpha = 0.4$, and $\delta_{min} = 0.339$. The plotted domain has $|x|, |y| \leq 3.3$. See also supplementary movie 2.

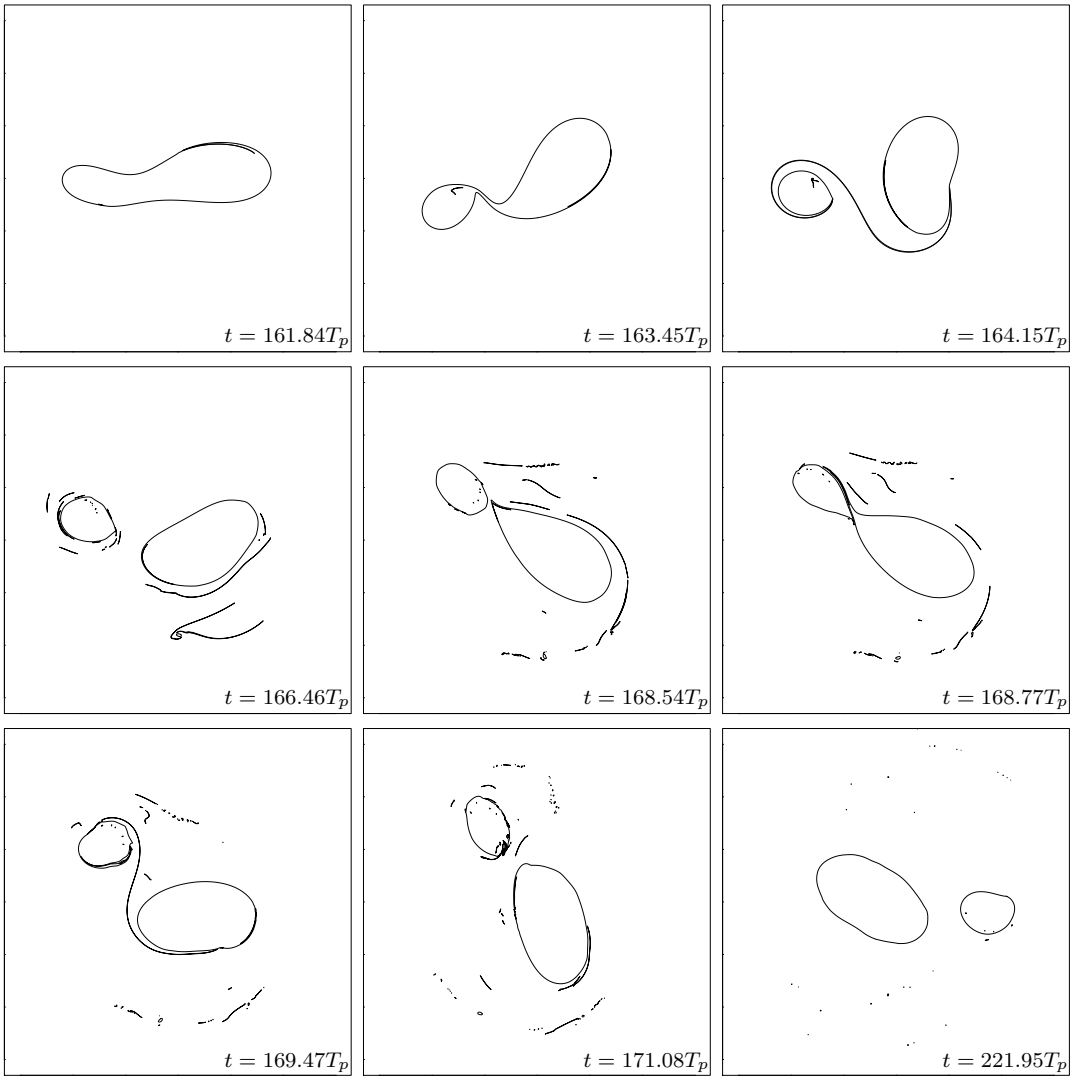

Figure 3.11: An example of the evolution of a state undergoing partial merger PM. We show the case $\gamma = 2$, $\alpha = 0.6$, and $\delta_{min} = 0.270$. Here, $|x|, |y| \leq 3.3$. See also supplementary movie 3.

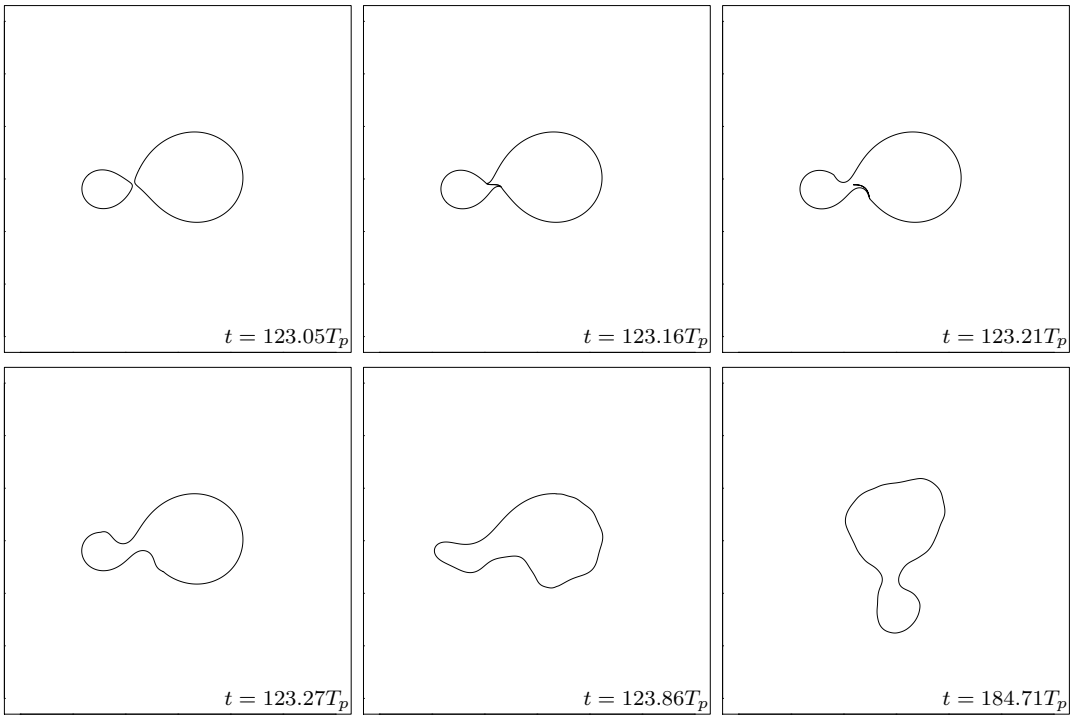

Figure 3.12: An example of the evolution of a state having large γ which undergoes complete merger CM. We show the case $\gamma = 10$, $\alpha = 0.2$, and $\delta_{min} = 0.268$. Here, $|x|, |y| \leq 3.3$. See also supplementary movie 4.

average once an instability has taken place). Four regimes have been identified, two of which are further divided into two categories. The first is the elastic interactions regime, in which the states do not change in area, i.e. $A_1^r = A_2^r = 1$. Based on a visual examination of the evolution of the states, this regime may be further subdivided into stable states ($\mathrm{EI_s}$), which do not change in shape, and vacillating states ($\mathrm{EI_v}$). The vacillating states undergo a cycle of approaching and moving away from each other, adjusting their shapes as the distance between them changes, but not changing in area. The second regime is partial straining out (PSO), where the areas of either one $A_1^r = 1$, $0 < A_2^r < 1$ ($\mathrm{PSO_o}$) or both $0 < A_1^r < 1$, $0 < A_2^r < 1$ ($\mathrm{PSO_b}$) of the vortices decreases. The third and fourth regimes are those where the larger vortex grows in size, by either partially destroying the smaller one $A_1^r > 1$, $0 < A_2^r < 1$ in partial merger (PM) or wholly absorbing it in complete merger $A_1^r > 1$, $A_2^r = 0$ (CM).

Figure 3.10 shows an example of the PSO_b regime, with $\gamma = 1$, $\alpha = 0.4$, and $\delta_{min} = 0.339$. (Note that figures 3.10–3.13 are complemented by supplementary movies 2–5). The smaller vortex (V_2) undergoes a wave-3 disturbance and sheds a filament which wraps around the larger vortex (V_1). Fine-scale structures develop on the boundary of V_1, which then get partly transferred also onto the boundary of V_2. Figure 3.14 shows how the area of V_1 (bold line), V_2 (thin line), and their sum (dashed line) changes with time. We see that soon after the onset of instability both of the vortices reach constant areas which do not change, even though some small-scale structures still exist on their boundaries (this is shown in the last panel of figure 3.10). In the case shown in figure 3.10, the small-scale filamentary debris become so small that they eventually get dissipated away, and we are left with two asymmetric vortices. However, the filaments may also roll up to form small satellite vortices (much smaller than the two dominant vortices). Additionally, the filament shed by V_2 is not always transferred back onto the boundary of V_2. The PSO_o regime is qualitatively similar to PSO_b, but V_1 does not increase in area. However, as can be seen from the plots in figure 3.14 corresponding to the PSO_o and PSO_b regimes, the decrease in area of V_1 is not large. In fact, at most it decreases by 2.5%. We say a state falls into the PSO_b regime if the area of V_1 changes by more than 1%, and so the division between the PSO_o and PSO_b regimes is arbitrary. However, the visual examination of the equilibria shows that there is significantly more interaction of the filament shed by the smaller vortex with the boundary of the larger vortex in the PSO_b regime.

Figure 3.11 shows an example of the partial merger regime, with $\gamma = 2$, $\alpha = 0.6$, and $\delta_{min} = 0.270$. The vortices merge, but after only about $3T_p$ the resulting vortex splits, shedding some filamentary debris. After another $5T_p$ it reconnects for $2T_p$ before splitting again and shedding more debris. As can be seen from the PM plot (top right) of figure 3.14, the size of V_1 does not change after the second split, unlike that of V_2, which sheds a few small filaments, until it too

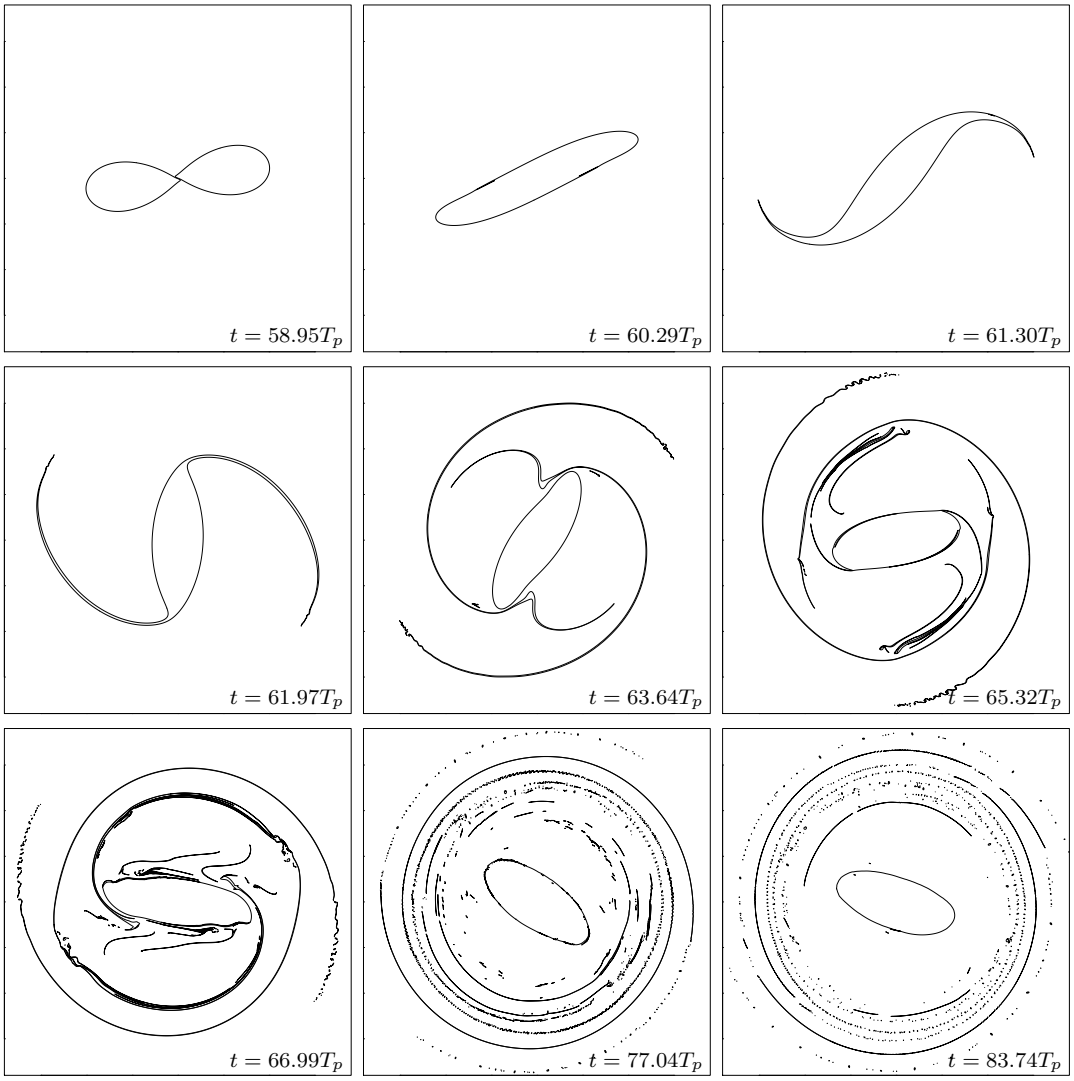

Figure 3.13: An example of the evolution of a state having small γ which undergoes complete merger CM. We show the case $\gamma = 0.02$, $\alpha = 1.0$, and $\delta_{min} = 0.266$. Here, $|x|, |y| \leq 3.8$. See also supplementary movie 5.

reaches a size which does not change (shown at $t = 221.95T_p$ in figure 3.11). The final area ratio between the two vortices gets halved to $\alpha^f \approx 0.27$, and despite the shedding of filaments during the splitting process, only about 2.4% of the total area of the two vortices is lost. This series of merging and splitting events, sometimes occurring multiple times, is typical of the PM regime. The amount of area lost to filaments varies with γ, and is maximum at 26.4% for $\gamma = 0.25$, $\alpha = 1.0$, and $\delta_{min} = 0.266$, where there is considerable filamentation and interaction of the filaments with the boundaries of both V_1 and V_2. For unstable equilibria with $\gamma > 1$, no more than 5% of the total area is lost, and states having $\gamma = 4$ (the largest γ in the PM regime) have the smallest area loss of $\ll 1\%$, despite repeating the merging and splitting process up to five times before reaching a quasi-equilibrium state. For the large-γ cases, it appears that when the state merges, it attempts to reach a quasi-steady simply-connected state by shedding small filaments, but it is not able to do so and eventually splits. Note that in realistic geophysical flows, in which vortices are often subjected to a straining flow from e.g. the presence of other vortices in their proximity, the effects of "vortex stripping" (vorticity being torn away from the vortex periphery) and diffusion (if additionally viscous effects were present) would affect the evolutionary path of unstable vortices (Legras and Dritschel, 1993; Mariotti et al., 1994). This might be expected to affect both the PSO and PM regimes of instability, as the strain would prevent filaments from rolling up to form smaller vortices.

When merger occurs at large γ, large-amplitude waves obeying the modified Korteweg-de Vries equation to leading order in L_D (see Nycander et al., 1993) propagate on the vortex boundary, and are responsible for the splitting of the vortex. As γ increases the splitting no longer takes place, or, as in the cases of $\gamma \lesssim 5$ having $\alpha \geq 0.8$ and $4 \lesssim \gamma \lesssim 6$ having $\alpha \lesssim 0.4$, a near-instantaneous split lasting much less than one T_p occurs and the vortices immediately reconnect. In figure 3.12 we see an example of a case having $\gamma = 10$, $\alpha = 0.2$, and

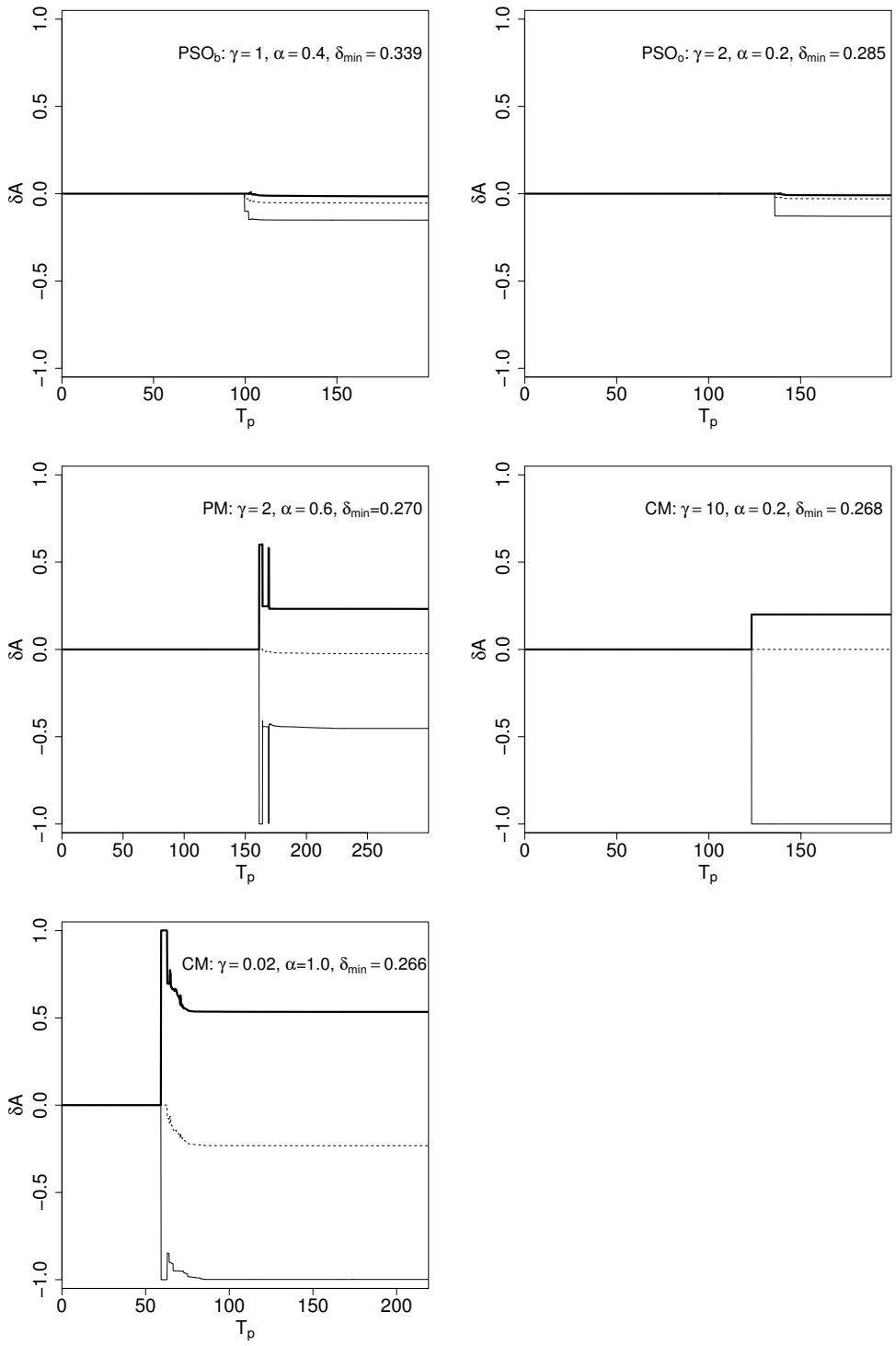

Figure 3.14: The fractional change in area $\delta A = A/A^i - 1$ of the vortex with largest area (bold line), second largest area (thin line), and in the total area of the two largest patches of vorticity (dotted line). We see the cases corresponding to figures 3.10–3.13, i.e. $\gamma = 1$, $\alpha = 0.4$, $\delta_{min} = 0.339$ for $\mathrm{PSO_b}$ (top left); $\gamma = 2$, $\alpha = 0.2$, $\delta_{min} = 0.285$ for $\mathrm{PSO_o}$ (top right); $\gamma = 2$, $\alpha = 0.6$, $\delta_{min} = 0.270$ for PM (middle left); and $\gamma = 10$, $\alpha = 0.2$, $\delta_{min} = 0.268$ (middle right) and $\gamma = 0.02$, $\alpha = 1.0$, $\delta_{min} = 0.266$ (bottom left) for CM.

$\delta_{min} = 0.268$ which undergoes complete merger. The waves propagating slowly along the merged boundary are obvious immediately after merger. Note that although the merged state is only quasi-steady, it nevertheless periodically repeats regular shapes, as shown at times $t = 123.27T_p$ and $t = 184.71T_p$ in figure 3.12. The asymmetry of the recurring dumbbell-shape is dependent on the initial α of the doubly-connected state – as α grows, the dumbbell becomes increasingly symmetric. As can be seen from the dashed line in figure 3.14 (bottom left), essentially no area is lost to filamentation during or after merger. Apart from special cases having $\gamma = 0.02$ and $\alpha = 1.0$ (see below), the CM regime occurs only for large-γ states having $\gamma \geq 2$. In this regime, states having small $\alpha \leq 0.4$ and $\gamma \leq 4$ produce the most filamentation, losing 2.7% of the total area. The behaviour of these states is similar to those in the PM regime, where merged simply-connected states shed PV while trying to recover a quasi-steady state. In the CM regime, such a quasi-steady state is reached quickly, and no further splitting occurs. States having large α, and larger γ shed essentially no PV during or after merger.

As mentioned above, cases having $\gamma = 0.02$ and $\alpha = 1.0$ exhibit atypical behaviour for the small-γ regime, as shown for $\delta_{min} = 0.266$ in figure 3.13. The state merges, and then by a wave-4 disturbance sheds filaments from both tips (in general, such a state loses about 23% of its total area, see figure 3.14). These filaments then interact with the vortex boundary in a very complex way, until a quasi-steady elliptical vortex surrounded by a sea of filamentary debris is formed. These filaments tend not to roll up into small vortices, unlike what is sometimes seen in the PSO_o and PSO_b regimes for sufficiently thick filaments (for an explanation of this behaviour, see Waugh and Dritschel, 1991). This type of evolution has been previously described in the barotropic case by Dritschel (1995), who showed that even slight departures from the initially symmetric state, e.g. $\alpha = 0.99$, causes the vortex to instead exhibit a wave-3 instability after merger.

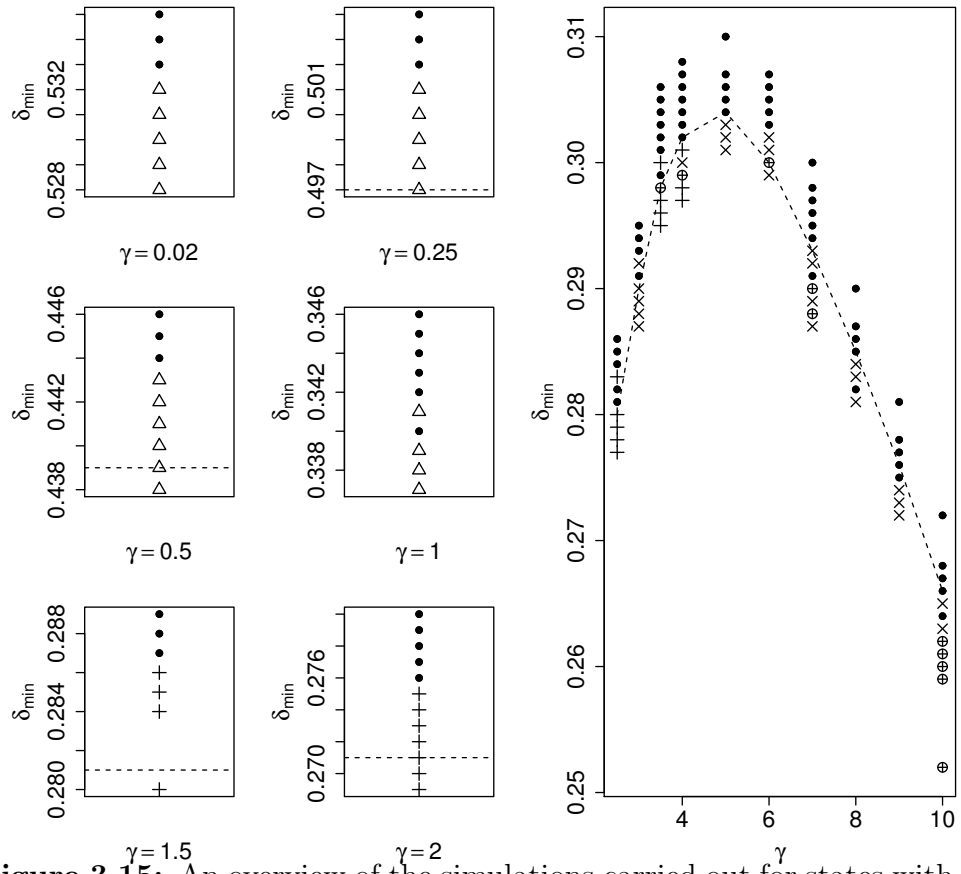

Figure 3.15: An overview of the simulations carried out for states with $\alpha = 0.4$. The symbols denote the following: "•" stable state; "⊕" vacillations; "△" $\mathrm{PSO_b}$; "+" PM; and "×" CM. The dashed line shows the margin of linear stability (note that if it is not present, the margin lies outside the plotted region).

We obtain similar results for $\gamma = 0.02$. However, for vortices with $\gamma \gtrsim 0.5$ we find that such a small departure from symmetry does not affect the nature of the nonlinear evolution. Note that we do not find complete merger for any other cases with $0.02 < \gamma < 2$.

An overview of the simulations carried out for states with $\alpha = 0.4$ is shown in figure 3.15. As can be seen from the figure (the other α examined produce similarly complex results), there may be a variety of different behaviours occurring at a fixed γ (and α) near λ_c. As an example, at $\gamma = 4$ near the margin of stability we see instabilities having the form of vacillations and partial and complete merger. For $\gamma \gtrsim 3$ we see that there is a continuous transition from vacillating to unstable states. As in the previous chapter, we attribute this behaviour to the sensitivity (now on δ_{min}) of the phases of the large-amplitude waves travelling on the boundary of the vortices. Despite the complexity of different types of behaviours occurring, below we attempt to divide up the parameter space considered based on the type of instability it experience, also tying this in with the results of the linear stability analysis. For $\alpha = 0.2 - 0.6$ at small $\gamma \lesssim 0.5 - 2$ there are only PSO evolutions (the lower γ values correspond to higher α). The location of this boundary roughly corresponds to the boundary between the steep and flat contours in figure 3.8. The PSO regime is absent for $\alpha \geq 0.8$, where instead the small $\gamma \lesssim 2$ states fall into the PM regime. For $\alpha = 0.2 - 0.6$ the PM regime falls between $1 \lesssim \gamma \lesssim 4$ (again, the lower γ corresponds to higher α). The PM regime corresponds to the region of the σ_r diagrams where there is a transition from the small-γ to large-γ instability modes. Although larger-α states do not have a region of steep σ_r contours nor the PSO regimes of evolution, the transition region is still present, only for smaller γ than in the lower-α states. The region of flat σ_r contours at large γ corresponds to the CM regime for all α. Note that both at the boundary of the PM and CM regimes, and in the CM regime itself, we also have vacillations (see supplementary movie 6 for an example of this).

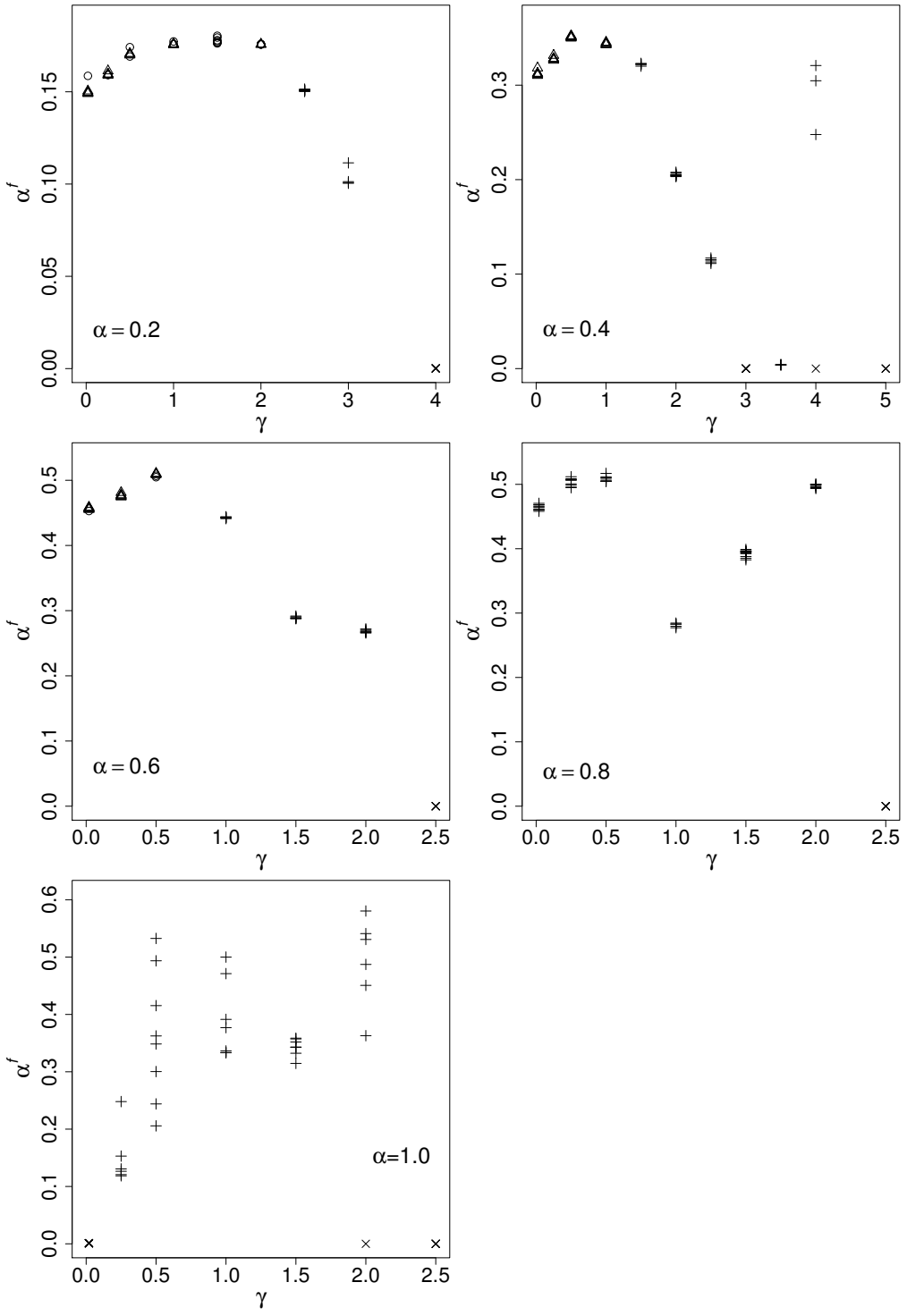

Figure 3.16: α^f as a function of γ for the unstable cases having different initial area ratios. The symbols denote the following: "○" PSO_o; "△" PSO_b; "+" PM; and "×" CM. Note that γ greater than the ones shown in each of the figures have only instabilities in the CM regime.

Lastly, we find that the final vortex area ratio α^f is *always* less than the initial one α^i (henceforth we omit the superscript i for ease of notation). This is shown in figure 3.16, which shows α^f for each δ_{min} considered and for the five different α examined. The area of V_2 never increases, but that of V_1 may for all α. For low $\alpha \lesssim 0.6$ the highest α^f are obtained in the PSO regime; on the other hand for $\alpha \gtrsim 0.6$, this regime of evolution is absent. Note that for the barotropic case, Dritschel (1995) has also found that V_2 never increased its size, and that V_1 did, but only for $\alpha \gtrsim 0.6$. Additionally, when $\gamma = 0$, $\alpha^f < 0.5$ always, which for $\gamma \neq 0$ changes to $\alpha^f < 0.6$.

3.5 Transitions between simply- and doubly-connected equilibria

In chapter 2, the stability of two-fold symmetric simply-connected (SC) vortex-patch equilibria was examined. The families of these dumbbell-shaped equilibria are fully spanned by γ and their aspect ratio λ, which is the ratio of the minor to major axes of the vortex patch. Similarly to the doubly-connected (DC) states, their limiting state consists of two vortices joined at a single point. The instability types of an SC state range from the vortex shedding a single filament — which as γ is increased may roll up to form a smaller vortex — to a split into two symmetric vortices. This means that a pair of quasi-steady co-rotating vortices with area ratio $0 < \alpha \leq 1$ is formed. Conversely, as was seen above, during instability many DC states, especially those with larger γ, often merge into a single quasi-steady vortex, with either no, or negligible filamentation. Through merging and splitting, they may also undergo a transition from one DC state to another quasi-steady DC state.

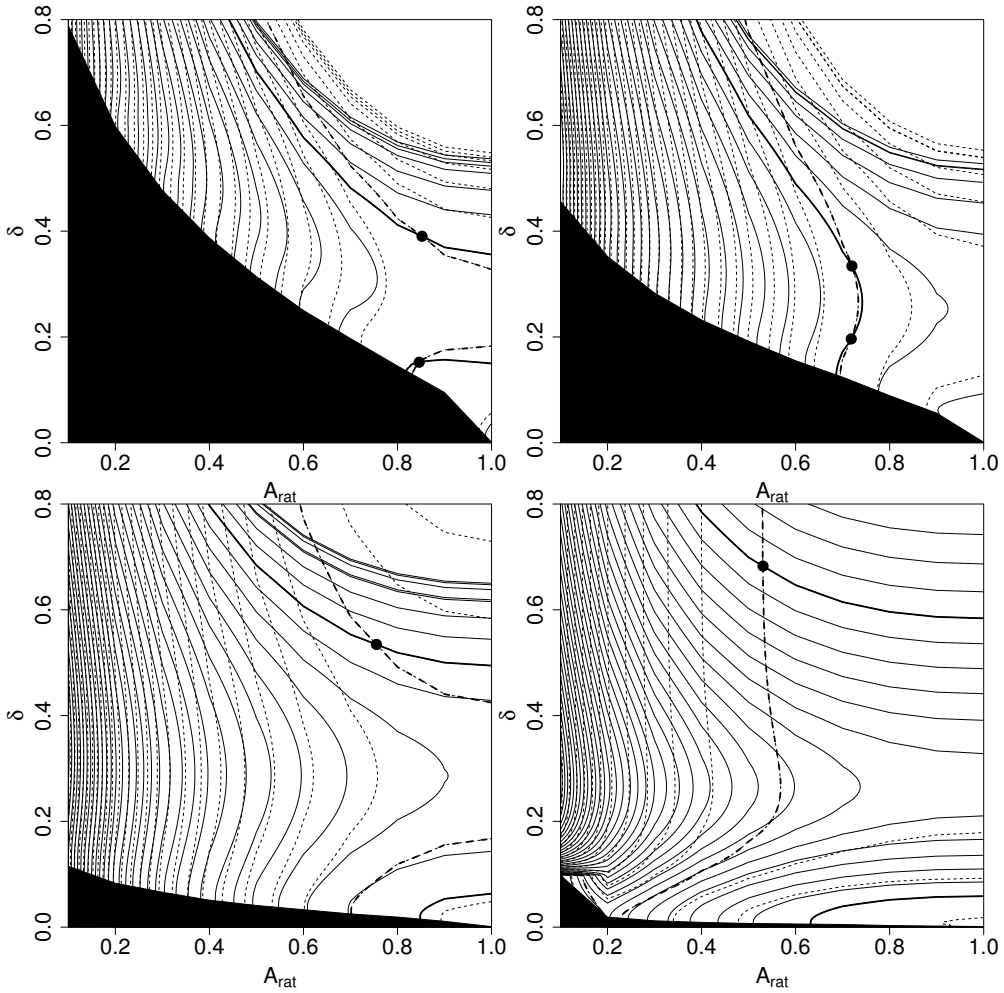

Figure 3.17: J (thin line) and E (dashed line) of DC states in the $\alpha - \delta_{min}$ parameter plane. From left to right, top to bottom, we show γ =0.25, 1, 3, and 10. The contours extracted correspond to states with $\lambda = 0 - 1$ at $\Delta\lambda = 0.010$. A transition is possible if corresponding E and J contours intersect. A complete transition into more than one unique DC state is possible, when contours intersect in more than one place. The intersection point(s) are indicated by the black dot(s), and the corresponding contours are bold.

Cerretelli and Williamson (2003a) studied families of barotropic equilibria, starting from a DC state and transitioning into an SC one. Experimental studies (Meunier and Leweke, 2001; Cerretelli and Williamson, 2003b) have shown that prior to merger, symmetric barotropic vortices may diffusively merge into a dumbbell-shaped vortex. Below we examine both the complete and dissipative transitions between DC and SC states, and between two DC states.

Dritschel (1985, 1986) examined transitions between barotropic SC and DC states having identical circulation, angular impulse, centroid location, energy, area and vorticity. Waugh (1992) performed a similar analysis for transitions between a single and two barotropic elliptical vortices. They found that such transitions are possible, even if they occur between two unstable states, and thus the resulting states are short-lived.

We say that a transition between two equilibrium states is complete if the quantities mentioned above are conserved. The statement of their conservation is equivalent to the conservation of J, E and area (for fixed γ). By finding two (or more) states with identical (J, E) at a fixed γ, we identify complete transitions between SC and DC states, and between two DC states (note that we keep the total area $A = \pi$ in all cases). We concentrate on complete transitions from an unstable to a stable state, as these are the most likely to occur and last long times, even though complete transitions between two stable and two unstable states also exist. Based on the results found here and in chapter 2, many transitions between distinct equilibrium states appear possible. Numerous instances have been found where vortices merge or split with virtually no filamentation or loss of area, especially at large γ, thus conserving total area, J and E.

We first examine the effects of non-zero γ on complete transitions between SC and DC equilibria. For a complete transition to be possible, the angular impulse and energy of an SC state must be equal to that of a DC state, i.e. $(J, E)_{\mathrm{SC}} \equiv (J, E)_{\mathrm{DC}}$. Figure 3.17 shows J (thin line) and E (dashed line) of

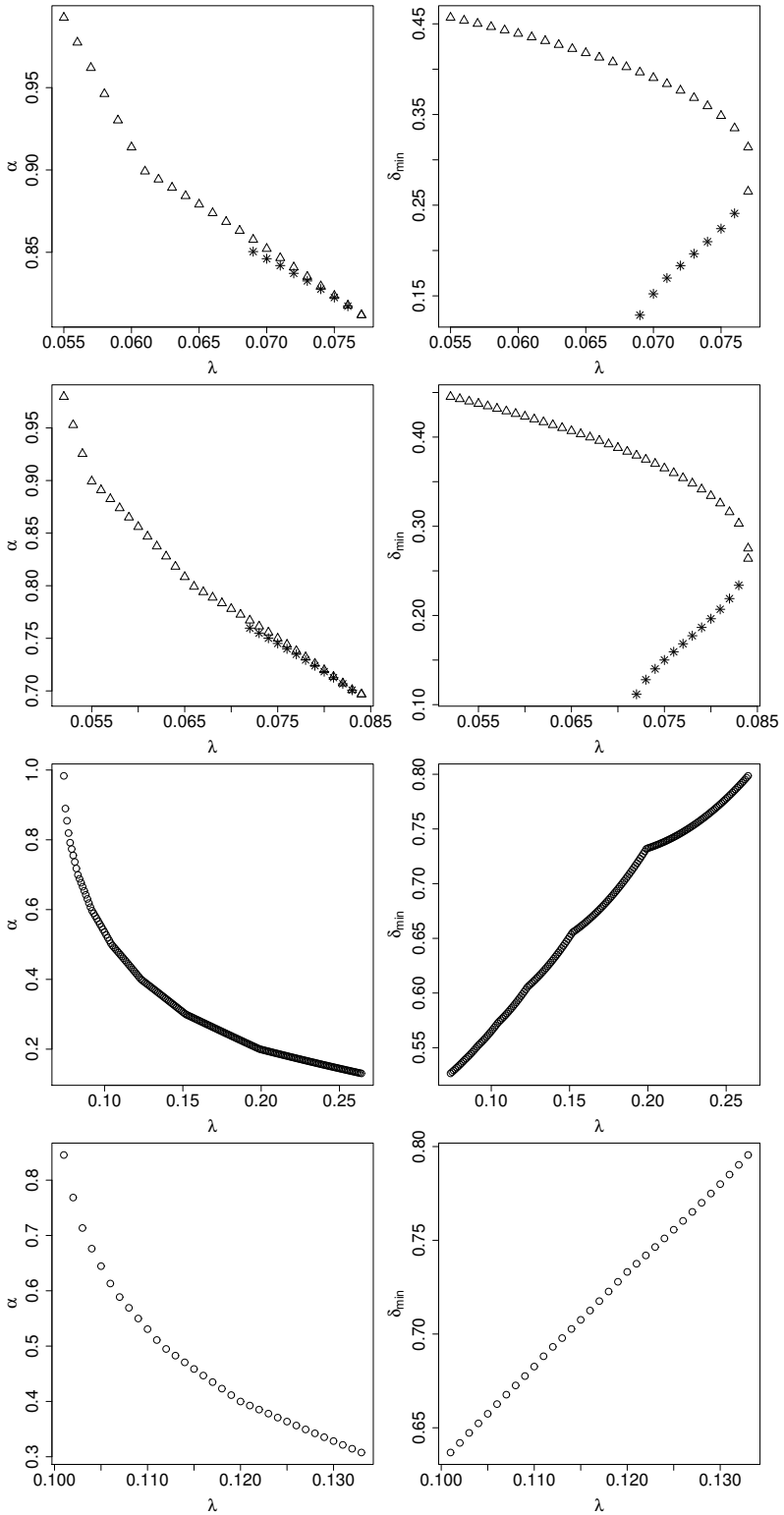

Figure 3.18: A summary of complete transitions possible between SC and DC states. In columns 1 to 4 we show γ =0.25, 1, 3, and 10. The symbols indicate the stability regimes of (SC,DC): $\circ$ (stable, stable), $\triangle$ (unstable, stable), and $*$ (unstable, unstable).

DC states in the $\alpha - \delta_{min}$ parameter plane for $\gamma = 0.25$, 1, 3 and 10. The contour levels shown correspond to $(J, E)_{\rm SC}$ at the same γ and for aspect ratios $0 < \lambda < 1$, with $\Delta\lambda = 0.010$. The intersection points of a pair of contours associated with the same λ (for illustration, marked by a black dot on one contour pair in the figure) correspond to a possible complete transition between two states. To determine a range of possible complete transitions, at a fixed γ we look at contour levels corresponding to SC states with a finer division $\Delta\lambda = 0.001$, and locate intersection points of (J, E) in the $\alpha - \delta_{min}$ parameter plane. Figure 3.18 shows a summary of these complete transitions for α (row 1) and δ_{min} (row 2) as a function of λ. We find that complete transitions are possible between a stable SC to stable DC state, an unstable SC to unstable DC state, and an unstable SC and stable DC state, as indicated by the different symbols in the figure. Note that we do not find transitions between a stable SC and an unstable DC state.

We see that for $\gamma \lesssim 1$, complete transitions are possible between a stable or unstable DC state and an unstable SC state. These complete transitions are not unique, and for SC states with larger λ, both a stable and unstable DC state with the same energetics exists. The difference in α of the two possible DC states is small, as opposed to the difference in the distance between each of the vortices in the corresponding states. In contrast, for $\gamma > 1$, we find that only complete transitions between stable SC and DC states are possible for the sampling of the parameter space examined, and that these complete transitions are unique.

We next examine complete transitions between two DC states, denoted a and b, so that $(J, E)^a_{\rm DC} \equiv (J, E)^b_{\rm DC}$. Figure 3.19 shows J and E of a DC^b state in the $\alpha - \delta_{min}$ parameter plane. The contour levels shown correspond to $(J, E)^a_{\rm DC}$ at a fixed γ and (α, δ_{min}) with α in the range 0.1–1 at $\Delta\alpha = 0.1$ and $\delta_{min} = 0.500$. Similarly as for complete transitions between SC and DC states, given $(\alpha, \delta_{min})^a$ of DC^a, we find the corresponding $(\alpha, \delta_{min})^b$ of DC^b by looking for intersection points between the J and E contours (for illustration, these are marked by the

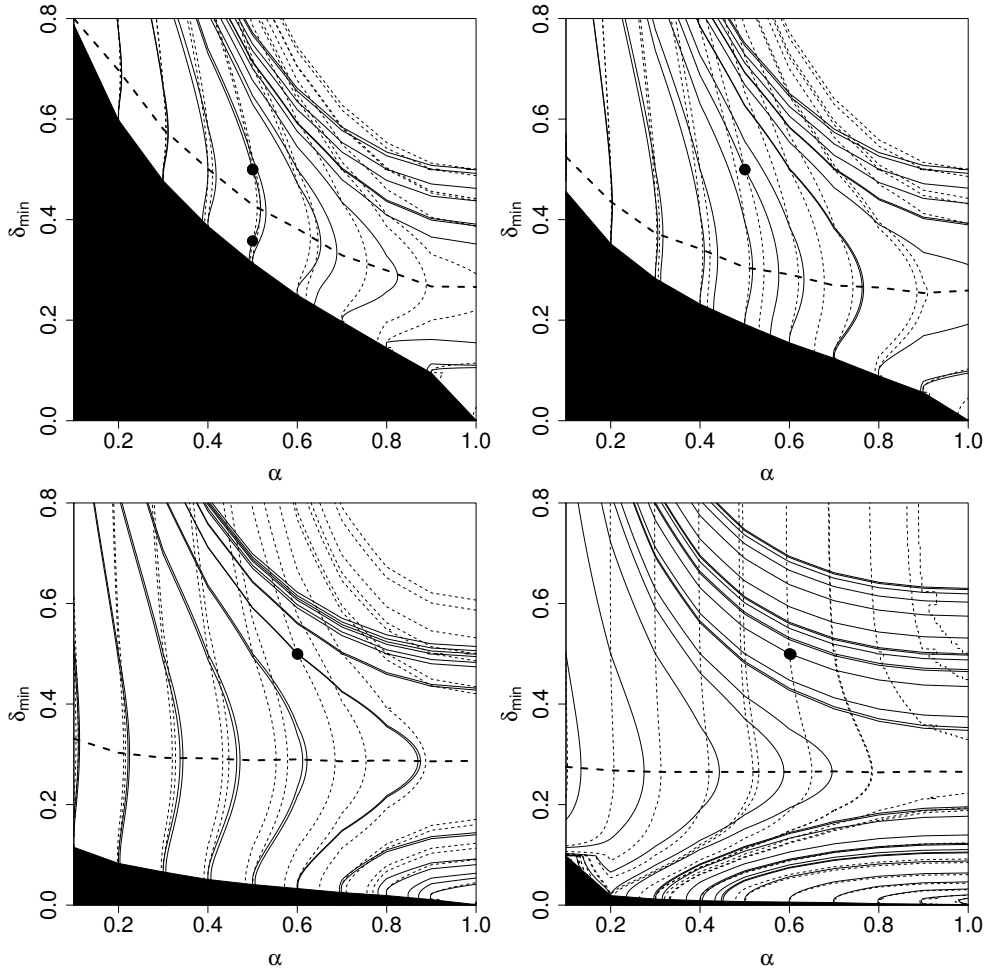

Figure 3.19: J (thin line) and E (dashed line) of DC states in the $\alpha - \delta_{min}$ parameter plane. From left to right, top to bottom, we show γ =0.25, 1, 3, and 10. The contours extracted (some of which may be close together) correspond to states with fixed (α, δ_{min}), where α=0.1–1.0 at $\Delta\alpha = 0.1$ and $\delta_{min} = 0.500$. States below the bold dashed line are unstable, and above – stable. The black dots mark the intersection points between the J and E contours corresponding to the same state, marking a possible complete transition from a pre-selected DC^a state. A complete transition into more than one unique DC^b state is possible when multiple black dots (i.e. multiple intersections) are present.

black dots in the figure for a given contour level). We find that complete transitions between two stable, two unstable, and an unstable and stable state are possible. However, as complete transitions between two stable states are unlikely to occur in real flows, and complete transitions between two unstable states would be short-lived, we only present results for complete transitions between unstable and stable states. Figure 3.20 shows these complete transitions in the $\alpha - \delta_{min}$ parameter plane. Possible complete transitions are connected by a grey line. Note that states below the bold dashed line are unstable, and those above are stable.

From figure 3.20 we see that states with small γ, and also ones with small α regardless of γ, undergo complete transitions in which α remains approximately unchanged, and only δ_{min} changes. As γ is increased, complete transitions which change both α and δ_{min} are possible for increasingly small α. In fact, when the maximum change in α is examined at each γ, we find that it increases almost perfectly linearly with γ, having a slope close to 0.057. At $\gamma = 0.25$ this maximum difference is 0.044, while at $\gamma = 10$ it is 0.591. Additionally, we see that for $\gamma \lesssim 1$ the change in δ_{min} between states is fairly uniform especially at a fixed α (with the standard deviation from the average being around 0.15), while for $\gamma > 1$ the complete transitions are more varied, with complete transitions having both small and large changes in δ_{min} (here, the standard deviation is around 0.21). A final point to note is that for larger γ, there exist more possible complete transitions than for smaller γ, for the discrete sampling chosen. Note that in fact a continuum of transitions are possible.

As shown above, complete transitions from one equilibrium state to another are possible. However, they do not appear to be preferred. We have induced small perturbations (as in §3.4) on unstable equilibria for which inviscid transitions to a stable equilibrium are known to exist to see if such a predicted complete transition would occur. We find that for transitions from unstable

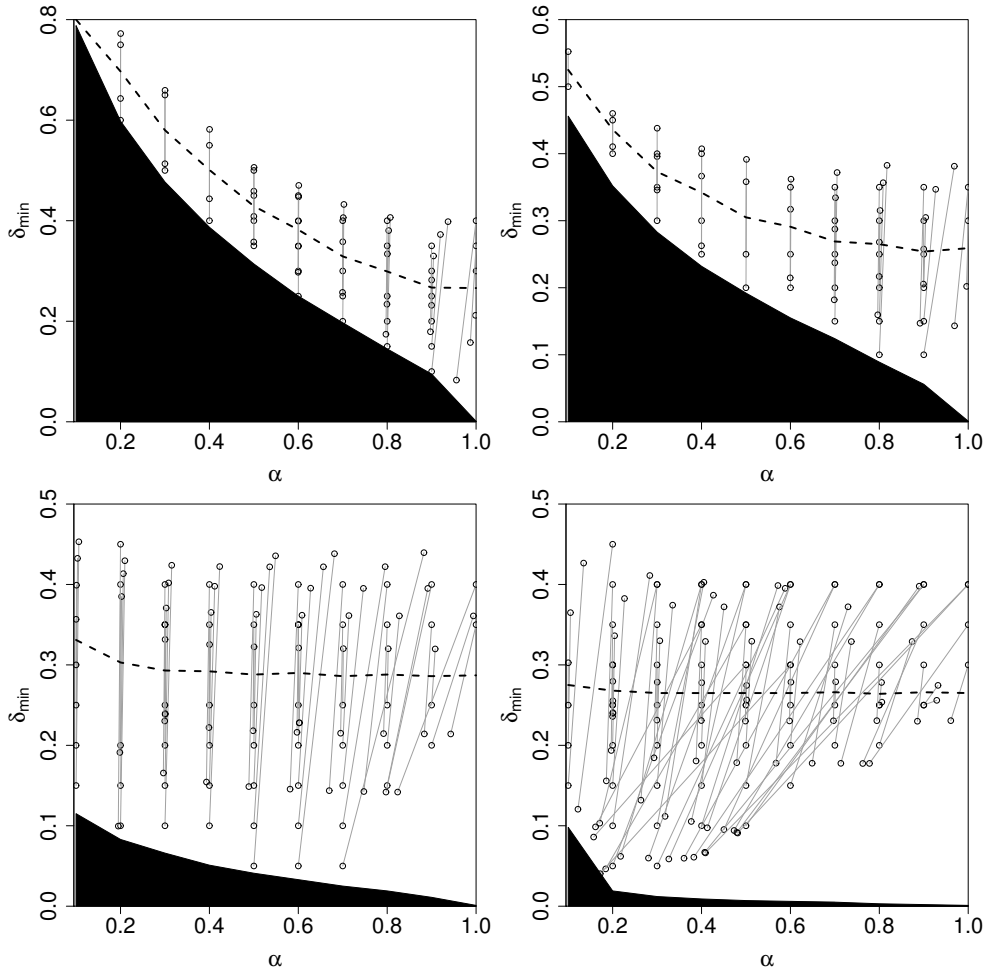

Figure 3.20: A summary of complete transitions, connected by the grey lines, possible between two DC states. From left to right, top to bottom, we show γ =0.25, 1, 3, and 10. States below the bold dashed line are unstable. We only show complete transitions between unstable and stable states. Note the different scales on the y-axis between the figures.

SC states to stable DC states there is always loss of J and E (recall that such complete transitions are only possible for small-γ states and note that we do not find complete transitions between an unstable DC state and a stable SC state, cf. figure 3.18). The same is true for transitions between two DC states at both small γ, and at large γ for small $\alpha \lesssim 0.4$. At large γ and large $\alpha \gtrsim 0.4$, we find that J and E are conserved, but rather than undergoing the complete transition into a DC state predicted by the above analysis, the state either exhibits vacillations around a stable steady state or complete merger, and thus transitions to an SC state. At large γ, all of the complete transitions between SC and DC states have been found to be between two *stable* states. The newly formed SC state has waves travelling on its boundary, and thus cannot be considered to be in equilibrium, as discussed below. This in turn implies that even at large γ and large α, inviscid transitions do not occur.

Although generally we do not find evidence for inviscid transitions, we observe that near the boundary of stability both small- and large-γ states which undergo unstable evolution reach unsteady end states with waves travelling on their boundary, as seen in the previous section. The long-time persistence of these newly formed states points towards their oscillation around an underlying equilibrium state, albeit with energetics different from those of the initial steady state. However, determining the underlying equilibrium from energetics is not possible, as the waves, which occur on the vortex boundary where most of the kinetic energy of the state is present, carry (negative) energy. This makes the total energy of the system lower than that of the underlying equilibrium state. Damping the waves during the unstable evolution, while at the same time preserving area in order to be able to find the underlying equilibrium could be done, but is *ad hoc*. Additionally, as the waves also carry J, determining δ_{min} or λ of the newly formed state (even from time-averaged values) is not meaningful despite the final α^f of the newly formed state being known. There is thus no

straightforward procedure to determine the underlying equilibrium states, even though they are likely to exist.

3.6 Conclusions

We have examined the form, properties and stability of asymmetric single-layer quasi-geostrophic shallow-water doubly-connected rotating equilibria. In this framework, the equilibria depend on three parameters: the ratio γ between the mean horizontal size of the vortices L and the Rossby deformation length L_D, the ratio α between the areas of the smaller and the larger vortices, and the minimum distance δ_{min} between the two vortices. Extending the work of Polvani et al. (1989) and Dritschel (1995) we have explored the $\gamma - \alpha - \delta_{min}$ parameter space, and for each (γ, α) we have found the margin of stability $\delta_{min} = \delta_c$, correct to within $\Delta\delta_{min} = 10^{-3}$.

By both performing a linear stability analysis and examining the nonlinear evolution of the equilibria, we have related the principal modes of linear stability to different types of evolution. We have found two principal modes of linear stability, occurring for small γ and large γ, with a transition region between them. The small-γ mode, absent for states with $\alpha \gtrsim 0.6$, is associated with either one, or both of the vortices getting smaller through an asymmetric instability where the smaller vortex sheds a filament from one of its tips. The large-γ mode, present for all α when $\gamma \gtrsim 3$, is associated with a suppression of filamentation and with the merger of the two vortices. The transition zone between the two (also present for $\alpha \gtrsim 0.6$, but for small $\gamma \lesssim 2$) is characterised by a series of merging and splitting events, with the state losing area in the process, as it tries to reach a quasi-steady simply-connected state, but is unable to do so.

The effects of non-zero γ cause the behaviour of the vortices to become α-independent. For $\gamma \gtrsim 2$, the critical distance δ_c between the vortices is almost

identical for all α (with it being slightly larger for $\alpha = 0.2$). As γ is decreased to the barotropic case $\gamma = 0$, the effects of α become increasingly pronounced, with more asymmetric states being unstable for larger δ_{min} than symmetric ones.

Noting the fast return of the flow to a quasi-steady state after an instability has taken place, we have examined possible inviscid transitions between two doubly-connected states or, using the results found in chapter 2, between a doubly-connected and a simply-connected state (which is described by γ and its aspect ratio λ). We find that although inviscid transitions are possible, they are not the preferred path of evolution. Small-γ states preserve neither angular impulse nor energy during unstable evolution, and a dissipative transition rather than an inviscid one is favoured in this regime. Large-γ states, which preserve both energy and angular impulse, favour merger rather than the predicted inviscid transitions into other doubly-connected states, despite the fact that inviscid transitions between an unstable doubly-connected state and a steady simply-connected state have not been predicted to occur. We believe this is a result of the unsteadiness induced by the instability. We find that the simply-connected state formed does split (instantaneously) at late times, but the existence of large-amplitude waves on its boundary prevents the split from being permanent.

To summarise, we have found that the stability of a vortex pair is not affected by the degree of its asymmetry for large vortices ($L \gg L_D$), although it does affect the underlying steady state into which an unstable state transitions. We have also found that for a fixed α and δ_{min}, smaller vortices are more likely to be unstable than larger ones, meaning that large vortices can sustain greater deformations induced by the flow of another vortex than smaller ones.

3.7 Supplementary movies

Supplementary movies are available on the compact disc attached to this thesis in the folder DC, with movie captions available in Appendix C.2. They are also available online at http://dx.doi.org/10.1017/jfm.2013.104.

Chapter 4

Shallow-water simply-connected quasi-equilibria

The following chapter consists of a study submitted to the *Journal of Fluid Mechanics* and the work is reproduced here with minor modifications.

4.1 Introduction

In chapter 2 we extend the work of Polvani et al. (1989), who studied dumbbell-shaped quasi-geostrophic shallow-water (QGSW) vortex-patch relative equilibria, which bifurcate from the Kirchhoff elliptical vortex (Kirchhoff, 1876) at finite Rossby deformation lengths. In QGSW, the families of these states are completely spanned by two parameters: their aspect ratio λ, namely the ratio between their minor to major axes, and their horizontal size L relative to the Rossby deformation length, $\gamma = L/L_D$. Note that our γ^{-2} is equivalent to the Burger number. In this chapter, we extend this work into shallow-water (SW), the simplest model which permits "balanced" vortical motions, ageostrophic effects, and "unbalanced" inertia-gravity waves (IGWs). A higher-order balanced model in

which the unbalanced component has been filtered out could be used to study ageostrophic effects. However, the choice of the order of balance to resolve is arbitrary, and so the SW model, which includes all orders of balance is used. As a result of the presence of ageostrophic motions, the symmetry which exists in geostrophically balanced models between motions spinning in opposite directions is broken. This allows us to study differences between cyclones, which spin in the same direction as the Coriolis frequency f (twice the background rotation rate Ω), and anticyclones, which spin in the opposite direction to f (in the northern hemisphere, the counter-clockwise and clockwise directions, respectively).

Only one additional parameter, the Rossby number $\mathcal{R}$, is required for the study of vortex-patch equilibria of chapter 2 in shallow-water. The Rossby number is a dimensionless measure of the strength of a vortex, defined as the ratio between the relative vorticity ζ and the Coriolis frequency, $\mathcal{R} = \zeta/f$. In geostrophically balanced systems where the motions are symmetric, $\mathcal{R} \equiv 0$; for cyclones $\mathcal{R} > 0$, whereas anticyclones have $\mathcal{R} < 0$. Our aim is to see to what extent the known QGSW equilibria are steady when extended into the SW context. Note that in shallow-water, due to spontaneous emission of IGWs, any equilibria generated are not strictly steady, but radiate such weak gravity waves that they may be deemed steady for all practical purposes. We further aim to determine how the stability of shallow-water equilibria is affected by their size and strength, and to classify the types of instabilities near the boundary of stability. Finally we wish to explore what role the unbalanced component of the flow plays during instability.

This chapter is organised as follows. In §4.2 we describe the model formulation used and provide an overview of the numerical method and the flow initialisation procedure. In §4.3 we discuss how we quantify the degree of steadiness, while in §4.4 we present the extent to which the stability of the equilibria is affected by vortex size and strength, and in so doing address the cyclone-anticyclone asym-

metry. Examples of the types of unstable evolution we find near the boundary of stability for various γ and $\mathcal{R}$ are shown in §4.5, and in §4.6 we quantify imbalance in both stable and unstable states. We end with some conclusions in §4.7, and provide information on supplementary movies in §4.8.

4.2 Model formulation

Below, in §4.2.1, we start by describing the theoretical framework used in this chapter — the shallow-water model. In §4.2.2 we discuss how we set up the flow in this system, providing details about the initial conditions used. Then, in §4.2.3 we give an overview of the Contour Advective Semi-Lagrangian (CASL) numerical algorithm used for evolving the flow.

4.2.1 The shallow-water model and the concept of balance

In this chapter, we use the full shallow-water (SW) model (see e.g. Pedlosky, 1979), which describes the motion of an incompressible fluid subject to planetary rotation and gravity effects. We use the single-layer, constant density form of the model on the f-plane, which is expressed by the shallow-water equations

$$\frac{Du}{Dt} - fv = -c^2 \frac{\partial h}{\partial x}, \tag{4.1}$$

$$\frac{Dv}{Dt} + fu = -c^2 \frac{\partial h}{\partial y}, \tag{4.2}$$

$$\frac{\partial h}{\partial t} + \nabla \cdot (\boldsymbol{u} h) = 0, \tag{4.3}$$

where $\boldsymbol{u} = (u(x, y, t), v(x, y, t))$ is the (horizontal) velocity, $h(x, y, t)$ is the fluid depth (or height) scaled on the mean fluid depth H, and $c = \sqrt{gH}$ is the short-scale gravity wave speed, with g being the gravity. The operator for the material derivative acting on a scalar a is defined to be $Da/Dt = \partial a/\partial t + \boldsymbol{u} \cdot \boldsymbol{\nabla} a$.

The flow described by the SW equations may be decomposed into two parts: the dominant, low frequency "balanced" component relating to vortical motions, and a faster, relatively short-lived "unbalanced" component consisting of ageostrophic motions and inertia-gravity waves. It is beneficial to view the balanced, vortical motions as local concentrations of potential vorticity (PV), a scalar, which in the absence of viscous and diabatic effects is materially conserved by fluid particles. In shallow-water, the PV q is defined to be

$$q = \frac{\zeta + f}{h}, \tag{4.4}$$

where $\zeta = \partial v/\partial x - \partial u/\partial y$ is the vertical component of vorticity. The statement of conservation of PV, $\mathrm{D}q/\mathrm{D}t = 0$, is a direct result of equations (4.1)–(4.3), and can also be made for its anomaly relative to a constant background value, $q' = q - f$. In QGSW, in which the unbalanced component has been completely filtered out, it is possible to determine exactly all dynamical fields from the instantaneous distribution of (QG)PV. In SW, the exact separation of a flow into a balanced and an unbalanced component is not possible for unsteady flow, as the "slow manifold" completely devoid of IGWs does not exist (Ford et al., 2000). Instead it makes sense to speak of "minimally unbalanced" flows, which are set up in a way to contain as little inertia-gravity waves as possible. For such a "minimally unbalanced" flow it is no longer possible to determine exactly the dynamical fields from the distribution of PV. Nevertheless, through what is known as the "invertibility principle" (Hoskins et al., 1985) various, sometimes very accurate, methods for approximating them do exist (McIntyre and Norton, 2000; Mohebalhojeh and Dritschel, 2000; Mohebalhojeh, 2002; Dritschel and Viúdez, 2003; McKiver and Dritschel, 2008, and others). These enable one to estimate the ageostrophic part of the flow arising from PV, as well as the proportion of IGWs in a flow.

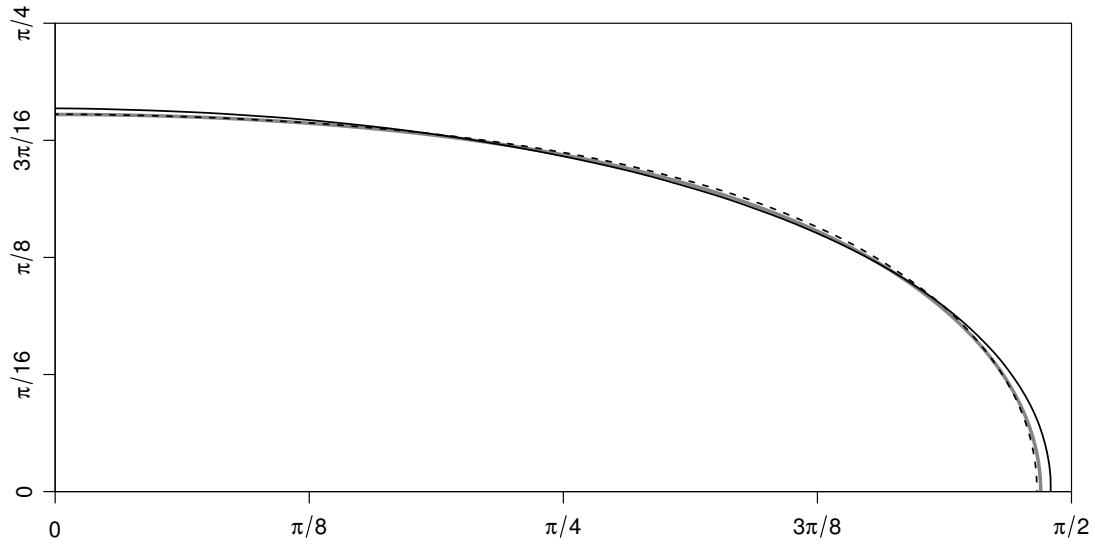

Figure 4.1: PV contours of states with $\gamma = 1$ and $\lambda = 0.400$ at time $t = \Delta_\tau = 10T_{ip}$ at the end of the ramping period. We show equilibria with three different $\mathcal{R}$: the initial QGSW state with $\mathcal{R} = 0$ (grey line), a cyclonic state with $\mathcal{R} = 0.5$ (dashed black line), and an anticyclonic state with $\mathcal{R} = -0.5$ (solid black line). Note that the cyclonic and anticyclonic states have been rotated to be aligned with the x-axis.

4.2.2 Flow initialisation

The solutions of the SW equations can describe a variety of realistic geophysical motions. Here, we seek those which represent relative vortex equilibria (referred to as just "equilibria"), or states which appear stationary in a co-rotating frame of reference. We do this by making use of the simply-connected two-fold symmetric relative equilibria generated by Polvani et al. (1989) and in chapter 2. In the QGSW model of the aforementioned studies, these states consist of a patch of constant QGPV in a background of zero PV, and are fully described by two parameters: their size relative to the Rossby deformation length, γ, and their aspect ratio, λ. In shallow-water, only one additional parameter is necessary to describe the vortex-patch equilibria – the Rossby number, $\mathcal{R}$, measuring the strength of the vortex relative to the background rotation. The PV anomaly inside the vortex patch is then defined in terms of the Rossby number by $q' = \mathcal{R}f$.

We generate shallow-water equilibria from QGSW ones (formally at $\mathcal{R} = 0$) by using a modification of the "optimal PV balance" (OPV) procedure of Viúdez and Dritschel (2004b). The OPV procedure starts with a flow at rest, and artificially ramps up the PV anomaly of each fluid particle by multiplying it by a ramp function $T(\tau) = \frac{1}{2}[1 - \cos(\pi\tau/\Delta_\tau)]$, which varies smoothly between 0 and 1 from the beginning ($\tau = 0$) to the end ($\tau = \Delta_\tau$) of the ramping period. Apart from the ramping of PV, the full SW equations are solved. The "target configuration", having only minimal amounts of imbalance if a sufficiently long Δ_τ is considered (in practice, exceeding 3 inertial time periods $T_{ip} = 2\pi/f$), is determined through a series of backward and forward iterations, where τ plays the role of the iteration parameter. The procedure does not enforce any specific balance conditions (such as e.g. geostrophic balance), but does depend on the choice of Δ_τ. Because of the sometimes very large q' considered in this chapter, convergence to the target configuration for long enough Δ_τ to truly minimise the presence of IGWs is not possible. Therefore, instead of performing a series of iterations until the target configuration in which we specify how close the "balanced" PV contours and those of the target configuration need to be, we remove the condition on the closeness of the two solutions. We perform only one forward iteration, allowing the initial contours to adjust to the flow, even if it means that they differ significantly from the "balanced" ones. This allows us to consider $\Delta_\tau = 10T_{ip}$, which is sufficiently long for the generation of IGWs to be kept to a minimum while the flow adjusts itself around the PV anomaly. Once the prescribed PV anomaly is reached, the PV is thereafter conserved and allowed to evolve freely. The minimally-unbalanced flows initialised in this way allow for the study of equilibria, and any destructive effects of artificially generated IGWs are attenuated.

Figure 4.1 shows the original contours of PV for a QGSW state (the grey line in the figure) and those of a cyclonic (dashed black line) and anticyclonic one (solid black line) with $(\gamma, |\mathcal{R}|) = (1, 0.5)$ and $\lambda = 0.400$ at $t = \Delta_\tau$ at the

end of the ramping period. During the ramp, the SW states undergo rotation and are here shown rotated back to be aligned with the x-axis. For clarity, in the figure we only show the form of the contours in the first quadrant. We do not impose any symmetry on the PV contour during the ramp and so the effects of the doubly-period domain may lead to an asymmetry of the contour in different quadrants. However, the nearly-zero slope of the contours at $x = 0$ and the nearly-infinite one at $x \approx \pi/2$ are indicative of symmetry, and the remaining quadrants are qualitatively similar to the one shown. From figure 4.1 we see that at the end of the ramping period, despite being allowed to evolve freely, the SW contours still closely resemble the QGSW one. This is especially so for the cyclonic state. Despite over-estimating the locations of the extrema of the contour, the anticyclonic state is still remarkably close to the QGSW one. This is especially astonishing since we are considering $\mathcal{R} = -0.5$, where a considerable free-surface deformation (of over 15% of the fluid depth) has taken place. Therefore, we henceforth approximate that the QGSW value of λ is the same as the SW one at the end of the ramping period.

Note that as mentioned in the introduction, there is always a small amount of IGW radiation from SW vortices (see Ford et al., 2000, and references therein for a brief review of the topic of spontaneous gravity wave emission), so the states we generate are not strictly equilibria, but rather quasi-equilibria. However, as discussed in the next sections, by initialising the flow with only minimal amounts of imbalance, it is still useful to view the states through the concept of equilibrium. Here, we call our states "equilibria" in order to avoid the more cumbersome "quasi-equilibria" term.

In order to provide an overview of the parameter space of realistic flows, we generate equilibria for both small and large γ, namely for $\gamma = 0.25, 1, 2, 3, 4$ and 6 (this gives a range of Burger numbers between 16 and 0.028). We examine both cyclonic ($\mathcal{R} > 0$) and anticyclonic ($\mathcal{R} < 0$) states with Rossby numbers $|\mathcal{R}| \leq 1.0$

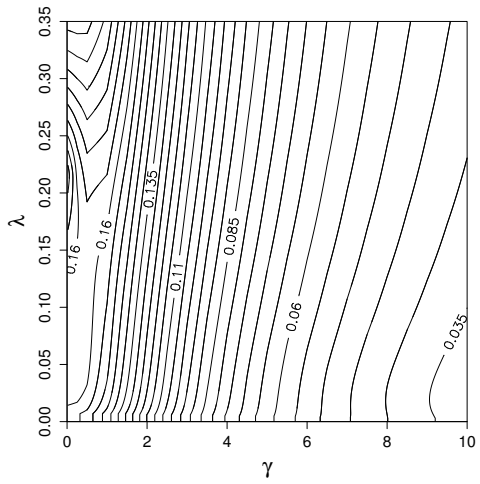

Figure 4.2: The particle rotation rate Ω_p (contour interval 0.005) of QGSW equilibria in the $\gamma - \lambda$ parameter plane. This figure is reproduced from figure 2.6(d) found in chapter 2.

at $\Delta\mathcal{R} = 0.1$.

4.2.3 Flow evolution

Having generated equilibria with non-zero $\mathcal{R}$, we solve the SW equations using the Contour Advective Semi-Lagrangian (CASL) algorithm (Dritschel and Ambaum, 1997; Dritschel et al., 1999). The algorithm keeps track of PV contours (across which q jumps by a prescribed increment Δq), and of the velocity and height field on a grid. Note that here we have only one contour defining the boundary of the equilibrium, with the jump $\Delta q = q' = \mathcal{R}f$. To improve the accuracy of simulating both the balanced and unbalanced components of the flow, a variable transformation is made from the standard set (u, v, h) to (q, δ, χ), where δ and χ are the divergence of the velocity and acceleration, respectively. Note that on the f-plane, χ/f is the ageostrophic vorticity. The primitive variables are then recovered from (q, δ, χ) via an inversion procedure so that PV contours can be advected, and the field tendencies calculated. The variable transformation results in a demonstrably more accurate representation of IGWs and vortical motions

(Mohebalhojeh and Dritschel, 2000; Smith and Dritschel, 2006). We evolve q using contour advection, while δ and χ are evolved using standard pseudo-spectral methods in a square doubly-periodic domain of side length 2π at a resolution of 256^2. The time stepping is carried out using a fourth-order Runge-Kutta scheme, with a time step chosen to marginally resolve the fastest gravity wave, i.e. $\Delta t = \Delta x/c$, where Δx is the grid spacing.

We use the CASL algorithm to evolve members of the families of equilibria for a range of γ and $\mathcal{R}$. At a fixed $(\gamma, \mathcal{R})$, by examining equilibria at different λ, by trial and error, we aim to determine the critical aspect ratio $\lambda_c = \lambda_c(\gamma, \mathcal{R})$ at which the equilibria cease to be stable, and to describe their unstable evolution near the boundary of stability. As a first guess for λ_c at $|\mathcal{R}| = 0.1$, we use the known QGSW value of $\lambda_c(\gamma, 0)$ determined in chapter 2. Increasing the Rossby number by a small amount only slightly modifies the form of the equilibria, and so too (it is found) the location of the boundary of stability. Once we determine $\lambda_c(\gamma, |\mathcal{R}| = 0.1)$, we continue to seek equilibria for progressively larger $|\mathcal{R}|$, using $\lambda = \lambda_c(\gamma, \mathcal{R}-0.1)$ (for cyclones) or $\lambda = \lambda_c(\gamma, \mathcal{R}+0.1)$ (for anticyclones) as a guess for $\lambda_c(\gamma, \mathcal{R})$. We determine the location of λ_c within an accuracy of $\Delta\lambda = 0.005$.

We evolve each steady state for at least 100 particle rotation periods T_p after the ramping of the PV anomaly has been completed. One T_p is the amount of time taken by a fluid particle to circuit the boundary of the equilibrium. In QGSW, $T_p^{QGSW} = 2\pi/\Omega_p$, where Ω_p is the particle rotation rate of the equilibrium, the values of which are shown in figure 4.2 in the $\gamma - \lambda$ parameter plane, as calculated in chapter 2. In SW, increasing the Rossby number increases particle velocities, and so we scale T_p accordingly by setting $T_p = T_p^{QGSW}/\mathcal{R}$.

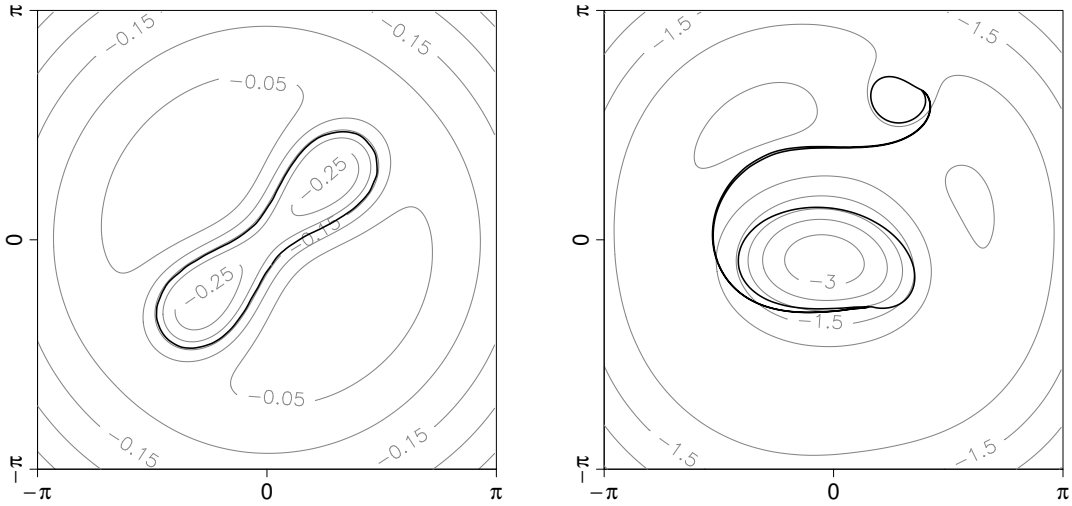

Figure 4.3: PV contours (black) and contours of the Bernoulli pressure function (grey) in the x-y plane. We see a stable state with $(\gamma, \mathcal{R}) = (3, 0.1)$ at $t = 53.08T_p$ (left; contour interval 0.1) and an unstable state with $(\gamma, \mathcal{R}) = (1, 0.3)$ at $t = 25.97T_p$ (right; contour interval 0.5), both near $\lambda = \lambda_c$.

4.3 Quantifying the degree of steadiness

The long-time persistence of the shallow-water equilibria we generate testifies to their steadiness, and thus their stability. However, we seek a more quantitative measure to verify this, and begin by noting that the Bernoulli pressure B and the PV are both functions of the streamfunction for steady (or steadily rotating) solutions of the SW equations (Malanotte-Rizzoli, 1982; Kizner et al., 2008). This means that in a steady flow, B is a constant on contours of PV, for an appropriately chosen frame of reference. In rotating shallow-water, the Bernoulli pressure function takes the form

$$B = hc^2 + \frac{1}{2}|\boldsymbol{u}'|^2 - \frac{1}{2}\Omega f(x^2 + y^2), \tag{4.5}$$

with the velocity in the rotating reference frame $\boldsymbol{u}' = (u + \Omega y, v - \Omega x)$ and Ω the rotation rate. Note that the rotation rate can be calculated following Dritschel (1995) by minimising the variance of the normal velocity along the PV contour.

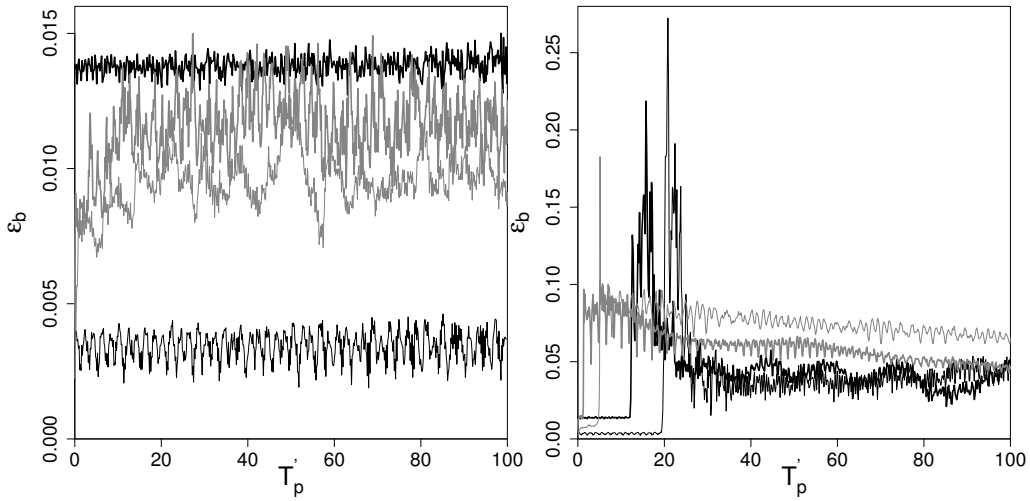

Figure 4.4: The value of ϵ_b as a function of time. Here, we show $\gamma = 0.25$ (black) and $\gamma = 6$ (grey) for $\mathcal{R} = -0.1$ (thin lines) and $\mathcal{R} = -0.5$ (bold lines) near the boundary of stability for steady, stable states (left) and unstable ones (right). Note that the two grey lines in the left panel are practically indistinguishable. We show how the flow develops for $100T_p$ once the ramping period has been completed, so "$t = 0$" occurs at the end of the ramping period, of duration $10T_{ip}$.

Figure 4.3 shows an example of the extent to which the contours of constant B (shown in grey) and PV (shown in black) are aligned for a steady, stable state (left-hand panel of the figure) and an unstable one (right-hand panel) near $\lambda = \lambda_c$. We see that for the stable state, the contours closely correspond, while crossing is apparent in the unstable one.

We check how close we are to a steady solution of equations (4.1)–(4.3) by defining the non-dimensional steadiness parameter ϵ_b, which measures how closely aligned the contours of PV and B are in a reference frame rotating with the equilibrium:

$$\epsilon_b = \frac{\sqrt{\frac{1}{P}\oint_{\mathcal{C}} (B - \bar{B})^2 \, ds}}{\bar{B}}, \tag{4.6}$$

where $P = \oint_{\mathcal{C}} ds$ is the arc length of the PV contour $\mathcal{C}$, and $\bar{B} = (1/P)\oint_{\mathcal{C}} B \, ds$ is the mean Bernoulli pressure around the PV contour. Figure 4.4 shows how ϵ_b changes through time for both stable, anticyclonic states (left-hand panel of the figure) and unstable ones (right-hand panel) near the boundary of stability.

In each panel of the figure, we show how γ and $\mathcal{R}$ affect the value of ϵ_b by showing it for states having $\gamma = 0.25$ at $\mathcal{R} = -0.1$ and -0.5 with black thin and bold lines, respectively, and for states having $\gamma = 6$ at the same $\mathcal{R}$ with grey thin and bold lines. We see that ϵ_b values are consistently small for the stable states, but also initially for the unstable states. Additionally, for the stable states, changing the Rossby number does not significantly affect the values of the steadiness parameter at $\gamma = 6$, whereas even though ϵ_b remains small for all time, the effects of increasing $|\mathcal{R}|$ are noticeable at $\gamma = 0.25$ (we return to this point in §4.4). On the other hand, the effects of $|\mathcal{R}|$ are not visible in the unstable states, where the value of ϵ_b seems to instead depend on γ, with small-γ vortices having larger ϵ_b values than large-γ ones. This mainly results from the difference in the types of unstable evolution small and large vortices undergo (see §4.5). After an instability has taken place, the flow returns to a quasi-steady state, with the value of ϵ_b falling again. This return to steadiness is quicker and more pronounced at small γ, but a downward trend is also visible for states at higher γ. We additionally note that for the stable states, the value of ϵ_b has quasi-periodic behaviour, and we re-examine this point in §4.6, linking it to the presence of the unbalanced component of the flow.

Throughout this chapter we refer to states which are "steady", and ones which are "stable" and "unstable". After the initial PV ramping procedure is completed, the values of ϵ_b for all of the states considered in this chapter are low. This is true for both the "stable" and "unstable" states (cf. figure 4.4, especially at early times for the unstable states). For the "stable" ones, ϵ_b stays small for the entire duration of the simulation, while for the "unstable" states there is a sudden spike in ϵ_b at some time $t = t_c$, during which the vortex undergoes unstable evolution. We do not attempt to perform a formal linear stability analysis of our equilibria, as doing so in SW is extremely difficult. However, we do determine a boundary of "stability" at $\lambda = \lambda_c$, such that for $\lambda > \lambda_c$, if left undisturbed, the vortex

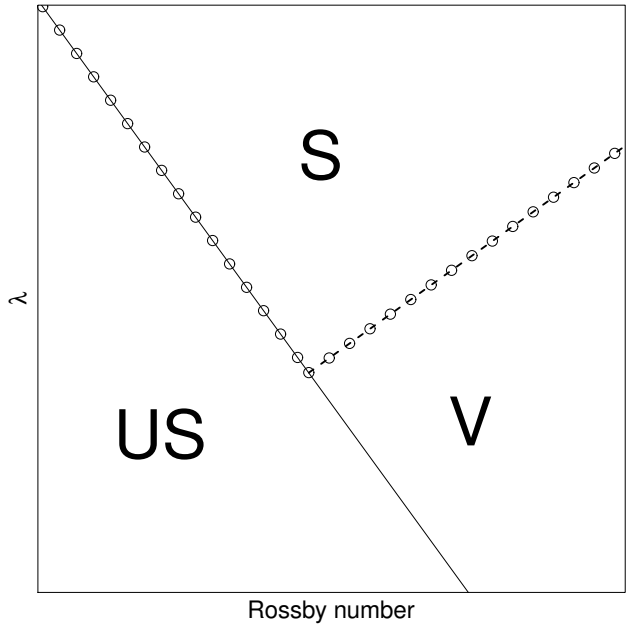

Figure 4.5: A schematic showing the location of λ_c (solid line), λ_v (dashed line) and λ_s (circles) as a function of $\mathcal{R}$ for a fixed γ. The region denoted by "US" indicates the unstable regime, by "V" the vacillating regime, and by "S" the stable regime. Note that for some Rossby numbers, only one of λ_c or λ_v may exists.

persists for long times without change in shape, and for $\lambda < \lambda_c$ it undergoes unstable evolution. Hence when "stable" states are referred to in this chapter, these are states which do not change in shape throughout the (sufficiently long) duration of the simulation, while "unstable" states are ones which do change in shape significantly.

The steadiness parameter ϵ_b is a good measure for determining the critical aspect ratio λ_c at which there is a very sharp spike in ϵ_b. However, for states with $\gamma > 1$, through a visual examination of the equilibria, we find weakly-unstable states for which ϵ_b has low values for all time. Unlike the states having $\lambda < \lambda_c$, these states do not undergo major changes in shape, and instead exhibit quasi-steady vacillations, during which their aspect ratio goes through cycles of increasing and decreasing its value. This process is sufficiently slow that the Bernoulli pressure B is able to adjust itself about the vortex, and no signal of the

weak instability is apparent in ϵ_b. We introduce the vacillating aspect ratio λ_v, such that for any $\lambda_c < \lambda < \lambda_v$ the state undergoes vacillations, while for $\lambda \geq \lambda_v$ it is stable. Determining the exact location of λ_v is difficult, as for λ ranging from λ_c to λ_v the change in aspect ratio during one vacillation cycle, $\Delta\lambda_{cyc}$, decreases. We define λ_v to be the smallest aspect ratio at which, for an appropriate choice of b, $\Delta\bar{\lambda}_{cyc}/\lambda_i < b$, where λ_i is the initial aspect ratio of the state. We take the average of $\Delta\lambda_{cyc}$ throughout the simulation, $\Delta\bar{\lambda}_{cyc}$, and scale it by λ_i to account for the wide range of λ_i considered. We set $b = 0.05$ since in shallow-water even balanced, steady states generate a small amount of IGWs, and hence there is always some deformation to the shape (and mass) of the state. We have deemed that a change of less than 5% in the initial aspect ratio is sufficiently small for a state to be termed steady. Additionally, as λ_v only exists for states with $\gamma > 1$, we introduce the steady aspect ratio λ_s such that all states with $\lambda > \lambda_s$ are steady; then $\lambda_s = \lambda_c$ when vacillations do not occur, and $\lambda_s = \lambda_v$ when they do. Figure 4.5 shows a schematic of the of locations of λ_c, λ_v and λ_s, along with the stability regions they bound. The location of λ_c and λ_v in the parameter space considered is discussed in detail in §4.4, of which a summary is presented in figure 4.8. However, before discussing the stability of the equilibria, we first examine a few of their properties.

At a fixed $(\gamma, \mathcal{R})$, figure 4.6 shows $\bar{\epsilon}_b$, the time average of ϵ_b (over the duration of a simulation) for the stable states near λ_s. We see that in general, at a fixed γ, states with smaller $|\mathcal{R}|$ have lower values of $\bar{\epsilon}_b$ than do states with larger $|\mathcal{R}|$. This is to be expected, as the amplitude of the free-surface deformations caused by the vortex increases with $|\mathcal{R}|$. The cyclone-anticyclone asymmetry is also apparent from the figure, where for all γ, at a fixed $|\mathcal{R}|$, cyclones have *lower* values of $\bar{\epsilon}_b$ than anticyclones. This asymmetry is strongest for small-γ states, and weakens as γ increases. Additionally, we see that for large-γ cyclonic states, the value of $\bar{\epsilon}_b$ becomes $\mathcal{R}$-independent, while for anticyclones there is a strong variation with $\mathcal{R}$.

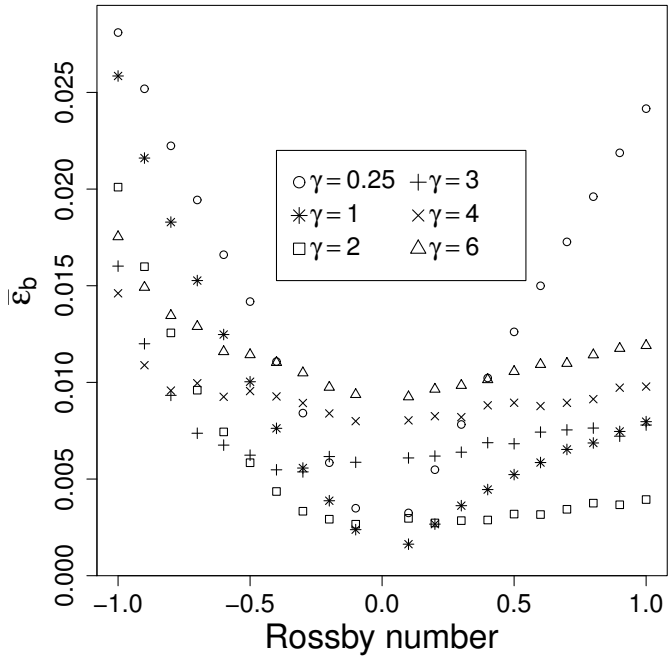

Figure 4.6: The time-average (over the duration of the simulation) of the steadiness parameter, $\bar{\epsilon}_b$, at a fixed $(\gamma, \mathcal{R})$ for the range of γ and $\mathcal{R}$ considered. Here, we show the average of $\bar{\epsilon}_b$ for stable states with $\lambda - \lambda_s < 0.020$.

Finally, we note that as the QGSW ($\mathcal{R} = 0$) states are balanced, then $\bar{\epsilon}_b \equiv 0$. We see that for small-$\gamma$ states, we do get convergence towards this limit. However, for large-γ states there is a discontinuity occurring at $\mathcal{R} = 0$. We readdress this issue in §4.4.

In figure 4.7 we show the mass M, i.e.

$$M = \iint_{\mathcal{D}} (H + h') \mathrm{d}x \mathrm{d}y, \tag{4.7}$$

of the equilibria at the end of the ramping period (at time $t = 10T_{ip}$) as a function of $\mathcal{R}$ for the range of γ considered near $\lambda = \lambda_s$. Here, $H = 1$ is the mean fluid depth, h' is the depth anomaly, and the integration is performed over the region inside the vortex $\mathcal{D}$, defined by the PV contour. For simplicity, we only describe the anticyclonic case, though the same arguments can be made for cyclones which have a negative, rather than positive, depth anomaly h', and at small $|\mathcal{R}|$ are anti-

symmetric to the anticyclonic states. We see that for the anticyclonic states, as $|\mathcal{R}|$ increases, so does the amount of mass contained within the vortex, as h' also increases. Additionally, at a fixed $\mathcal{R}$, vortices with larger γ contain greater mass. Larger vortices (with larger γ) also feel the effects of increasing $|\mathcal{R}|$ more. The mass contained by the $\gamma = 0.25$ equilibria at $\mathcal{R} = -0.1$ and $\mathcal{R} = -0.6$ differs by around 1%, whereas for the $\gamma = 6$ equilibria this difference is about 36%.

We note that for both cyclones and anticyclones, at small $|\mathcal{R}|$, there appears to be a linear relationship between M and $\mathcal{R}$. We attempt to explain this as follows. It is known that in shallow-water, near the quasi-geostrophic limit (for small $|\mathcal{R}|$), the mass anomaly scales like $m' \sim \mathcal{F}^2/\mathcal{R}$ (see e.g. Vallis, 2006), where $\mathcal{F} = U/c$ is the Froude number. This can be shown by performing a scale analysis of the permissible free surface deformations η in geostrophic balance $\eta \sim fUL/g = R\gamma = Fr^2/R$ (these deformations are proportional to mass when, as here, the density of the fluid is constant). For large γ, the maximum speed on the vortex edge scales like $U \sim \mathcal{R} f L_D$ (Nycander et al., 1993). Hence, since $c = fL_D$, $\mathcal{F} \sim \mathcal{R}$ which implies $m' \sim \mathcal{R}$ as observed. We find in fact that this scaling holds for all of the γ considered (including $\gamma < 1$), and for values of $|\mathcal{R}|$ up to 0.4. The departures from this linear relationship are less than 0.07 at large γ and up to two orders of magnitude smaller at small γ. Note that the amount of mass added (subtracted) by anticyclones (cyclones) is not symmetric, and at a fixed $|\mathcal{R}|$, anticyclones contain more mass than cyclones are able to displace. Finally, we note that as we are in fact considering quasi-equilibria which are not strictly steady, small fluctuations in mass do occur for the stable states. However, these are $\ll 1\%$ of the total mass for states with $\gamma \lesssim 3$ and no more than 2.4% for large-γ states.

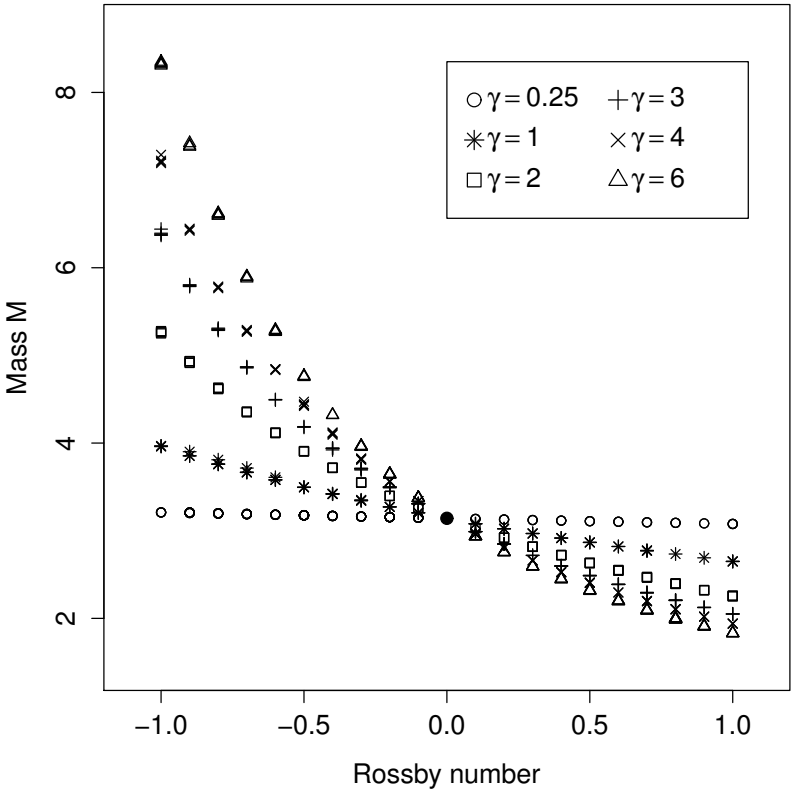

Figure 4.7: The mass M of the equilibrium at the end of the ramping period, shown as a function of $\mathcal{R}$ for the steady states near $\lambda = \lambda_s$. The filled in point indicates the QGSW mass $M = \pi$.

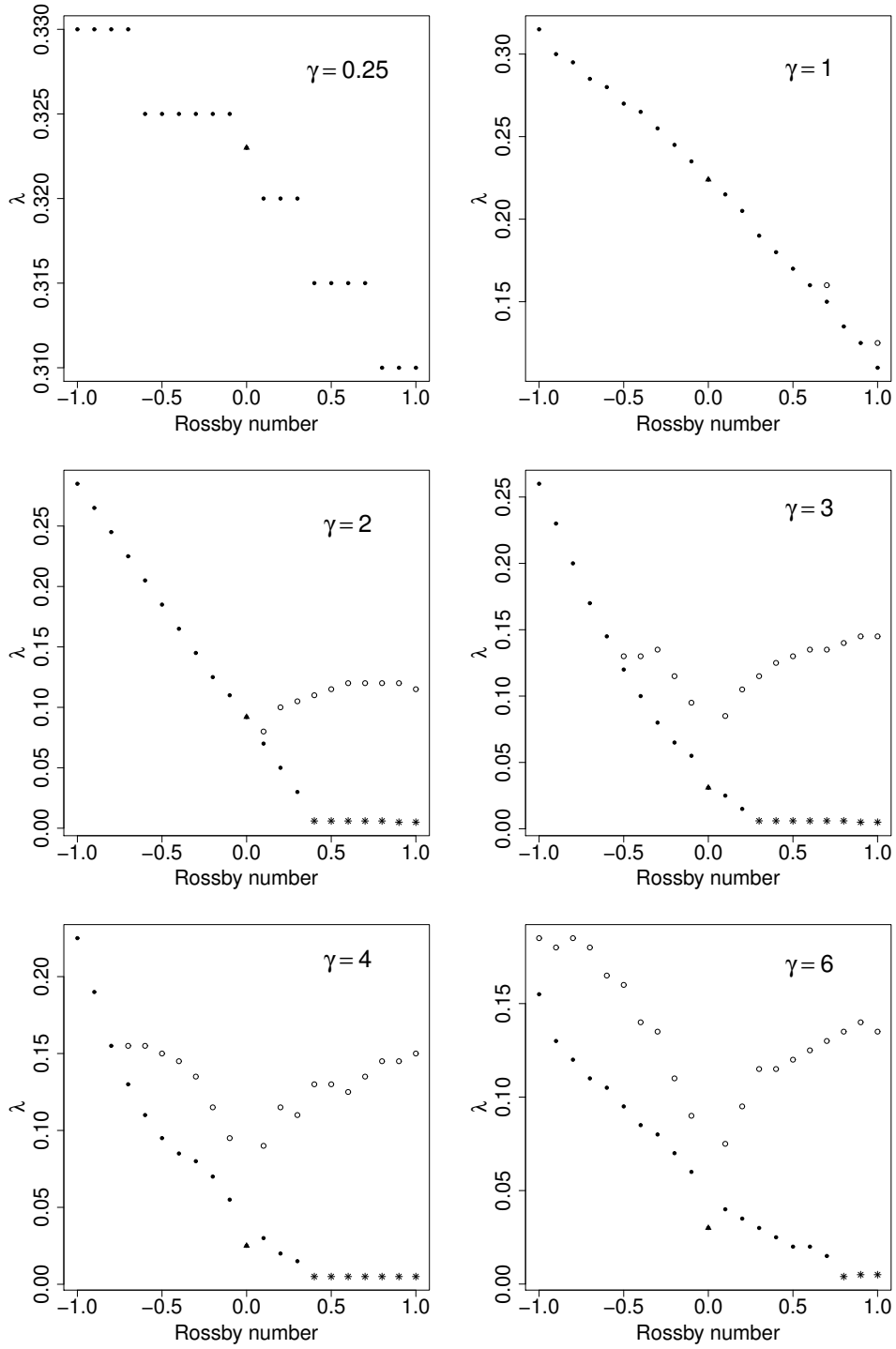

Figure 4.8: The location of λ_c (filled-in circles) and λ_v (circles) as a function of $\mathcal{R}$ for various γ, as labelled. The triangle in each plot shows the location of the QGSW λ_c, and the asterisk indicates a vacillating state with the smallest λ we have been able to generate, which is weakly-unstable. Note the range in λ varies with γ, and that we determine λ_c and λ_v to within $\Delta\lambda = 0.005$.

4.4 Stability

We next discuss how the stability of the equilibria discussed above varies with γ and $\mathcal{R}$, and thus study the naturally-occurring asymmetry between cyclonic and anticyclonic vortices. We say that a vortex is stable (sometimes also weakly unstable) when it undergoes no major structural changes for at least $100T_p$ after the end of the ramping period. We measure this via the steadiness parameter ϵ_b, in which a clear jump is visible during the onset of instability (cf. figure 4.4) providing us with the location of the critical aspect ratio $\lambda_c(\gamma, \mathcal{R})$. Additionally, for larger γ, we find the location of the vacillating aspect ratio $\lambda_v(\gamma, \mathcal{R})$, and thus find $\lambda_s(\gamma, \mathcal{R})$, such that at a fixed $(\gamma, \mathcal{R})$, all states having $\lambda \geq \lambda_s$ are stable (see figure 4.5 for a visual representation of λ_c, λ_v, and λ_s). The different types of unstable behaviour are discussed in the next section, and here we focus on the location of the boundary of stability $\lambda_s(\gamma, \mathcal{R})$. Note that at some $(\gamma, \mathcal{R})$ only one of λ_c or λ_v may exist.

Figure 4.8 shows the location of λ_c (marked by filled-in circles in the figure) and λ_v (marked by circles) as a function of $\mathcal{R}$ for various γ. We also indicate states for which we do not find λ_c (marked by asterisks). These results offer the clearest picture of the cyclone-anticyclone asymmetry. Cyclones are generally *more* stable in that they remain stable for smaller λ than anticyclones. The difference is immediate even at small $\mathcal{R}$.

For $\gamma \lesssim 2$, λ_c varies nearly linearly with $\mathcal{R}$, and includes the QGSW limit $\lambda_c(\gamma, 0)$. For larger γ however, the QGSW limit value appears to depart from the collection of nearby points with $\mathcal{R} \neq 0$. That is, the QGSW state at $\mathcal{R} = 0$ can become noticeably more deformed before losing stability than nearby small $|\mathcal{R}|$ states. Recall that in §4.3, for large-γ states, we noted a similar discontinuity at $\mathcal{R} = 0$ in $\bar{\epsilon}_b$ (cf. figure 4.6). A complexity of behaviours is observed for large γ with $\mathcal{R}$ close to QG. We believe that this may happen because at large γ motions

are slow, and so the phase of a vacillation cycle may be comparable to the length of the ramping period Δ_τ. For a long enough ramping period it is plausible that the results will converge to the QGSW values. Given the range of parameters considered in this study, due to computational costs it was deemed impractical to do so in the present study. From figure 4.8 we also see that at large γ there is a change in slope in the line fitted through the values of λ_c for anticyclonic states, where it is shallower for small $|\mathcal{R}|$, and steeper for large $|\mathcal{R}|$. For example, at $\gamma = 4$, the slope of the line predicting the location of λ_c for $|\mathcal{R}| \lesssim 0.5$ is -0.11, while for $|\mathcal{R}| \gtrsim 0.5$ it is -0.29. For larger γ, this change occurs at higher $|\mathcal{R}|$: at $\gamma = 3$, it happens at $\mathcal{R} \approx -0.5$, while for $\gamma = 6$, at $\mathcal{R} \approx -0.9$. If we once again compare this behaviour to the results presented in figure 4.6, we see that at large γ, for states with $\mathcal{R} \lesssim -0.5$ the slope of the line fitted through the $\bar{\epsilon}_b$ values steepens compared to the slope of the line fitted through values with $\mathcal{R} \gtrsim -0.5$. Higher values of $\bar{\epsilon}_b$ mean that states become less steady, which is consistent with the steepening of the slope of the line through λ_c. We do not see this behaviour in cyclonic states, where the slope of the line fitted through $\bar{\epsilon}_b$ values does not change. However, for large-γ cyclones, at large $\mathcal{R}$, strong instabilities cease to occur. The value of $\mathcal{R}$ at which this happens increases with γ.

For small-γ states, the location of λ_c coincides with the location λ_s, in contrast to large-γ states ($\gamma \gtrsim 1$), where a region of weakly unstable states occurs. For $\gamma = 2$, vacillations only occur for cyclonic states, and although variations in the exact location of λ_v at different $\mathcal{R}$ are small, it appears that states with $\mathcal{R} \lesssim 0.6$ need to increase their aspect ratios for stability, and states with $\mathcal{R} \gtrsim 0.6$ can once again decrease it while retaining their stability. As γ increases, vacillations occur not only for smaller values of $\mathcal{R}$, but also for a wider range of λ. In fact, for $\gamma \geq 2$, at large $\mathcal{R} > 0.4$ this is the only type of instability which occurs. For cyclones, across all γ, the vacillating region expands as $\mathcal{R}$ increases, and states need to be less deformed in order to be stable. The same is true for anticyclones

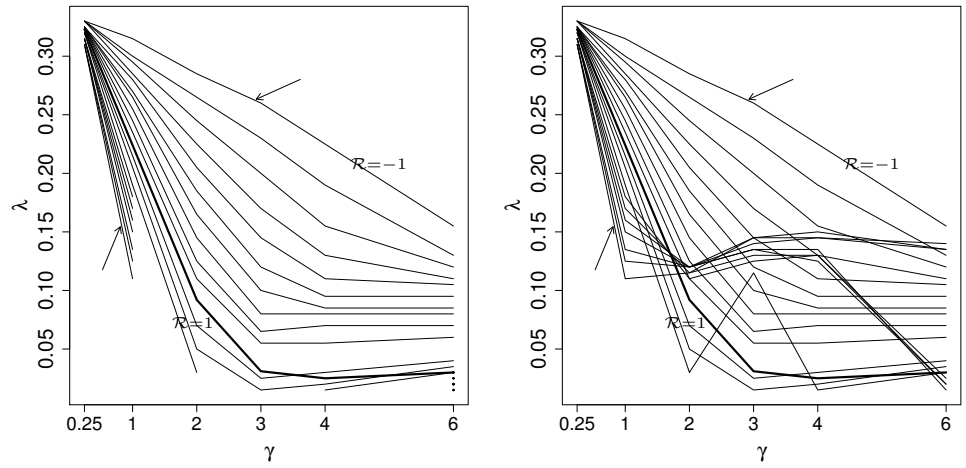

Figure 4.9: The location of λ_c (left) and λ_s (right) as a function of γ for the range of $\mathcal{R}$ considered. The bold line indicates the QGSW case $\mathcal{R} = 0$. Note that at certain γ and $\mathcal{R}$, λ_c does not exist, so lines may be cut off.

at small $|\mathcal{R}|$, but as $|\mathcal{R}|$ increases, for large enough λ_c no vacillations occur. This is most visible for $\gamma = 3$, where for $-0.5 \leq \mathcal{R} \leq -0.3$ the vacillating aspect ratio $\lambda_v \approx 0.130$, and as $|\mathcal{R}|$ increases it converges to λ_c. Similarly as with λ_c, at large γ, the location of λ_v appears to be converging towards $\lambda_c(\gamma, 0)$ in a nonlinear way. Note that apart from at certain λ values at $\gamma = 5$ and 6, in chapter 2 we found no evidence for vacillations in QGSW.

Figure 4.9 shows the locations of λ_c (left panel of the figure) and λ_s (right panel) as a function of γ for the range of $\mathcal{R}$ considered. We see that regardless of $\mathcal{R}$, large-scale effects tend to stabilise states, especially strongly cyclonic ones, as seen by the decrease in the location of λ_c and λ_s as γ increases. Additionally, we see that for large-γ states, the location of λ_s becomes γ-independent.

The determination of λ_s for anticyclonic states at $\gamma = 0.25$ has proved difficult, as in addition to being affected by an elliptical wavenumber-3 instability (hereafter the wave-3 instability, see Dritschel, 1986) which leads to the state shedding a filament from one of its tips, small-scale disturbances may develop on the vortex boundary, which grow in time and eventually lead to the state becoming unstable. The form of $\epsilon_b(t)$ is very different for such states, as shown in figure

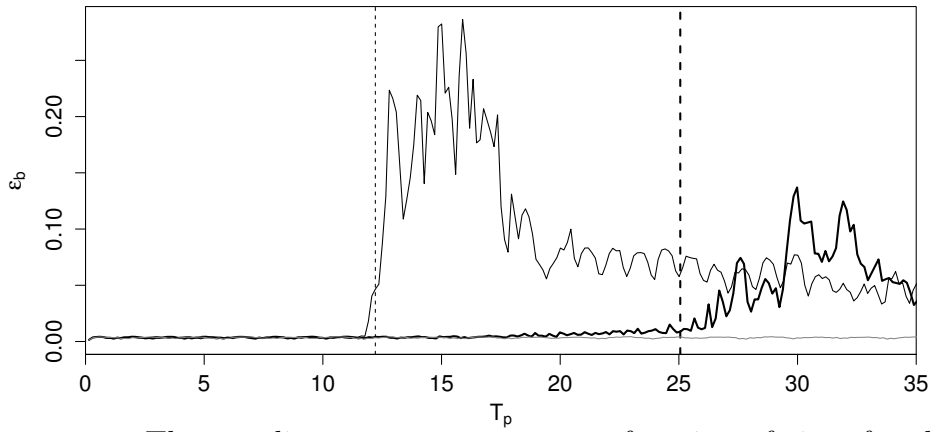

Figure 4.10: The steadiness parameter ϵ_b as a function of time for the case $(\gamma, \mathcal{R}) = (0.25, -0.1)$ near $\lambda = \lambda_c$. We see: an unstable state at $\lambda = 0.315$ (thin line), a stable state with a weak instability at $\lambda = 0.325$ (bold line), and a state stable for all time at $\lambda = 0.340$ (grey line). The times at which the first filament is shed are indicated with the two dashed lines.

4.10. As seen from the thin line in the figure, unstable states have a very sharp, clearly defined jump in ϵ_b, while weakly-unstable states exhibit a slow growth of ϵ_b up to and after the time the first filament is shed, which is marked by the thin and bold dashed vertical lines. A jump in ϵ_b may occur in the weakly-unstable state once the small-scale filaments shed by the vortex have interacted with its boundary to such an extent that a larger filament is shed. For comparison, in the figure we also show ϵ_b for a state which is stable for all time (grey line), and we see that the weakly-unstable state very gradually begins to depart from these values before a filament is shed. We find this type of "weak" instability occurring even at large aspect ratios, and it may be surrounded by extensive regions of stable aspect ratios. We therefore classify these weakly-unstable states as stable.

A clear difference in the stability of cyclones and anticyclones is visible in both figures 4.8 and 4.9. Many previous studies have examined the cyclone-anticyclone asymmetry, and in general it has been reported that in decaying shallow-water turbulence and in more realistic oceanic flows, large anticyclonic structures are more prevalent than their cyclonic counterparts (Olson, 1991; Arai and Yama-

gata, 1994; Polvani et al., 1994). Furthermore, cyclones are generally found to be more deformed than anticyclones (Aristegui et al., 1994). By analysing a large oceanic dataset, Olson (1991) showed that although anticyclones appear to be more long-lived, there is no evident asymmetry between the distribution of cyclones and anticyclones. The results of our study confirm the above results. Across all γ, we find that cyclones are able to sustain greater deformations than anticyclones while remaining stable. Anticyclones are in general believed to be more "stable" than cyclones, see e.g. Stegner and Dritschel (2000). We find the opposite – ageostrophic effects tend to stabilise cyclones and destabilise anticyclones. However, it is important to keep in mind that when comparing cyclonic and anticyclonic motions, it is necessary to define what is meant by two states which are "equivalent", as cyclones and anticyclones cannot simultaneously have identical (but oppositely-signed) velocities, PV and height anomalies. Here, we say two states are "equivalent" when they have the same magnitude of Rossby number $|\mathcal{R}|$ (which defines the PV anomaly), size γ relative to the Rossby deformation length, and aspect ratio λ. Stegner and Dritschel (2000) studied circular, isolated, distributed shallow-water vortices, and chose to examine "equivalent" vortices which shared the Burger number (recall that this is our γ^{-2}) and (oppositely-signed) relative vorticity profiles, hence the differences in their conclusions. To our knowledge, a careful study of the cyclone-anticyclone asymmetry, which spans a wide parameter space and where the "equivalence" between two states is clearly defined has not been previously performed. We find that cyclones are stable for a wider range of the parameter regime than anticyclones, and that large-scale effects tend to stabilise them more easily than anticyclones (cf. the steeper slopes of lines corresponding to states with $\mathcal{R} > 0$ in figure 4.9). We also find that for cyclones, a strong instability which results in the break-up of the vortex may not exist at all, and instead only a weak instability in the form of vacillations occurs. Anticyclones on the other hand are stable for a smaller portion of the parameter space, and, especially at large $|\mathcal{R}|$, are less

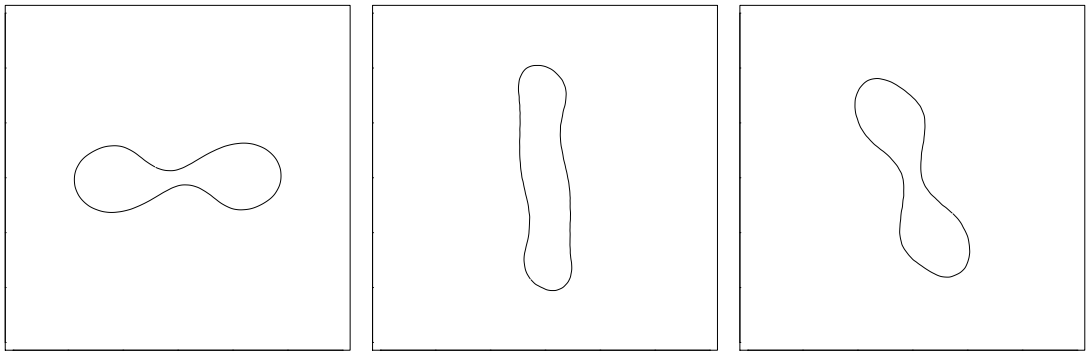

Figure 4.11: An example of a vacillating state having $(\gamma, \mathcal{R}, \lambda) = (6, 0.8, 0.005)$. We see time $t = 0.84T_p$ after the ramping period has finished (left), and times $t = 19.49T_p$ and $t = 22.85T_p$ when the state reaches a maximum (middle) and minimum (right) aspect ratio during a vacillation cycle. Here and in subsequent figures we see contours of the PV anomaly q', with $|x|, |y| \leq \pi$.

likely to experience vacillations.

4.5 Types of evolution

Below, we describe the types of unstable evolution that vortices exhibit near λ_c, and where they occur in the $\gamma - \mathcal{R}$ parameter space. We find four distinct types of instability regimes, which, following the classification made in chapter 2 in QGSW, we call type 1 instability for vacillating states, type 2 instability for states which shed a filament, and type 3i and 3ii instabilities, for states which split into two vortices of unequal or equal size, respectively.

We first show a few examples of the evolution of each of the types of instability. In figure 4.11 an example of the type 1 instability is shown – a weakly unstable, vacillating state having $(\gamma, \mathcal{R}) = (6, 0.8)$ at $\lambda = 0.005$, the smallest aspect ratio examined. As time progresses, we see that the state increases its initial aspect ratio λ_i (shown in the left panel of the figure) until some maximum value of a vacillation cycle λ_{max}^{cyc} (middle panel), before decreasing it again to λ_{min}^{cyc} (right panel). After the first few vacillation cycles where it is comparable to λ_i, λ_{min}^{cyc}

Figure 4.12: An example of a state having $(\gamma, \mathcal{R}, \lambda) = (0.25, 0.7, 0.310)$, which sheds a filament. We see the state, from left to right and top to bottom, at times $t = 21.22T_p$, $t = 21.73T_p$, $t = 22.24T_p$, $t = 22.50T_p$, $t = 23.52T_p$, and $t = 30.68T_p$.

settles down to a constant value which is greater than λ_i, while the value of λ_{max}^{cyc} has similar values for the entire duration of the simulation. As visible in the middle panel of the figure, there are large-amplitude waves travelling on the boundary of the equilibrium, which obey a modified Korteweg-de Vries equation to leading order in L_D (Nycander et al., 1993). The behaviour described above is typical of all vacillating states, although as λ_i increases towards λ_s, both the amplitude of the vacillation and that of the waves travelling on the equilibrium boundary decreases. As seen in figure 4.8 in the previous section, this sort of instability occurs only in states having $\gamma > 1$.

Figure 4.12 shows an example of the type 2 instability – for a state having $(\gamma, \mathcal{R}) = (0.25, 0.7)$ at $\lambda = \lambda_c = 0.310$, which sheds a filament in a wave-3 instability. As seen from the left and middle panels of the bottom row of the figure, further interactions between the original state and the filamentary debris can occur after the filament has been shed. The state eventually evolves towards a quasi-steady time-dependent state with $\lambda = 0.461$, which is well within the stable parameter regime (this λ is based on the second-order spatial moments of the patch). The state also has small values of ϵ_b, albeit larger ones than initially, as discussed in §4.3. As is visible in the bottom-right panel of the figure, parts of the filament may roll up to form small satellite vortices. For states with $\gamma = 0.25$, these satellite vortices are negligible in size and make up less than 0.3% of the total mass held by vortices in the domain. At higher γ where this instability occurs, the largest of the small vortices can hold up to 2.8% of the mass, and the state resembles a state having undergone the type 3i instability. There is a smooth transition between the different types of instabilities occurring, as seen in figure 4.15 showing that more than one type of instability may occur at a fixed $(\gamma, \mathcal{R})$ at different nearby λ (this is discussed further below). Additionally, our results are consistent with those of Waugh and Dritschel (1991), who found that strips of PV are more likely to roll-up to form vortices as the interaction range

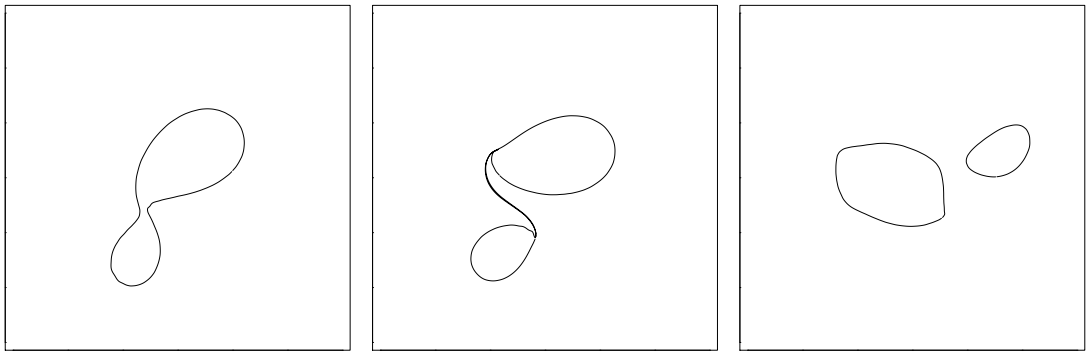

Figure 4.13: An example of a state having $(\gamma, \mathcal{R}, \lambda) = (4, -0.8, 0.150)$, which undergoes a split into two asymmetric vortices. We see the state right before the split at $t = 22.93T_p$ (left), during the split at $t = 23.07T_p$ (middle), and what the state looks like at a late time $t = 54.93T_p$ (right).

decreases, i.e. for increasing γ.

In figure 4.13 we show an example of the type 3i instability for an anticyclonic state having $(\gamma, \mathcal{R}) = (4, -0.8)$ at $\lambda = \lambda_c = 0.150$, which splits into two vortices of unequal size. During the onset of instability, the state exhibits behaviour similar to that of the type 2 instability, where it looks like it is about to shed a filament. There is a competition between the wave-3 and wave-4 instabilities, and the state pinches off a small vortex, which, especially for $1 \leq \gamma < 3$, may further interact with the larger vortex before reaching a final quasi-steady state in which the two vortices corotate. Although not occurring in the case shown in the figure, as in the type 2 instability regime, small satellite vortices may roll up from the filaments shed during the split. Apart from the case $(\gamma, \mathcal{R}, \lambda) = (1, -0.1, 0.230)$ where the largest satellite vortex contains 3.5% of the total mass held by the vortices in the domain (this compares to 5% of the mass held by the second-largest vortex in the domain), satellite vortices normally contain less than 0.6% of the mass.

Finally, in figure 4.14 we show an example of a state having $(\gamma, \mathcal{R}) = (4, -0.2)$ at $\lambda = \lambda_c = 0.065$, which splits into two vortices of equal size. The state rapidly decreases its aspect ratio and splits, shedding tiny filaments which, as seen in the

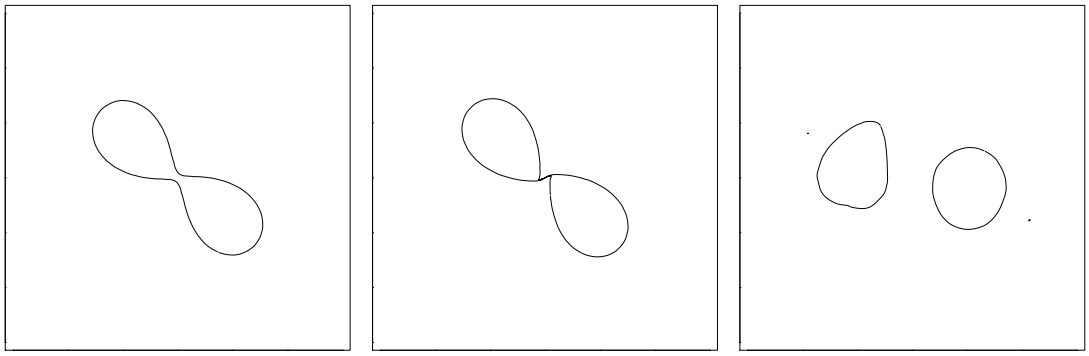

Figure 4.14: An example of a state having $(\gamma, \mathcal{R}, \lambda) = (4, -0.2, 0.065)$, which undergoes a split into two symmetric vortices. We see two times right before the split, $t = 2.15T_p$ (left) and $t = 2.28T_p$ (middle), and what the state looks like at a late time $t = 38.50T_p$ (right).

rightmost panel of the figure, roll up into very small vortices containing $\ll 1\%$ of the total mass held by vortices. Because of its resemblance to type 3i instability, we call this type 3ii instability.

We next present a quantitative measure for dividing unstable vortex behaviour into the four instability regimes described above. In §4.3 we have already discussed how we determine if a state is vacillating, and here we instead focus on the evolution types of states which undergo break-up. As the end state is generally composed of two larger vortices, we perform the classification based on the ratio of the masses of the two largest patches of PV in the domain at the end of the simulation, $M_r = M_2/M_1$, where the subscripts 1 and 2 denote the largest and second-largest vortices in the domain, respectively. We say that a state undergoes type 2 instability, filamentation, when $M_r < 0.03$. The type 3i and 3ii instability regimes, asymmetric and symmetric splitting, occur if $0.03 \leq M_r < 0.99$ and $M_r \geq 0.99$, respectively.

Figure 4.15 shows a summary of where the different instabilities occur in the $\gamma - \mathcal{R}$ parameter plane, with type 1 instability marked by asterisks, type 2 instability by circles, and types 3i and 3ii by squares and filled-in squares, respectively. Note, several types of instability can occur at the same $(\gamma, \mathcal{R})$ value;

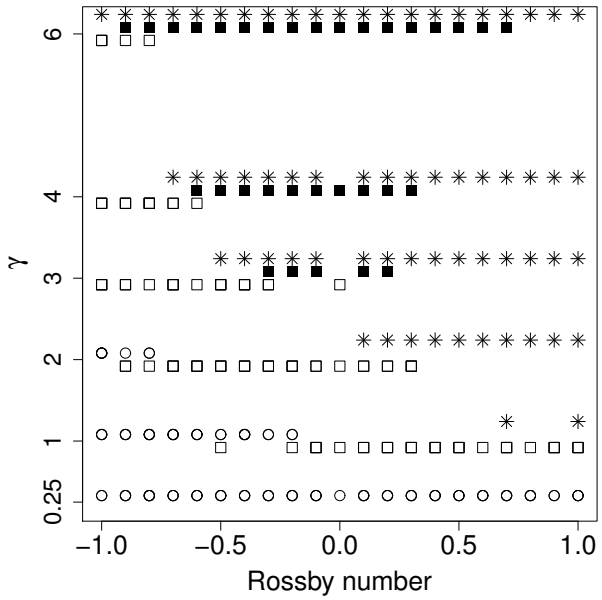

Figure 4.15: A summary of the instability types at each γ classified by their end mass shown as a function of $\mathcal{R}$ for aspect ratios near λ_c. The instability types shown are: type 1, vacillations (asterisks); type 2, filamentation with $M_r < 0.03$ (circles); type 3i, asymmetric split with $0.03 \leq M_r < 0.99$ (squares); and type 3ii, symmetric split with $M_r \geq 0.99$ (filled-in squares). Note that we also show the $\mathcal{R} = 0$ results, as found in chapter 2.

these instabilities occur on vortices with different λ near λ_c. We see that for states with $\gamma < 1$, the type 2 instability is the only one occurring, while at large $\gamma > 2$ it is completely absent. In the intermediate vortex-size range $1 \leq \gamma \leq 2$, this type of instability only occurs in anticyclones, and only for increasingly large $|\mathcal{R}|$ as γ increases. Type 1 and 3 instabilities are typical of the large-γ states. Type 3i instability occurs at smaller γ, where it is more common in cyclones, but as γ increases, it starts affecting a narrower range of increasingly small $\mathcal{R}$: at $\gamma = 6$ it only affects states with $-1 \leq \mathcal{R} \leq -0.8$, whereas at $\gamma = 1$ it affects states with $-0.5 \leq \mathcal{R} \leq 1$. Type 3ii instability occurs only for large $\gamma \geq 3$, and similarly to type 3i instability, at smaller γ it occurs mainly in states with small $|\mathcal{R}|$. As γ increases it begins to affect states with larger $|\mathcal{R}|$. This is also true of the type 1 instability, which, as γ increases, begins to affect a wider range of $\mathcal{R}$. Both the type 1 and type 3ii instabilities involve a wave-4 disturbance. However, as in chapter 2, whether a strong (vortex breakup) or weak (vacillations) instability occurs is highly sensitive to the choice of λ. We believe this can be attributed to the sensitivity on λ of the large-amplitude waves travelling on the vortex boundary. When the phases of the waves are slightly out of synch, vacillations, rather than breaking, occurs.

As mentioned above, as γ increases, there is a smooth transition from the type 2 to type 3i instabilities, with the filaments shed rolling up to form increasingly large vortices, and from the type 3i to 3ii instabilities, with the smaller vortex gradually becoming larger until the wave-4 instability, resulting in a symmetric split of the state, dominates over the wave-3 one which causes a filament to be shed from one of the tips of the vortex.

Finally, we note that the total mass held by all of the vortices in the domain at the end of the simulation is generally not the same as the mass held by the vortex initially. In fact, mass conservation only occurs for large-γ states which undergo symmetric or near-symmetric splitting. Most states which undergo type

3 instabilities lose no more than 5% of their mass in the process. States experiencing types 2 and 3i instabilities (only anticyclones for the latter) may lose up to 14% of their mass in the process.

4.6 Quantification of imbalance

In this section we aim to quantify the unbalanced component of the flows considered in this chapter, and to show how it develops as a function of time. We do this by first calculating the minimally-unbalanced fields, which we then subtract from the full fields. This provides us with an approximation of the amount of imbalance. In §4.2.2 we discussed how the OPV procedure can be used for initialising the flow. In fact, given a distribution of PV, OPV can be used for calculating the minimally-unbalanced fields at any time during the simulation. However, using this method requires a change of the length of the ramp period Δ_τ at different times of the simulation (we fail to obtain convergence if Δ_τ is too short in some cases, and in others, PV contours get convoluted for Δ_τ too long). As the amount of imbalance in the calculated fields is dependent on the choice of Δ_τ (recall that we do not impose any specific balance conditions), comparisons at different stages of a simulation cannot be made. To avoid this problem, we instead use the "dynamic PV initialisation" (PVI) procedure of Viúdez and Dritschel (2004a). Similarly as in OPV, we start this procedure with a flow at rest and, by using the same smooth ramping function, grow the PV anomaly of each fluid particle to a prescribed value, while integrating the full equations. The difference between the two procedures comes from the fact that unlike in OPV which allows the contours of PV to evolve freely during a series of forwards and backwards integrations, in PVI we perform only one forward integration while holding the contours of PV fixed in space. Although not as accurate as OPV, PVI still provides us with a good approximation of the fields

which are surprisingly close to the minimally-unbalanced ones obtained by OPV, see e.g. figure 9 of McKiver and Dritschel (2008) who found that there are only very minor differences in the minimally-unbalanced fields calculated using OPV and a "nonlinear quasi-geostrophic balancing" (NQG) procedure. Their NQG procedure used in the non-hydrostatic Boussinesq context is equivalent to a first order balance condition in SW, in which $\delta_t = \chi_t = 0$.

In figures 4.16 and 4.18–4.20 below, we show the root mean square (over the entire domain) of the balanced (in black) and unbalanced (in grey) components of three fields, namely that of the height anomaly h' (the top panel of each of the figures), of u', the x-component of velocity in a frame rotating with the equilibrium vortex (the middle panel), and of the divergence δ (the bottom panel). The subscripts "b" and "i" are used to distinguish between the "balanced" and "unbalanced" part of the fields ("balance" and "imbalance"), respectively. Note that the full fields are recovered from the sum of the two components. In the figures, we show how the flow develops from the start to the end of the ramping period of length Δ_τ, and then for $100T_p$ once the ramping period has been completed. We thus have a rapid initial growth of the fields during the ramp.

In figure 4.16 we show an example of the decomposition of the flow at $(\gamma, \mathcal{R}) = (6, 0.5)$ for aspect ratios corresponding to three different flow regimes, namely a stable state with $\lambda = \lambda_s = 0.120$ (dotted lines in the figure), a vacillating state (dashed lines), and an unstable state (solid lines) both near $\lambda = \lambda_c = 0.020$. We see that the form of both the balanced and unbalanced parts of h' are almost identical for all the cases, with perhaps a very small jump at the time of instability $t = 6.96T_p'$ in the unbalanced fields of the unstable state. The x-component of velocity u' also has similar values for all three cases, with oscillations being visible for all three cases in u_b', as the state adjusts itself to the flow around it (v', the y-component of the velocity in a frame rotating with the equilibrium, is similar both quantitatively and qualitatively). Note that the point at which the

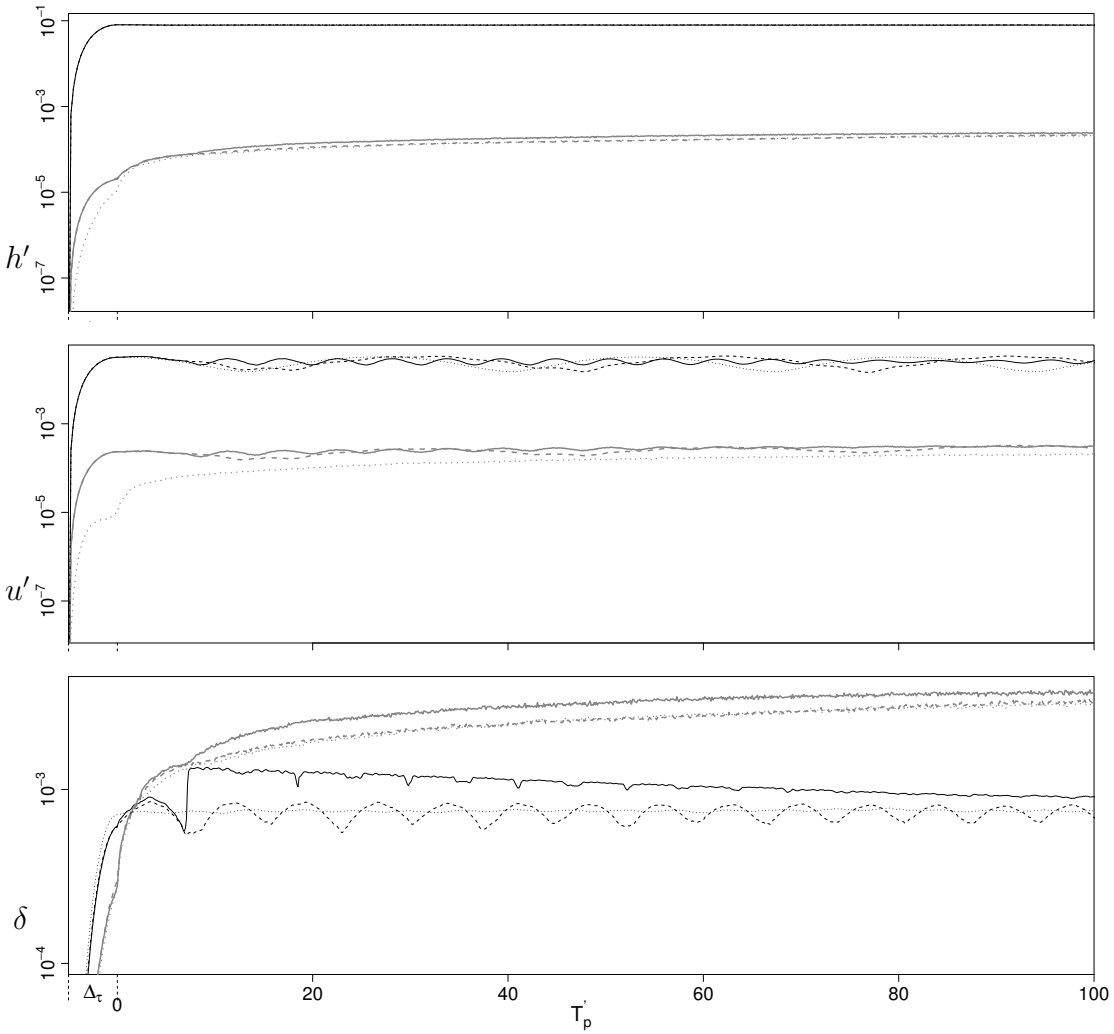

Figure 4.16: The balanced (black) and unbalanced (grey) fields for a stable (dotted; $\lambda = 0.120$), vacillating (dashed; $\lambda = 0.020$) and unstable (solid; $\lambda = 0.015$) state having $(\gamma, \mathcal{R}) = (6, 0.5)$. Here, and in figures 4.18–4.20, in rows 1 to 3 we see the root mean square (over the entire domain) of: h', the anomaly in height; u', the x-component of the horizontal velocity in a frame rotating with the equilibrium vortex; and of the divergence δ. Note that "$t = 0$" occurs at the end of the ramping period, of duration $10T_{ip}$.

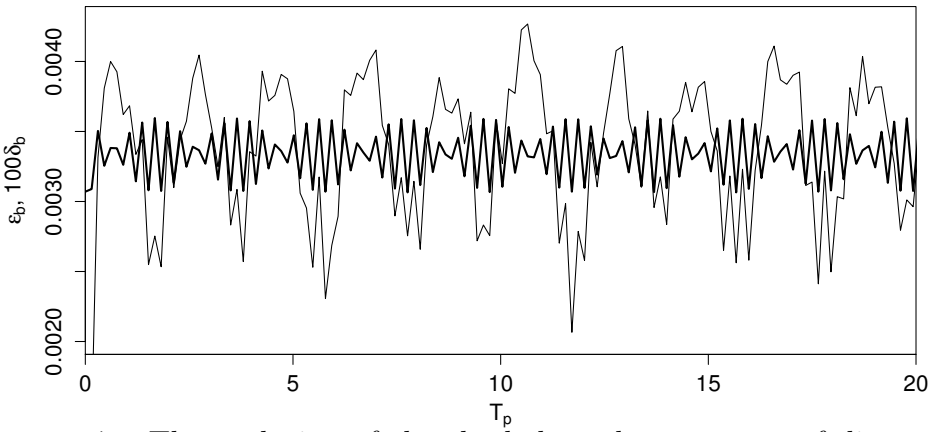

Figure 4.17: The evolution of the the balanced component of divergence $\delta_{\rm b}$, scaled by a factor of 100 (bold line), superimposed on top of the steadiness parameter $\epsilon_b(t)$ (thin line) for the stable state $(\gamma, \mathcal{R}) = (0.25, -0.1)$ near $\lambda = \lambda_s$. Note that we only show $t = 0 - 20T_p$, but similar behaviour is obtained for all time.

instability occurs is not apparent in either $h'_{\rm b,i}$ or $u'_{\rm b,i}$. The divergence δ, especially its balanced part, $\delta_{\rm b}$, is most sensitive to detecting the regime of stability of the flow. We see that the stable state has consistently low levels of $\delta_{\rm b}$ over the entire duration of the simulation; the amplitude of $\delta_{\rm b}$ in the vacillating state, like the aspect ratio λ, goes through cycles of increasing and decreasing. The point of instability is clearly marked in $\delta_{\rm b}$ for the unstable state, where it suddenly spikes, before beginning to slowly fall again after the instability as the newly formed quasi-steady state adjusts itself. Although $\delta_{\rm i} > \delta_{\rm b}$ in all of the three cases shown, both $\delta_{\rm i}$ and $\delta_{\rm b}$ are still very small (compared to the root mean square vorticity), even during instability. Note that no wave damping is present in the numerical code used, hence there is a gradual growth of $\delta_{\rm i}$ as time progresses, as waves are continually generated by the state in all three cases.

As noted above, the divergence is the field which is most sensitive to detecting instability. The significance of δ is that geostrophically balanced motions are non-divergent, and if higher-order balance conditions are accounted for in $\delta_{\rm b}$, we can view $\delta_{\rm i}$ as a means of measuring inertia-gravity wave activity. However, our "balanced" fields do contain a minimal amount of imbalance, and so they may

still contain a signal of wave activity. We illustrate this in figure 4.17, which shows the evolution of δ_{b}, scaled up by a factor of 100, superimposed on top of the steadiness parameter $\epsilon_b(t)$ for a stable state with $(\gamma, \mathcal{R}) = (0.25, -0.1)$ near $\lambda = \lambda_s$. As mentioned in §4.3, even though ϵ_b remains small for all times for stable states, oscillations are still present. In the figure, we see that there is a strong anti-correlation between ϵ_b and δ_{b}: for low values of ϵ_b (i.e. increased steadiness of the state), there are bursts of activity in δ_{b}, while when ϵ_b is higher, there seems to be no activity in δ_{b}. We interpret this as follows. The bursts of activity correspond to the generation of higher-order (in $\mathcal{R}$) inertia-gravity waves, which have not been detected in full by our PVI balancing procedure, and are therefore included in δ_{b} instead. When the equilibrium reaches some "maximally unsteady" form (i.e. when ϵ_b has a local maximum), it adjusts itself by emitting waves, which propagate away from the vortex boundary, contributing towards the total amount of imbalance in the domain, but not directly affecting the vortex itself; a signal of this emission is present in δ_{b}. This emission of waves allows the state to become more steady (and corresponds to a local minimum of ϵ_b). The whole procedure then repeats itself for the entire duration of the simulation. It appears that δ_{b} is composed of two main parts, the first corresponding to the balanced dynamics, apparent when there are no bursts of wave activity, and the second corresponding to the emission of gravity waves.

As seen in figure 4.16 for three different aspect ratios at $(\gamma, \mathcal{R}) = (6, 0.5)$, both the balanced and unbalanced components of h', u' and δ have similar values for all cases over the entire duration of the simulation, and so apart from affecting the stability regime of the flow, the aspect ratio λ does not seem to have a large effect on the values of these fields. We henceforth concentrate on examining the unstable states near $\lambda = \lambda_c$, as this allows us to see how the unbalanced component of each of the fields is affected by instability, especially if δ is examined. We next illustrate how the decomposition of h', u', and δ is affected by the sign of

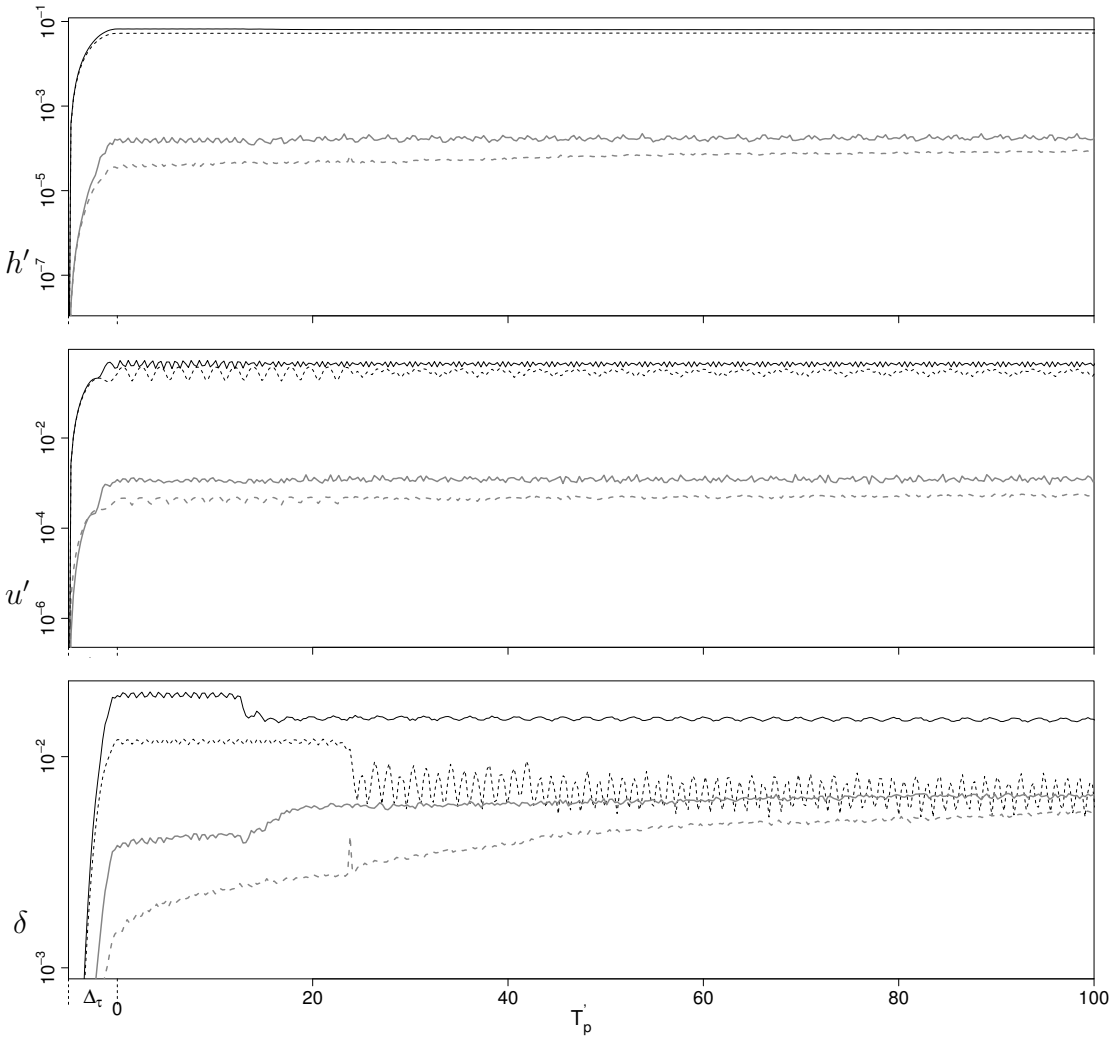

Figure 4.18: The balanced (black) and unbalanced (grey) fields for cyclonic (dashed) and anticyclonic (solid) unstable states near $\lambda = \lambda_c$ at $(\gamma, |\mathcal{R}|) = (1, 0.8)$.

the Rossby number. Figure 4.18 shows the state $(\gamma, |\mathcal{R}|) = (1, 0.8)$ near $\lambda = \lambda_c$, with fields corresponding to the cyclone shown with a dashed line, and those representing the anticyclone shown with a solid line. We see that for all of the fields, both the balanced and unbalanced components are smaller for the cyclone than for the anticyclone, and that this is more pronounced in the unbalanced fields. As mentioned previously, this is not a result of the difference in the location of λ_c for cyclones and anticyclones (recall that cyclones are stable for smaller aspect ratios than anticyclones), but rather arises from a difference in the nature of the two types of flows. From figure 4.18 we also note that the signature of the instability in δ_{b} is more visible in cyclones than in anticyclones, but the reverse is true for δ_{i}. We once again note the very low values of the unbalanced fields for h', u', and δ, in comparison to the balanced ones for h' and u', and to root mean square vorticity for δ.

In figure 4.19 we illustrate the effects of increasing $|\mathcal{R}|$ in examples of unstable anticyclonic states with $\gamma = 6$ near $\lambda = \lambda_c$. We once again show the balanced and unbalanced fields, this time for a state with $\mathcal{R} = -0.1$ (solid lines in the figure), $\mathcal{R} = -0.5$ (dashed lines), and $\mathcal{R} = -0.8$ (dotted lines). While the form of the balanced and unbalanced components of all of the fields does not change qualitatively with $\mathcal{R}$, it does seem to scale with $|\mathcal{R}|$, with higher-$|\mathcal{R}|$ states having larger values of both components of the fields. Additionally, we see that the signature of the instability in δ_{b} is more apparent for the small-$|\mathcal{R}|$ state, although the post-instability adjustment period is longer and more extreme in large-$|\mathcal{R}|$ states. Here, bursts of activity of comparable magnitude to those during the instability itself take place. Once again though, even for large-$|\mathcal{R}|$ states, the magnitude of the unbalanced fields is small (compared to the balanced fields for h' and u', and to root mean square vorticity for δ), and moreover the signature of the instability is not readily visible in them.

Finally, in figure 4.20 we examine the role large-scale effects play in determin-

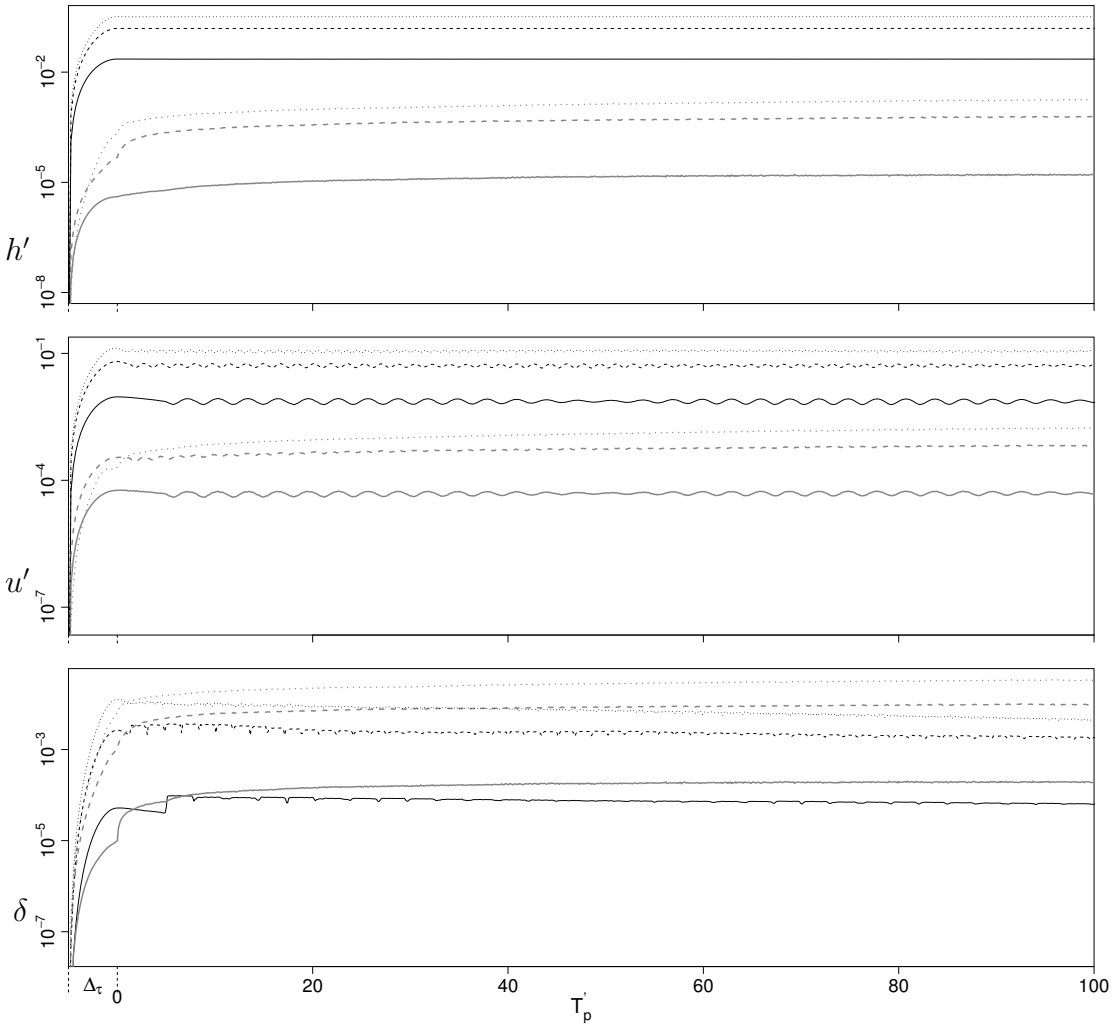

Figure 4.19: The balanced (black) and unbalanced (grey) fields for anticyclonic states near $\lambda = \lambda_c$ at $\gamma = 6$ and $\mathcal{R} = -0.1$ (solid), -0.5 (dashed), and -0.8 (dotted).

ing the magnitudes of the balanced and unbalanced components of the flow. We show three γ values: a small-γ state with $\gamma = 0.25$ (solid lines in the figure), an intermediate-γ state with $\gamma = 1$ (dashed lines), and a large-γ state with $\gamma = 6$ (dotted lines). We see that large-scale effects cause an increase in both h'_{b} and h'_{i}, which is not surprising since the large-γ states are affected by larger surface deformations than small-γ ones (cf. figure 4.7). For the other fields examined, the effect of increasing the size of the vortex (or γ) is less obvious. The magnitude of u'_{i} increases with γ, although the differences between states with different γ are small. This is in contrast to u'_{b}, where the differences between states with different γ are not only much more pronounced, but also have higher values at small γ. This is not surprising either: as γ increases, motions become slower, and so the velocity decreases in the rotating frame of reference; u'_{i} retains similar values for all γ, but its role becomes more important in large-γ states as the ratio $u'_{\mathrm{i}}/u'_{\mathrm{b}}$ grows with γ. The large-scale effects in δ show a difference in behaviour for the large-γ and small-γ regimes discussed in the previous sections. For all states, as γ increases, so does the value of δ_{i}. However, δ_{b} only increases with γ for small-γ states; for the large-γ state shown, δ_{b} has lower values than in the intermediate-γ state. This means that large-γ states are more affected by the unbalanced component of the flow than small-γ ones. Lastly, the signature of the instability becomes more apparent in δ_{b} as γ increases.

As noted above, the flow (at rest) is initially balanced, but during the initial PV ramping inertia-gravity wave activity is inevitably excited. We illustrate this process by examining how the curvature κ of the PV contour develops with time. The curvature is highly sensitive to any irregularities in the smoothness of the contour, and hence is able to pick up signals of what we believe to be waves of very small amplitude, not visible otherwise. Figure 4.21, complemented by supplementary movie 1, shows $\kappa(\theta, t)$ for the state $(\gamma, \mathcal{R}, \lambda) = (1, 0.1, 0.400)$ as a function of the tangent angle θ at time $t = 0$ before the start of the PV

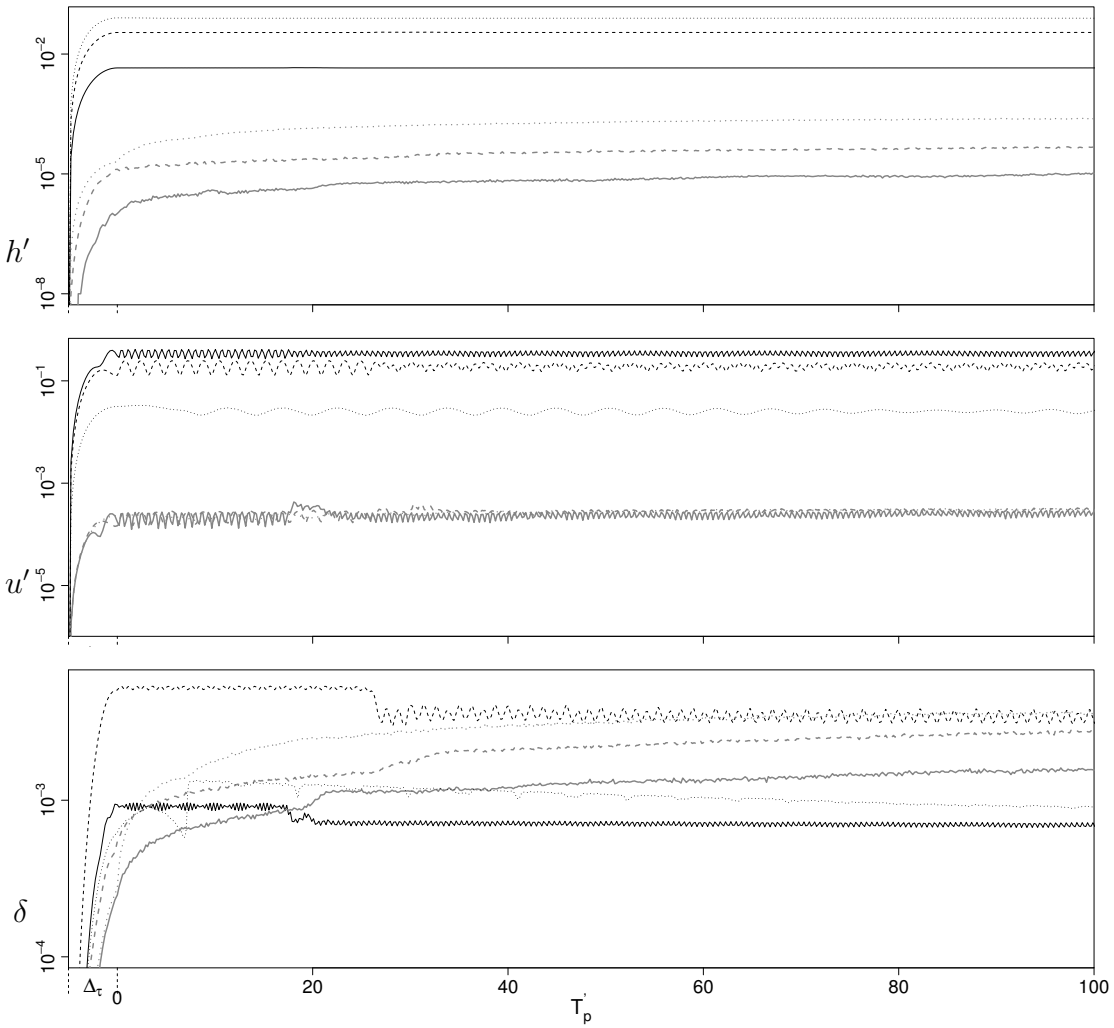

Figure 4.20: The balanced (black) and unbalanced (grey) fields for cyclonic states near $\lambda = \lambda_c$ at $\mathcal{R} = 0.5$ and $\gamma = 0.25$ (solid), 1 (dashed), and 6 (dotted).

ramp (grey line in the figure), and at times $t = 2T_{ip}$ and $t = 4T_{ip}$ during the ramp (black lines in the figure). We have taken great care in calculating the curvature by using global cubic splines to ensure continuity of the tangent and curvature (Dritschel and Scott, 2013, personal communication). We see that initially, when the state is balanced, the curvature is smooth and contains no sign of irregularities. As time grows, it becomes increasingly rugged, and the irregularities appear to be propagating away from regions in which they first appear (this is especially clear in the supplementary movie). The irregularities are initially most pronounced in areas of low curvature, which are also regions of high velocities, and hence correspond to regions having maximal local Froude number, $\mathcal{F} = U/c$. Numerous studies have shown that flows with high $\mathcal{F}$ are more likely to generate waves than low-$\mathcal{F}$ ones. These includes works by Ford (1994) who analytically examined the $\gamma \to 0$ case, Dritschel and Vanneste (2006) who examined a straight PV front with $\gamma = 1$, and others (including Spall and McWilliams, 1992; Polvani et al., 1994). Additionally, results suggest that the curved shapes of vortices are more likely to generate gravity-wave instabilities than fronts with no curvature, hence irregularities also form initially in areas of high curvature. We therefore believe that the signal present in κ corresponds to inertia-gravity waves, which are not visible otherwise (cf. figure 4.1 in which, for $(\gamma, |\mathcal{R}|, \lambda) = (1, 0.5, 0.400)$ at $t = 10T_{ip}$, the contours of PV look smooth).

In summary, we find that even for unstable states, the amount of imbalance generated by the quasi-equilibria studied is very low. The amount of imbalance produced increases with $|\mathcal{R}|$, and is higher in anticyclones than in cyclones. Additionally, we find a difference of behaviour in small- and large-γ states, where large-scale effects often result in greater amounts of imbalance.

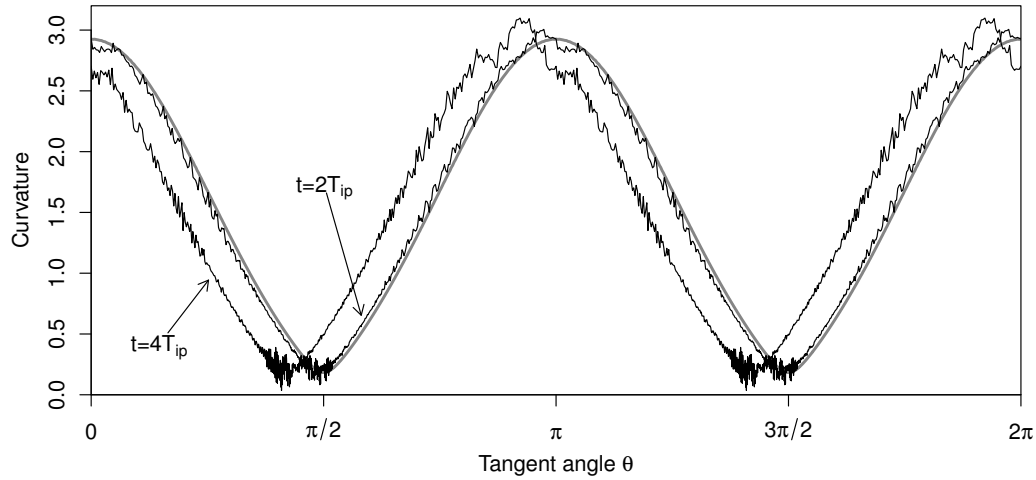

Figure 4.21: The curvature κ as a function of the tangent angle θ around the PV contour for the state $(\gamma, \mathcal{R}) = (1, 0.1)$ at $\lambda = 0.400$. We show the initial curvature of the QGSW contour (grey line) and κ at times $t = 2T_{ip}$ and $t = 4T_{ip}$ (black lines) during the ramping period. Recall that the ramping period lasts from $t = 0$ to $t = \Delta_\tau = 10T_{ip}$. Note that the shift along the x-axis arises from differences in what the numerical method specifies as the "first" point on each PV contour. See also supplementary movie 1.

4.7 Conclusions

We have examined the form and stability of vortex-patch relative quasi-equilibria in the single-layer f-plane shallow-water model of geophysical fluid dynamics. These states depend on three parameters: the ratio γ between their mean radius L and the Rossby deformation length L_D, their aspect ratio λ, and their strength relative to the background rotation, measured by the Rossby number $\mathcal{R}$.

The states we generate in this model problem are not strictly in equilibrium, since in shallow-water, even in initially well-balanced flows, there is always some degree of inertia-gravity wave generation. By defining a "steadiness" parameter, which measures how closely aligned the contours of potential vorticity (defining the boundary of the vortex) and those of the Bernoulli pressure function are, we show that both the stable and unstable states generated are steady, which is

further confirmed by the long times for which the stable states remain unchanged in shape; indeed, they have less than a 5% average variation in λ over the duration of the simulation. For simplicity, we refer to the quasi-equilibria as just equilibria.

We find the stable aspect ratio λ_s, which depends on both γ and $\mathcal{R}$, at which equilibria cease to be steady. The instability can either be weak, occurring at $\lambda_s = \lambda_v$, where the state vacillates around the steady state by going through cycles of increasing and decreasing its aspect ratio, or strong, at $\lambda_s = \lambda_c$, where the vortex undergoes a drastic change in shape, often involving a break-up into two or more parts. For both the weakly-unstable vacillating states, and for the strongly unstable ones after they have settled down after instability, the flow is often close to equilibrium. Families of equilibria for which vacillations occur and so $\lambda_s = \lambda_v$ may still contain members having $\lambda = \lambda_c$ such that for any $\lambda < \lambda_c$ the vortex experiences a strong instability. Multiple forms of instability may occur for nearby values of λ.

Large-scale effects (large γ values) stabilise vortices, regardless of their strengths ($\mathcal{R}$). These large-scale stabilising effects are most pronounced for large-$\mathcal{R}$ states, where the location of λ_s for states with $\gamma \gtrsim 1$ becomes γ- and $\mathcal{R}$-independent. We find that for states with $\gamma \gtrsim 3$ and $\mathcal{R} \gtrsim -0.6$, the location of λ_s becomes γ-independent, and for $\mathcal{R} \gtrsim 0.8$ also $\mathcal{R}$-independent (see figure 4.9). This difference in behaviour between small-γ and large-γ states is also visible in the types of unstable evolution they undergo near λ_c: small-γ states are affected by the wave-3 instability, which causes them to shed a filament from one of its tips, whereas for large-γ states the most unstable mode is wave-4, which causes a nearly-symmetric split of the vortex. In the intermediate-γ range there is a competition between the two modes, resulting in a split of the vortex into two parts of unequal size.

By calling two states which share γ, $|\mathcal{R}|$, and λ "equivalent", we find a clear asymmetry in the stability of cyclonic ($\mathcal{R} > 0$) and anticyclonic ($\mathcal{R} < 0$) equilibria. Cyclones can sustain greater deformations than anticyclones before expe-

riencing an instability. In fact, for large enough γ and $\mathcal{R}$ (i.e. $\gamma \gtrsim 2$, $\mathcal{R} \gtrsim 0.5$) they may not experience a "strong" instability at all, even for λ close to 0. They rather undergo a weak instability, vacillating around an underlying equilibrium state. In general, cyclones are more prone to experiencing such a weak instability, with it being completely absent for anticyclones with large enough $|\mathcal{R}|$ at γ between 2 and 4. In short, *ageostrophic motions stabilise cyclones and destabilise anticyclones*. This is true even if vacillations are regarded as a strong, rather than weak instability. Both types of vortices undergo the same main types of unstable evolution, although the wave-4 instability dominates over the wave-3 one in cyclones at smaller γ than in anticyclones. This cyclone-anticyclone asymmetry is the opposite of what is generally reported in the literature. This, we believe, is due to the difficulty in defining "equivalent" cyclones and anticyclones.

We decompose the full flow into a "balanced" and "unbalanced" component in order to measure inertia-gravity wave generation by the equilibria. We find that even during and in the aftermath of instability, the flow remains very close to balance. We see that examining just the "unbalanced" component does not reveal the regime of stability that the state is in, and only when the "balanced" component, which contains high-order (in $\mathcal{R}$) amounts of imbalance, is also viewed can we say something more about the nature of the flow. Despite the fact that we find that levels of imbalance are consistently low for all cases studied, we see that the amount of imbalance increases with $|\mathcal{R}|$ and γ, and that anticyclones are more unbalanced than cyclones.

4.8 Supplementary movies

Supplementary movies are available on the compact disc attached to this thesis in the folder SW, with movie captions available in Appendix C.3. They will also be available in a forthcoming paper.

Chapter 5

Summary and Outlook

In this chapter we provide a brief summary and discussion of the main results of this thesis. We also provide a link between the individual chapters, and outline potential extensions to this work.

This thesis has examined the structure, stability and interaction of geophysical vortices. Geophysical flows are under the influence of planetary rotation and stratification, and, in a simplified context, this study examined what effect these two components have on balanced, vortical structures. In both simulations of geophysical flows and in observational data long-lived, unchanging (to a certain degree) vortices are common, and so we have restricted our attention to examining relative vortex equilibria. These are states which in a co-rotating frame of reference appear stationary. Understanding their properties allows insight into more complicated vortex-interaction problems.

We have approached the problem from three different perspectives, corresponding to each of the three main chapters of this thesis. Namely, in chapter 2 we have studied the single-vortex, quasi-geostrophic shallow-water (QGSW) problem; in chapter 3 we generalised this to an (asymmetric) two-vortex problem; lastly, in chapter 4 we re-visited the single-vortex problem, by making use

of the more realistic, albeit also more complicated, shallow-water (SW) model.

Full details of the findings of each of the sub-studies may be found in the Conclusions section of each of the chapters. Here, we provide a summary of their main findings.

In chapter 2 we have examined the form, stability and nonlinear evolution of two-fold symmetric vortex-patch relative equilibria in the single-layer quasi-geostrophic shallow-water model. The families of these equilibria are described by two parameters: the ratio γ of the mean vortex radius L to the intrinsic Rossby deformation length L_D, and the ratio λ of the minimum to the maximum width of the vortex. We find two principal modes of linear stability, both of which exhibit an "exchange-type" instability, where both the real and imaginary parts of the eigenfrequency are simultaneously zero at marginal stability. The first mode occurs mainly in small-γ states, and near the margin of stability the mode is asymmetric. It results in the ejection of a filament in the nonlinear evolution of the state. The second, symmetric mode occurs in large-γ states and results in a symmetric split of the state. A competition between the two modes is found to occur in states with intermediate γ, leading to asymmetric splits of the states. Lastly, at certain large-γ values, we find a weak nonlinear instability, vacillation, occurring at certain λ near the margin of stability, as a result of which variations of the shape of the equilibrium occur, but the state itself is not destroyed.

In chapter 3 we have examined the form, properties and stability of asymmetric single-layer quasi-geostrophic shallow-water doubly-connected relative equilibria. In addition to γ, two other parameters are needed to describe the families of these equilibria: the ratio α between the areas of the smaller and the larger vortices, and the minimum distance δ_{min} between the two vortices. By performing a linear stability analysis and examining the nonlinear evolution of the equilibria, we have related the two principal modes of linear stability that we find to different types of evolution. Once again, each of these modes occurs at either small

or large γ, with a transition region between them. The small-γ mode (absent in states with $\alpha \gtrsim 0.6$) is again, as in the single-vortex case, asymmetric, resulting in either one, or both of the vortices getting smaller through the shedding of filaments. The large-γ mode results in the merger of the two vortices, and the transition zone is characterised by a series of merging and splitting events, the end result of which are two vortices of unequal size. In chapter 3 we have also examined possible inviscid transitions between doubly-connected states and the simply-connected states of chapter 2, and found that although inviscid transitions are possible, they are not the preferred path of evolution.

In chapter 4 we have examined the form and stability of vortex-patch relative quasi-equilibria in the single-layer f-plane shallow-water model. These states, similarly to the simply-connected QGSW states of chapter 2, depend on γ and the aspect ratio λ, and only one additional parameter is necessary to describe them in SW, namely the Rossby number $\mathcal{R}$, which gives their strength relative to the background rotation. By defining an appropriate "steadiness" parameter, we have shown that despite the fact that in SW there is always some degree of inertia-gravity wave generation, it is still useful to view the states through the concept of equilibrium. We evolved the "equilibria" for sufficiently long times, and thus determined their boundary of stability $\lambda = \lambda_s$. We found that the instability at λ_s can either be weak, having the form of vacillations, or strong, with a break-up of the vortex. Additionally, large-scale effects (large γ values) stabilise vortices, regardless of their strength ($\mathcal{R}$), and we have found that although the levels of inertia-gravity wave activity increase with $|\mathcal{R}|$ and γ, they remain small even for unstable states.

One of the more significant findings of chapter 4 is that *ageostrophic motions stabilise cyclones and destabilise anticyclones.* Both types of vortices undergo the same main types of unstable evolution, although the symmetric instability mode dominates over the asymmetric one in cyclones at smaller γ than in anticyclones.

This cyclone-anticyclone asymmetry is the opposite of what is generally reported in the literature. This, we believe, is due to the difficulty in defining "equivalent" cyclones and anticyclones. Here, we have defined this "equivalence" in terms of γ, $|\mathcal{R}|$, and λ.

To summarise, we have found that in all of the systems studied, large vortices ($L \gg L_D$) are more likely to be stable than small ones. For the single-vortex problem, this means that large vortices can sustain much greater deformations before destabilising than small vortices, and for the two-vortex problem this means that vortices are able to come closer together before destabilising. Additionally, we found that for large vortices the stability of a vortex pair is not affected by the degree of its asymmetry, although it does affect the underlying steady state into which an unstable state transitions. Lastly, by carefully defining the "equivalence" between cyclones and anticyclones which appear in the SW system, contrarily to what is commonly believed, we found that cyclones are more stable than anticyclones.

There are a few possible routes for further investigation of geophysical vortex equilibria, both within the quasi-geostrophic shallow-water and in the shallow-water frameworks. One possibility would be to revisit the two-layer quasi-geostrophic (QG) problem studied by Polvani et al. (1989). This thesis has focused on systems in which the lower layer is infinitely deep, i.e. $D = H_1/H_2 \to 0$, where H_1 and H_2 are the depths ("heights") of the upper and lower layers, respectively. However, for most oceanic and atmospheric systems the lower layer has finite depth $D = \mathrm{O}(1)$, and so considering a two-layer system would be more realistic. Polvani et al. (1989) have argued that, in contrast to the QGSW problem, the dynamics of the two-layer system in the large-γ limit are expected to be similar to the barotropic case (when $\gamma = 0$), only with a rescaling of time (the "baroclinic", vertically-varying mode becomes weak compared to the barotropic, vertically-integrated mode when D is not small). Hence the large-γ results presented here

need to be interpreted with care. Polvani (1991), who examined two-layer QG equilibria, showed that, indeed, equilibria which do not overlap (vertically) behave similarly to the (scaled) barotropic ones, but overlapping equilibria do not. Essentially, baroclinic effects become important at short range, i.e. where vortices overlap. The vertical PV structure is also expected to play a major role; this is expected to strongly affect the relative importance of baroclinic effects, but to our knowledge has yet to be investigated in this context. Examining the two-layer system would additionally allow the study of the competition between the barotropic and baroclinic modes, and the energy transfer from the baroclinic to the barotropic mode in a very simple framework. This in itself is an interesting problem, especially in the oceanographic context (Ghil et al., 2002). It would also be of interest to understand how the conclusions of the aforementioned studies are affected in a model which allows ageostrophic motions.

More remains to be done in the two-vortex system of chapter 3, with a few possible extensions arising. In addition to examining the problem in a two-layer QG context, it would be interesting to further investigate the effects of asymmetry on the equilibria, this time including asymmetry in strength. Two patches of unequal PV have received little attention, except in the barotropic case (see Yasuda and Flierl, 1995; Trieling et al., 2005; Makarov and Kizner, 2011, and references therein). Furthermore, extending this study to the full shallow-water equations, as was done in chapter 4 with single-vortex equilibria, would permit one to study new effects such as spontaneous gravity-wave emission, ageostrophic effects, and the associated cyclone-anticyclone asymmetry. As with the single-vortex system, to our knowledge a careful study of the parameter space, consisting of the Rossby number in addition to $(\gamma, \alpha, \delta_{min})$, has not been performed, and the cyclone-anticyclone asymmetry is not well understood. This would also allow us to gain insight into the nature of the quasi-steady two-vortex states formed in chapter 4 as a result of instability, and to explore possible transitions between

SW equilibrium solutions.

Lastly, as seen in each of the chapters 2–4, the long-time persistence of the states formed after instability suggests that they oscillate around an underlying equilibrium. However, as discussed in the QGSW system in chapter 3, as a result of waves propagating on their boundary, it is difficult to determine these equilibria. Additionally, since we have found that there exist many robust time-dependent states especially at large γ (which are hard to quantify), it appears that examining vortices through the concept of equilibrium is not complete. This is an important conclusion from this thesis, suggesting a new paradigm. Studying an initially circular QGSW vortex, for example, with a fixed area and γ, in a random (in both phase and amplitude) irrotational straining flow would provide further insight into the impact of strain on the robustness of vortices.

In short, there remain a number of open, fundamental problems in equilibrium vortex dynamics whose study would help us better comprehend the complex, multi-faceted behaviour of vortices in the atmosphere and oceans.

Appendix A

Derivation of the linear dispersion relation for small amplitude waves

The following result may be deduced from Waugh and Dritschel (1991).

Consider a circular vortex of radius $r = 1$. The streamfunction is determined from

$$\frac{1}{r}\frac{\mathrm{d}}{\mathrm{d}r}\left(r\frac{\mathrm{d}\bar{\psi}}{\mathrm{d}r}\right) - \gamma^2\bar{\psi} = \begin{cases} 1 & , r < 1 \\ 0 & , r > 1, \end{cases} \tag{A.1}$$

and matching $\bar{\psi}$ and $\bar{u}_\theta = \bar{\psi}_r$ at $r = 1$, we find

$$\bar{\psi} = \begin{cases} -\gamma^{-2} + \mathrm{K}_1(\gamma)\mathrm{I}_0(\gamma r)/\gamma & , r < 1 \\ -\mathrm{I}_1(\gamma)\mathrm{K}_0(\gamma r)/\gamma & , r > 1 \end{cases} \tag{A.2}$$

and

$$\bar{u}_\theta = \bar{\psi}_r = \begin{cases} \mathrm{K}_1(\gamma)\mathrm{I}_1(\gamma r) & , r < 1 \\ \mathrm{I}_1(\gamma)\mathrm{K}_1(\gamma r) & , r > 1. \end{cases} \tag{A.3}$$

Next, consider an m-fold symmetric perturbation to this basic state, having the

form

$$\psi' = \hat{\psi}(r)\mathrm{e}^{\mathrm{i}(m\theta-\sigma t)} \quad , \qquad r' = \hat{r}\mathrm{e}^{\mathrm{i}(m\theta-\sigma t)}, \tag{A.4}$$

with $\psi = \bar{\psi} + \psi'$ and $r = \bar{r} + r'$, where $\bar{r} = 1$ and both ψ' and r' are suitably small. Note that the perturbation satisfies the Helmholtz equation on both sides of the jump since $q' = 0$ there,

$$(\nabla^2 - \gamma^2)\psi' = 0, \tag{A.5}$$

whose solutions are the modified Bessel functions of order m:

$$\hat{\psi} = \begin{cases} a\mathrm{K}_m(\gamma)\mathrm{I}_m(\gamma r) & , r < 1 \\ a\mathrm{I}_m(\gamma)\mathrm{K}_m(\gamma r) & , r > 1. \end{cases} \tag{A.6}$$

Since the vortex boundary moves as a material curve, its radial displacement satisfies

$$\frac{\mathrm{D}\eta}{\mathrm{D}t} = u_r(1 + r', \theta, t) = -\frac{1}{r}\frac{\partial\psi'}{\partial\theta}, \tag{A.7}$$

which, when linearised, gives simply

$$\hat{r}(m\bar{\Omega} - \sigma) = -m\hat{\psi}(1), \tag{A.8}$$

where $\bar{\Omega} = \bar{u}_\theta(1) = \mathrm{K}_1(\gamma)\mathrm{I}_1(\gamma)$.

Using the continuity of radial and tangential velocities $u_r = u'_r$ and $u_\theta = \bar{u_\theta} + u'_\theta$, respectively, gives $\hat{r} = -a$, and using $\hat{\psi}(1) = a\mathrm{I}_m(\gamma)\mathrm{K}_m(\gamma)$ gives, after some re-arrangement

$$\frac{\sigma}{m} = \mathrm{I}_1(\gamma)\mathrm{K}_1(\gamma) - \mathrm{I}_m(\gamma)\mathrm{K}_m(\gamma). \tag{A.9}$$

Appendix B

Contour-integral form of the energy for quasi-geostrophic vortex patches

The total energy, kinetic plus potential, of a spatially compact distribution of PV in a single-layer QG flow is given by

$$E = \frac{1}{2}\iint (u^2 + v^2 + \psi^2/L_D^2)\,\mathrm{d}x\mathrm{d}y = -\frac{1}{2}\iint q\psi\,\mathrm{d}x\mathrm{d}y \tag{B.1}$$

after integrating by parts and using the fact that all fields decay exponentially fast as $|x|$ and $|y| \to \infty$. For a single vortex patch, of uniform PV q_0 in a region $\mathcal{D}$ bounded by a contour $\mathcal{C}$ outside of which $q = 0$, we have

$$E = -\frac{q_0}{2}\iint_{\mathcal{D}} \psi\,\mathrm{d}x\mathrm{d}y\,, \tag{B.2}$$

where the streamfunction is itself obtained by an integration over the QG Green function:

$$\psi = -\frac{q_0}{2\pi}\iint_{\mathcal{D}} \mathrm{K}_0(\gamma r)\,\mathrm{d}x'\mathrm{d}y' \tag{B.3}$$

where $r = |\boldsymbol{x}' - \boldsymbol{x}|$ and $\gamma = 1/L_D$ henceforth. The purpose of this appendix is to show that the calculation of E can be reduced to a pair of contour integrals, which proves convenient for its numerical evaluation in the paper.

The starting point is Stokes' theorem written in polar coordinates:

$$\iint_{\mathcal{D}} \left[\frac{1}{r}\frac{\partial(rP)}{\partial r} - \frac{1}{r}\frac{\partial Q}{\partial \theta}\right] r\mathrm{d}r\mathrm{d}\theta = \oint_{\mathcal{C}} P r\mathrm{d}\theta + Q\mathrm{d}r\,. \tag{B.4}$$

To use this, in ψ we place $\boldsymbol{x}$ at the origin of our (polar) coordinate system, so that $x' - x = r\cos\theta$ and $y' - y = r\sin\theta$. Then ψ is given by the integral

$$\psi = -\frac{q_0}{2\pi}\iint_{\mathcal{D}} \mathrm{K}_0(\gamma r)\, r\mathrm{d}r\mathrm{d}\theta\,. \tag{B.5}$$

This can be reduced to a contour integral by choosing $Q = 0$ and $P = (\mathrm{K}_1(\gamma r) + B/r)/\gamma$, for an arbitrary constant B, since then $r^{-1}\mathrm{d}(rP)/\mathrm{d}r = -\mathrm{K}_0(\gamma r)$. However, to avoid a singularity in the contour integral (and in ψ), we must take $B = -1/\gamma$ since $\mathrm{K}_1(z) \sim 1/z$ as $z \to 0$. Then, noting that $r^2\mathrm{d}\theta = (x' - x)\mathrm{d}y' - (y' - y)\mathrm{d}x'$, and defining the function

$$H(z) = \big(z\mathrm{K}_1(z) - 1\big)/z^2\,, \tag{B.6}$$

we obtain

$$\psi = \frac{q_0}{2\pi}\oint_{\mathcal{C}} H(\gamma r)[(x' - x)\mathrm{d}y' - (y' - y)\mathrm{d}x']\,. \tag{B.7}$$

Next, we tackle the double integral over ψ needed to calculate the energy E:

$$E = -\frac{q_0^2}{4\pi}\oint_{\mathcal{C}}\iint_{\mathcal{D}} H(\gamma r)[(x' - x)\mathrm{d}y' - (y' - y)\mathrm{d}x']\,\mathrm{d}x\mathrm{d}y\,. \tag{B.8}$$

This time, we use polar coordinates relative to a fixed point $\boldsymbol{x}'$ in the outer contour integral, that is $x - x' = r\cos\theta$ and $y - y' = r\sin\theta$ (re-defining the

symbol θ). Then, we may write

$$E = +\frac{q_0^2}{4\pi} \oint_{\mathcal{C}} \int\int_{\mathcal{D}} H(\gamma r)[r\cos\theta \mathrm{d}y' - r\sin\theta \mathrm{d}x']\, r\mathrm{d}r\mathrm{d}\theta\,. \tag{B.9}$$

This time in Stokes' theorem, we take $P = 0$ and choose Q either to be $H(\gamma r)r^2\sin\theta$ or $H(\gamma r)r^2\cos\theta$, as appropriate. This leads to

$$E = -\frac{q_0^2}{4\pi} \oint_{\mathcal{C}} \oint_{\mathcal{C}} H(\gamma r)r^2[\sin\theta \mathrm{d}y' + \cos\theta \mathrm{d}x']\mathrm{d}r\,. \tag{B.10}$$

Then, using $r\cos\theta = x - x'$, $r\sin\theta = y - y'$ and $r\mathrm{d}r = (x - x')\mathrm{d}x + (y - y')\mathrm{d}y$, we arrive at the final form for E:

$$E = -\frac{q_0^2}{4\pi} \oint_{\mathcal{C}} \oint_{\mathcal{C}} H(\gamma r)[(\boldsymbol{x}' - \boldsymbol{x}) \cdot \mathrm{d}\boldsymbol{x}'][(\boldsymbol{x}' - \boldsymbol{x}) \cdot \mathrm{d}\boldsymbol{x}]\,. \tag{B.11}$$

This can be easily extended to multiple patches by summing over all pairs of associated contour integrals and PV jumps (cf. Dritschel, 1985).

It has been verified that this expression gives the correct energy for a circular vortex patch of unit radius, $E = \pi q_0^2[1/2 - \mathrm{I}_1(\gamma)\mathrm{K}_1(\gamma)]/\gamma^2$, which can be evaluated directly from the form of ψ given in Appendix A. Note that $E > 0$ for all γ and monotonically decreases to 0 as $\gamma \to \infty$. As $\gamma \to 0$, however, $E \to \infty$. This is perhaps not the result one would expect in this limit, in which the flow is governed by the 2D Euler equations. But energy cannot be defined in this limit, only "excess energy", by removing a divergent part (see Dritschel, 1985). Here, using the asymptotic properties of modified Bessel functions (cf. Watson, 1966), one can show that $H(\gamma r) \to (1/4)(\ln r^2 - 1) + C + \mathrm{O}(\gamma)$ as $\gamma \to 0$, where $C = [\ln(\gamma/2) + \gamma_e]/2$ and $\gamma_e = 0.57721566...$ is Euler's constant. The leading function of r is exactly that used to compute the excess energy for the 2D Euler equations (Dritschel, 1985). The constant C contributes $-\Gamma^2 C/2\pi$ to E, where $\Gamma = q_0 A$ and A is the area of the vortex patch. Hence, $E + \Gamma^2 C/2\pi$ — the excess

energy — is expected to be finite as $\gamma \to 0$. For a circular patch of unit radius, $\Gamma = q_0\pi$, and $E + \Gamma^2 C/2\pi$ reduces to $\pi q_0^2/16$, which is the correct value of the excess energy.

Finally, (B.11) can be generalised to any Green function of the form $G(r)$. Then, the function H is determined from $r^{-1}\mathrm{d}(r^2 H)/\mathrm{d}r = G(r)$ subject to $\lim_{r\to 0} r^2 H = 0$. The final expression is the same as in (B.11), omitting the leading 2π factor (4π is replaced by 2).

Appendix C

Supplementary movie captions

C.1 Movies of quasi-geostrophic shallow-water simply-connected equilibria

Supplementary movies are available on the compact disc attached to this thesis in the folder SC.

MOVIE SC1. Examples of simply-connected vortex equilibria for γ=0.5, 3, and 8. For each case we begin at the aspect ratio $\lambda = 1$, and end at the smallest aspect ratio attained, $\lambda = \lambda_f$. Here, $|x|, |y| \leq 2.3$. In this and subsequent movies we are in a frame of reference rotating with the equilibria.

MOVIE SC2. An example of type 2 instability, filamentation. We show the case $\gamma = 0.5$ and $\lambda_c = 0.296$, for times between $18.12T_p$ and $45.31T_p$. Note that $|x|, |y| \leq 3.3$ in this and subsequent movies.

MOVIE SC3. An example of type 3i instability, asymmetric split. We show the case $\gamma = 2$ and $\lambda_c = 0.091$, for times between $74.78T_p$ and $100.04T_p$.

MOVIE SC4. An example of type 3ii instability, symmetric split. We show the case $\gamma = 10$ and $\lambda = 0.024$, for times between $43.50T_p$ and $50.00T_p$.

MOVIE SC5. An example of type 1 instability, vacillation. We show the case $\gamma = 5$ and $\lambda = 0.024$, for times between 0 and $40.02T_p$.

C.2 Movies of quasi-geostrophic shallow-water doubly-connected equilibria

Supplementary movies are available on the compact disc attached to this thesis in the folder DC. They are also available online, hosted on the *Journal of Fluid Mechanics* website at http://dx.doi.org/10.1017/jfm.2013.104.

MOVIE DC1. Examples of doubly-connected vortex equilibria for γ=0.02, 3, and 10 at $\alpha = 0.2$. For each case we begin at the distance $\delta_{min} = 0.8$, and end at the smallest distance attained, $\delta_{min} = \delta_f(\gamma)$, at which a sharp corner develops on the boundary of one of the vortices. The smallest distance decreases with γ. In this and subsequent movies we are in a frame of reference rotating with the equilibria, and $|x|, |y| \leq 3$.

MOVIE DC2. An example of the evolution of a state undergoing partial straining out $\mathrm{PSO_b}$. We show the case $\gamma = 1$, $\alpha = 0.4$, and $\delta_{min} = 0.339$, for times between $88.47T_p$ and $132.71T_p$.

MOVIE DC3. An example of the evolution of a state undergoing partial merger PM. We show the case $\gamma = 2$, $\alpha = 0.6$, and $\delta_{min} = 0.270$, for times between $150.28T_p$ and $254.31T_p$.

MOVIE DC4. An example of the evolution of a state having large γ which undergoes complete merger CM. We show the case $\gamma = 10$, $\alpha = 0.2$, and $\delta_{min} = 0.268$, for times between $121.70T_p$ and $135.22T_p$.

MOVIE DC5. An example of the evolution of a state having small γ which undergoes complete merger CM. We show the case $\gamma = 0.02$, $\alpha = 1.0$, and

$\delta_{min} = 0.266$, for times between $33.50T_p$ and $100.49T_p$.

MOVIE DC6. An example of the evolution of a state undergoing vacillations. We show the case $\gamma = 10$, $\alpha = 0.4$, and $\delta_{min} = 0.200$, for times between 0 and $115.68T_p$. Note, the boundary of stability occurs at $\delta_{min} = \delta_c = 0.265$.

C.3 Movies of shallow-water simply-connected quasi-equilibria

Supplementary movies are available on the compact disc attached to this thesis in the folder SW. They will also be available in a forthcoming paper.

MOVIE SW1. The curvature κ as a function of θ for the state $(\gamma, \mathcal{R}) = (1, 0.1)$ at $\lambda = 0.400$, for times between 0 and $11T_{ip}$ (recall, the ramp period has length $\Delta_\tau = 10T_{ip}$). Here, $\theta = 2\pi\xi(s)/\xi(P)$, where P is the arc length of the PV contour, s is the distance along the PV contour and $\xi(s) = \int_0^s |\kappa| \mathrm{d}s'$. When $\kappa > 0$, θ is the tangent angle. The shift along the x-axis arises from differences in what the numerical method specifies as the "first" point on each PV contour. Note that here the contour is discretised by 1200 points on a grid having a resolution of 1024^2.

Bibliography

M. Arai and T. Yamagata. Asymmetric evolution of eddies in rotating shallow water. *Chaos*, 4:163–175, 1994.

J. Aristegui, P. Sangrá, S. Hernandez-León, M. Canton, A. Hernández-Guerra, and J. L. Kerling. Island-induced eddies in the Canary islands. *Deep-Sea Res.*, 41:1509–1525, 1994.

O. Bühler. Wave-vortex interactions. In J. B. Flor, editor, *Fronts, waves and vortices in geophysics*, volume 805 of *Lect. Notes Phys*, pages 139–187. Springer-Verlag, 2010.

X. Carton. Hydrodynamical modelling of oceanic vortices. *Surveys Geophys.*, 22: 179–263, 2001.

C. Cerretelli and C. H. K. Williamson. A new family of uniform vortices related to vortex configurations before merging. *J. Fluid Mech.*, 493:219–229, 2003a.

C. Cerretelli and C. H. K. Williamson. The physical mechanism for vortex merging. *J. Fluid Mech.*, 475:41–77, 2003b.

J. G. Charney. On the scale of atmospheric motions. *Geofys. Publ. Oslo*, 17:3–17, 1948.

J. G. Charney and G. R. Flierl. Oceanic analogues of large-scale atmospheric mo-

tions. In B. A. Warren and C. Wunsch, editors, *Evolution of Physical Oceanography*, pages 504–548. MIT Press, Massachusetts, 1981.

J. Y.-K. Cho, M. de La Torre Juarez, A. P. Ingersoll, and D. G. Dritschel. A high-resolution, three-dimensional model of Jupiter's Great Red Spot. *J. Geophys. Res.*, 106:5099–5105, 2001.

B. Cushman-Roisin. Exact analytical solutions for the elliptical vortices of the shallow-water equations. *Tellus A*, 39:235–244, 1987.

B. Cushman-Roisin and B. Tang. Geostrophic turbulence and emergence of eddies beyond the radius of deformation. *J. Phys. Oceanogr.*, 20:97–113, 1990.

B. Cushman-Roisin, W. H. Heil, and D. Nof. Oscillations and rotations of elliptical warm-core rings. *J. Geophys. Res.*, 90(C6):11756–11764, 1985.

G. S. Deem and N. J. Zabusky. Vortex waves: stationary "V-states," interactions, recurrence, and breaking. *Phys. Rev. Lett.*, 40:859–862, 1978a.

G. S. Deem and N. J. Zabusky. Stationary "V-states," interactions, recurrence, and breaking. In K. Lonngren and A. Scott, editors, *Solitons in Action*, pages 277–293. Academic Press, 1978b.

D. G. Dritschel. The stability and energetics of corotating uniform vortices. *J. Fluid Mech.*, 157:95–134, 1985.

D. G. Dritschel. The nonlinear evolution of rotating configurations of uniform vorticity. *J. Fluid Mech.*, 172:157–182, 1986.

D. G. Dritschel. Contour surgery: a topological reconnection scheme for extended integrations using contour dynamics. *J. Comp. Phys.*, 77:240–266, 1988.

D. G. Dritschel. Contour dynamics and contour surgery: Numerical algorithms for extended, high-resolution modelling of vortex dynamics in two-dimensional, inviscid, incompressible flows. *Comput. Phys. Rep.*, 10:77–146, 1989.

D. G. Dritschel. The stability of elliptical vortices in an external straining flow. *J. Fluid Mech.*, 210:223–261, 1990.

D. G. Dritschel. Vortex properties of two-dimensional turbulence. *Phys. Fluids A*, 5:984–997, 1993.

D. G. Dritschel. A general theory for two-dimensional vortex interactions. *J. Fluid Mech.*, 293:269–303, 1995.

D. G. Dritschel and M. H. P. Ambaum. A contour-advective semi-Lagrangian algorithm for the simulation of fine-scale conservative dynamical fields. *Quart. J. Roy. Meteorol. Soc.*, 123:1097–1130, 1997.

D. G. Dritschel and J. Fontane. The combined Lagrangian advection method. *J. Comput. Phys.*, 229:5408–5417, 2010.

D. G. Dritschel and B. Legras. The elliptical model of two-dimensional vortex dynamics. II: disturbance equations. *Phys. Fluids A*, 3:855–869, 1991.

D. G. Dritschel and R. K. Scott. On the simulation of nearly inviscid two-dimensional turbulence. *J. Comput. Phys.*, 228:2707–2711, 2009.

D. G. Dritschel and R. K. Scott. personal communication, 2013.

D. G. Dritschel and J. Vanneste. Instability of a shallow-water potential-vorticity front. *J. Fluid Mech.*, 561:237–254, 2006.

D. G. Dritschel and Á. Viúdez. A balanced approach to modelling rotating stably stratified geophysical flows. *J. Fluid Mech.*, 488:123–150, 2003.

D. G. Dritschel and D. W. Waugh. Quantification of the inelastic interaction of unequal vortices in two-dimensional vortex dynamics. *Phys. Fluids A*, 4: 1737–1744, 1992.

D. G. Dritschel, L. M. Polvani, and A. R. Mohebalhojeh. The contour-advective semi-Lagrangian algorithm for the shallow water equations. *Mon. Weather Rev.*, 127:1551–1565, 1999.

D. G. Dritschel, R. K. Scott, C. Macaskill, G. A. Gottwald, and Tran C. V. Unifying scaling theory for vortex dynamics in two-dimenisional turbulence. *Phys. Rev. Lett.*, 101:094501, 2008.

C. C. Ebbesmeyer, B. A. Taft, J. C. McWilliams, C. Y. Shen, S. C. Riser, H. T. Rossby, P. E. Biscaye, and H. G. Östlund. Detection, structure, and origin of extreme anomalies in a Western Atlantic oceanographic section. *J. Phys. Oceanogr.*, 16:591–612, 1986.

J. Fontane and D. G. Dritschel. The HyperCASL algorithm: a new approach to the numerical simulation of geophysical flows. *J. Comput. Phys.*, 228:6411–6425, 2009.

R. Ford. The response of a rotating ellipse of uniform potential vorticity to gravity wave radiation. *Phys. Fluids*, 6(11):3694–3704, 1994.

R. Ford, M. E. McIntyre, and W. A. Norton. Balance and the slow quasimanifold: some explicit results. *J. Atmos. Sci.*, 57:1236–1254, 2000.

B. Fornberg. A numerical study of 2-D turbulence. *J. Comput. Phys.*, 25:1–31, 1977.

I. Garate-Lopez, R. Hueso, A. Sánchez-Lavega, J. Peralta, G. Piccioni, and P. Drossart. A chaotic long-lived vortex at the southern pole of Venus. *Nature Geosci.*, 6:254–257, 2013.

M. Ghil, Y. Feliks, and L. U. Sushama. Baroclinic and barotropic aspects of the wind-driven ocean circulation. *Phys. D*, 167(1–2):1–35, 2002.

R. W. Griffiths and E. J. Hopfinger. Experiments with baroclinic vortex pairs in a rotating fluid. *J. Fluid Mech.*, 173:501–518, 1986.

R. W. Griffiths and E. J. Hopfinger. Coalescing of geostrophic vortices. *J. Fluid Mech.*, 178:73–97, 1987.

B. J. Hoskins, M. E. McIntyre, and A. W. Robertson. On the use and significance of isentropic potential vorticity maps. *Quart. J. Roy. Meteor. Soc.*, 111:877–946, 1985.

M. N. Juckes and M. E. McIntyre. A high-resolution, one-layer model of breaking planetary waves in the stratosphere. *Nature*, 328:590–596, 1987.

J. R. Kamm. *Shape and stability of two-dimensional uniform vorticity regions*. PhD thesis, California Institute of Technology, 1987.

G. R. Kirchhoff. *Vorlesungen über mathematische Physik. Mechanik*. B. G. Teubner, 1876.

Z. Kizner, D. Berson, and R. Khvoles. Baroclinic modon equilibria on the beta-plane: stability and transitions. *J. Fluid Mech.*, 468:239–270, 2002.

Z. Kizner, G. Reznik, B. Fridman, R. Khvoles, and J. C. McWilliams. Shallow-water modons on the f-plane. *J. Fluid Mech.*, 603:305–329, 2008.

B. Legras and D. G. Dritschel. Vortex stripping and the generation of high vorticity gradients in two-dimensional flows. *Appl. Sci. Res.*, 51:445–455, 1993.

B. Legras, D. G. Dritschel, and P. Caillol. The erosion of a distributed two-dimensional vortex in a background straining flow. *J. Fluid Mech.*, 441:369–398, 2001.

A. E. H. Love. On the stability of certain vortex motions. *Proc. London Math. Soc.*, 25:18–43, 1893.

P. Luzzatto-Fegiz and C. H. K. Williamson. Stability of elliptical vortices from "Imperfect-Velocity-Impulse" diagrams. *Theor. Comput. Fluid Dyn.*, 24:181–188, 2010.

P. Luzzatto-Fegiz and C. H. K. Williamson. An efficient and general numerical method to compute steady uniform vortices. *J. Comp. Phys.*, 230:6495–6511, 2011.

P. Luzzatto-Fegiz and C. H. K. Williamson. Determining the stability of steady two-dimensional flows through imperfect velocity-impulse diagrams. *J. Fluid Mech.*, 706:323–350, 2012.

V. G. Makarov and Z. Kizner. Stability and evolution of uniform-vorticity dipoles. *J. Fluid Mech.*, 672:307–325, 2011.

V. G. Makarov, M. A. Sokolovskiy, and Z. Kizner. Doubly symmetric finite-core heton equilibria. *J. Fluid Mech.*, 708:397–417, 2012.

P. Malanotte-Rizzoli. Planetary solitary waves in geophysical flows. *Adv. Geophys.*, 24:147–224, 1982.

A. Mariotti, B. Legras, and D. G. Dritschel. Vortex stripping and the erosion of coherent structures in twodimensional flows. *Phys. Fluids*, 6:3954–3962, 1994.

M. E. McIntyre. Atmospheric dynamics: some fundamentals, with observational implications. In J. C. Gille and G. Visconti, editors, *The use of EOS for studies of atmospheric physics*, Proc. Internat. School of Phys. Enrico Fermi, pages 313–386. North Holland, 1993.

M. E. McIntyre and W. A. Norton. Potential vorticity inversion on a hemisphere. *J. Atmos. Sci.*, 57:1214–1235, 2000.

W. J. McKiver and D. G. Dritschel. Balance in non-hydrostatic rotating stratified turbulence. *J. Fluid Mech.*, 596:201–219, 2008.

J. C. McWilliams. The emergence of isolated coherent vortices in turbulent flow. *J. Fluid Mech.*, 146:21–43, 1984.

J. C. McWilliams. Submesoscale, coherent vortices in the ocean. *Rev. Geophys.*, 23:165–182, 1985.

M. V. Melander, N. J. Zabusky, and J. C. McWilliams. Asymmetric vortex merger in two-dimensions: Which vortex is "victorious"? *Phys. Fluids*, 30:2610–2612, 1987.

P. Meunier and T. Leweke. Three-dimensional instability during vortex merging. *Phys. Fluids*, 13:2747–2750, 2001.

T. B. Mitchell and C. F. Driscoll. Electron vortex orbits and merger. *Phys. Fluids*, 8:1828–1841, 1996.

T. B. Mitchell and L. F. Rossi. The evolution of Kirchhoff elliptic vortices. *Phys. Fluids*, 20:054103–1/12, 2008.

A. R. Mohebalhojeh. On shallow water potential vorticity inversion by Rossby-number expansions. *Q. J. R. Meteorol. Soc.*, 128:679–694, 2002.

A. R. Mohebalhojeh and D. G. Dritschel. On the representation of gravity waves in numerical models of the shallow-water equations. *Q. J. R. Meteorol. Soc.*, 126:669–688, 2000.

A. R. Mohebalhojeh and D. G. Dritschel. Hierarchies of balance conditions for the f-plane shallow-water equations. *J. Atmos. Sci.*, 58:2411–2426, 2001.

W. A. Norton. Breaking Rossby waves in a model stratosphere diagnosed by a vortex-following coordinate system and a technique for advecting material contours. *J. Atmos. Sci.*, 51:654–673, 1994.

J. Nycander, D. G. Dritschel, and G. G. Sutyrin. The dynamics of long frontal waves in the shallow water equations. *Phys. Fluids A*, 5:1089–1091, 1993.

D. B. Olson. Rings in the ocean. *Annu. Rev. Planet. Sci.*, 19:283–311, 1991.

E. A. Overman II. Steady-state solutions of the Euler equations in two dimensions II. local analysis of limiting V-states. *SIAM J. Appl. Math.*, 46:765–800, 1986.

J. Pedlosky. *Geophysical Fluid Dynamics*. Springer-Verlag, 1979.

R. T. Pierrehumbert. A family of steady, translating vortex pairs with distributed vorticity. *J. Fluid Mech.*, 99:129–144, 1980.

H. Płotka and D. G. Dritschel. Quasi-geostrophic shallow-water vortex-patch equilibria and their stability. *Geophys. Astro. Fluid*, 106(6):574–595, 2012.

H. Płotka and D. G. Dritschel. Quasi-geostrophic shallow-water doubly-connected vortex equilibria and their stability. *J. Fluid Mech.*, 723:40–68, 2013.

L. M. Polvani. *Geostrophic Vortex Dynamics*. PhD thesis, MIT/WHOI WHOI-88-48, 1988.

L. M. Polvani. Two-layer geostrophic vortex dynamics. Part 2. Alignment and two-layer V-states. *J. Fluid Mech.*, 225:241–270, 1991.

L. M. Polvani and D. G. Dritschel. Nonlinear vortex dynamics on the surface of the sphere: Equilibria and their stability. *J. Fluid Mech.*, 255:35–64, 1993.

L. M. Polvani and G. R. Flierl. Generalized Kirchhoff vortices. *Phys. Fluids*, 29: 2376–2379, 1986.

L. M. Polvani, N. J. Zabusky, and G. R. Flierl. Two-layer geostrophic vortex dynamics. Part 1. Upper-layer V-states and merger. *J. Fluid Mech.*, 205:215–242, 1989.

L. M. Polvani, J. C. McWilliams, M. A. Spall, and R. Ford. The coherent structures of shallow-water turbulence: deformation-radius effects, cy-

clone/anticyclone asymmetry and gravity-wave generation. *Chaos*, 4(2):177–186, 1994.

P. Ripa. On the stability of elliptical vortex solutions of the shallow-water equations. *J. Fluid Mech.*, 183:343–363, 1987.

S. M. Rosier, B. N. Lawrence, D. G. Andrews, and F. W. Taylor. Dynamical evolution of the northern stratosphere in early winter 1991/92, as observed by the improved stratospheric and mesospheric sounder. *J. Atmos. Sci.*, 51:2783 – 2799, 1994.

P. G. Saffman. *Vortex Dynamics*. Cambridge University Press, 1992.

P. G. Saffman and R. Szeto. Equilibrium shapes of a pair of equal uniform vortices. *Phys. Fluids*, 23:2339–2342, 1980.

R. Santangelo, R. Benzi, and B. Legras. The generation of vortices in high-resolution, two-dimensional decaying turbulence and the influence of initial conditions on the breaking of self-similarity. *Phys. Fluids A*, 1:1027–1034, 1989.

R. K. Scott and L. M. Polvani. Equatorial superrotation in shallow atmospheres. *Geophys. Res. Lett.*, 35:L24202, 2008.

R. K. Smith and D. G. Dritschel. Revisiting the RossbyHaurwitz wave test case with contour advection. *J. Comput. Phys.*, 217:473–484, 2006.

M. A. Spall and J. C. McWilliams. Rotational and gravitational influences on the degree of balance in the shallow-water equations. *Geophys. Astro. Fluid*, 64:1–29, 1992.

A. Stegner and D. G. Dritschel. A numerical investigation of the stability of isolated shallow water vortices. *J. Phys. Oceanogr.*, 30:2562–2573, 2000.

Y. Tang. Nonlinear stability of vortex patches. *Trans. Amer. Math. Soc.*, 304: 617–637, 1987.

W. Thomson. Vortex statics. *Math. Phys. Pap.*, IV:115–128, 1875.

R. R. Trieling, O. U. Velasco Fuentes, and G. J. F. van Heijst. Interaction of two unequal corotating vortices. *Phys. Fluids*, 17:087103–1/17, 2005.

G. K. Vallis. *Atmospheric and oceanic fluid dynamics*. Cambridge University Press, 2006.

Á. Viúdez and D. G. Dritschel. Dynamic potential vorticity initialization and the diagnosis of mesoscale motion. *J. Phys. Oceanogr.*, 34:2761–2773, 2004a.

Á Viúdez and D. G. Dritschel. Optimal potential vorticity balance of geophysical flows. *J. Fluid Mech.*, 521:343–352, 2004b.

G. N. Watson. *A Treatise on the Theory of Bessel Functions*. Cambridge University Press, 1966.

D. W. Waugh. The efficiency of symmetric vortex merger. *Phys. Fluids A*, 4: 1745–1758, 1992.

D. W. Waugh and D. G. Dritschel. The stability of filamentary vorticity in two-dimensional geophysical vortex-dynamics models. *J. Fluid Mech.*, 231:575–598, 1991.

D. W. Waugh and L. M. Polvani. Stratospheric polar vortices. In L. M. Polvani, A. H. Sobel, and D. W. Waugh, editors, *The Stratosphere: Dynamics, Chemistry, and Transport*, volume 190 of *Geophys. Monogr. Ser.*, pages 43–57. AGU, Washington, D.C., 2010.

H. M. Wu, E. A. Overman II, and N. J. Zabusky. Steady-state solutions of the Euler equations in two dimensions: Rotating and translating V-states with

limiting cases. I. Numerical algorithms and results. *J. Comp. Phys.*, 53:42–71, 1984.

I. Yasuda. Geostrophic vortex merger and streamer development in the ocean with special reference to the merger of Kuroshio warm core rings. *J. Phys. Oceanogr.*, 25:979–996, 1995.

I. Yasuda and G. R. Flierl. Two-dimensional asymmetric vortex merger: contour dynamics experiment. *J. Oceanogr.*, 51:145–170, 1995.

N. J. Zabusky, M. H. Hughes, and K. V. Roberts. Contour dynamics for the Euler equations in two dimensions. *J. Comput. Phys.*, 30:96–106, 1979.